

Czech Technical University in Prague
Faculty of Nuclear Sciences and Physical Engineering
Department of Physical Electronics



**Tight-focusing of short intense laser pulses in
particle-in-cell simulations of
laser-plasma interaction**

(Master's thesis)

Author: Bc. Petr Valenta
Supervisor: doc. Ing. Ondřej Klimo, Ph.D.
Consultant: Dr. Stefan Andreas Weber
Academic year: 2016/2017



ČESKÉ VYSOKÉ UČENÍ TECHNICKÉ V PRAZE
FAKULTA JADERNÁ A FYZIKÁLNĚ INŽENÝRSKÁ
Katedra fyzikální elektroniky

ZADÁNÍ DIPLOMOVÉ PRÁCE

Student: **Bc. Petr Valent**

Obor: **Informatická fyzika**

Školní rok: **2016/2017**

Název práce: **Zaostření krátkého intenzivního laserového impulsu do velmi malého ohniska v PIC simulacích interakce s plazmatem**
Tight-focusing of short intense laser pulses in PIC simulations of laser-plasma interaction

Vedoucí práce: **doc. Ing. Ondřej Klimo, PhD.**

Konzultant: **Dr. Stefan Weber**

Cíl práce:

Cílem práce je implementovat novou okrajovou podmíinku v PIC simulačním kódu EPOCH (případně vytvořit za tímto účelem zvláštní program), která umožní simulaci krátkého intenzivního laserového impulsu zaostřeného do ohniska menšího, než umožňuje paraxiální approximace. Tato okrajová podmínka bude otestována a použita v modelových simulacích, kde bude studován vliv zaostření laserového impulsu na průběh laserové interakce s plazmatem.

Pokyny pro vypracování:

- 1) Seznamte se s fyzikou šíření a fokusace krátkých ultra-intenzivních laserových impulsů. Popište paraxiální approximaci a její omezení a vypracujte přehled možností zaostření laserových impulsů do velmi malého ohniska.

- 2) Připravte metodu pro zadání okrajové podmínky v PIC simulacích s kódem EPOCH, která umožní zaostření laserového impulsu do ohniska menšího než je střední vlnová délka laserového záření. Metodu implementujte a otestujte.
- 3) Pro vybrané případy provádějte simulace interakce laserového záření s plazmatem a popište kvantitativní a kvalitativní rozdíly v závislosti na velikosti ohniska.

Literatura:

- 1) P. Gibbon, *Short Pulse Laser Interactions with Matter*, Imperial College Press, London, 2005.
- 2) T. D. Arber et al., Contemporary particle-in-cell approach to laser-plasma modelling, *Plasma Physics and Controlled Fusion* 57, 113001 (2015).
- 3) A. Macchi, A Superintense Laser-Plasma Interaction Theory Primer, SpringerBriefs in Physics, Springer, Dordrecht (2013).
- 4) C. K. Birdsall, A. B. Langdon, *Plasma Physics via Computer Simulation*, Hilger, Bristol (1991).
- 5) I. Thiele et al., Boundary conditions for arbitrarily shaped and tightly focused laser pulses in electromagnetic codes, *Journal of Computational Physics* 321, 1110 (2016).
- 6) R. L. Garay-Avendaño et al., Exact analytic solutions of Maxwell's equations describing propagating nonparaxial electromagnetic beams, *Applied Optics* 53, 4524 (2014).
- 7) JX. Li. et al., Fields of an ultrashort tightly focused laser pulse, *Journal of the Optical Society of America B* 33, 405 (2016).

Datum zadání: říjen 2016

Datum odevzdání: 5.květen 2017

.....
Vedoucí katedry

.....
Děkan

Prohlášení/Declaration

Prohlašuji, že jsem předloženou práci vypracoval samostatně a že jsem uvedl veškerou použitou literaturu.

I hereby declare that I carried out this work independently, and only with the cited sources, literature and other professional sources.

V Praze dne/In Prague on

.....
Bc. Petr Valenta

Název práce: **Zaostření krátkého intenzivního laserového impulsu do velmi malého ohniska v částicových simulacích interakce s plazmatem**

Autor: Bc. Petr Valenta

Druh práce: Diplomová práce

Studijní program: (N3913) Aplikace přírodních věd

Obor: (3901T065) Informatická fyzika

Vedoucí práce: doc. Ing. Ondřej Klimo, Ph.D.
Katedra fyzikální elektroniky, Fakulta jaderná a fyzikálně inženýrská, České vysoké učení technické v Praze

Konzultant: Dr. Stefan Andreas Weber
Projekt ELI-Beamlines, Fyzikální ústav Akademie věd České republiky, v. v. i.

Abstrakt

Content...

Klíčová slova: fokuzace, PIC simulace, laser-plazma interakce, optika

Title: **Tight-focusing of short intense laser pulses in particle-in-cell simulations of laser-plasma interaction**

Author: Bc. Petr Valenta

Type of work: Master's thesis

Study programme: (N3913) Applications of Natural Sciences

Branch of study: (3901T065) Computational Physics

Supervisor: doc. Ing. Ondřej Klímo, Ph.D.
Department of Physical Electronics, Faculty of Nuclear Sciences
and Physical Engineering, Czech Technical University in Prague

Consultant: Dr. Stefan Andreas Weber
Project ELI-Beamlines, Institute of Physics of the Czech Academy
of Sciences

Abstract

Content...

Keywords: tight-focusing, PIC simulations, laser-plasma interaction, plasma optics

Contents

Introduction	11
1 Electromagnetic field	13
1.1 Maxwell's equations	13
1.2 Electrodynamic potentials	15
1.3 Hertz vectors	16
1.4 Energy and momentum	17
1.5 Electromagnetic waves and Gaussian beam	19
2 Laser-plasma interaction	23
2.1 Basic plasma parameters	23
2.2 Plasma description	25
2.3 Electromagnetic waves in plasmas	27
2.3.1 Unmagnetized plasmas	27
2.3.2 Magnetized plasmas	28
2.4 Ponderomotive force	31
2.4.1 Non-relativistic case	31
2.4.2 Relativistic case	33
2.5 Self-induced transparency (SIT)	34
2.6 Laser absorption and electron heating mechanisms	35
2.6.1 Resonance absorption	35
2.6.2 Brunel's vacuum heating	36
2.6.3 Relativistic $\mathbf{J} \times \mathbf{B}$ heating	36
2.7 Mechanisms of laser-driven ion acceleration	37
2.7.1 Radiation pressure acceleration (RPA)	37
2.7.2 Target normal sheath acceleration (TNSA)	38
3 Particle-in-cell (PIC) method	41
3.1 Mathematical derivation	41
3.2 Particle pusher	44
3.3 Field solver	46

3.4	Particle and field weighting	48
3.5	Stability and accuracy	49
3.6	Extendable PIC Open Collaboration (EPOCH)	49
4	Tight-focusing of laser pulses	53
4.1	Laser boundary conditions	53
4.2	Implementation	57
4.3	Evaluation	58
4.4	Overview of experimental methods	66
4.4.1	Off-axis parabolic mirror	66
4.4.2	Focusing plasma mirror	67
4.4.3	Plasma lens	68
4.4.4	Conical targets	69
5	2D simulations of focused laser beams	71
5.1	Simulation model and initial conditions	71
5.2	Simulation results	72
Conclusion		85
Bibliography		88
Appendices		93
A Input files		93
B Code listings		97
C CD content		113

Introduction

Since the first demonstration of pulsed laser in 1960 [s], the intensive research and development in the field of laser technology have seen a tremendous progress. Pulse compression and amplification techniques, such as CPA [s], OPCPA [s] and lately RBA [s], have enabled a generation of ultra-short laser pulses with intensities exceeding 10^{22} W/cm². Pulses in this regime provide an unprecedented capability for basic research (e.g. high-energy density physics, warm dense matter, plasma optics, laboratory astrophysics) as well as a broad range of groundbreaking applications in diverse fields (e.g. coherent diffractive imaging, X-ray diffraction and spectroscopy, production of compact sources for radiotherapy, inertial confinement fusion).

The peak laser intensities are typically increased by enhancing the produced laser properties, either by lowering the pulse duration or increasing the pulse energy. This approach comes at great cost since it requires a higher level of complexity for the laser chain [s]. More effective way to increase the laser intensity is to reduce the focal spot size. However, the conventional solid state optics are inappropriate in the case of tight-focusing (expensive, susceptible to damage from solid target debris, sensitive to small misalignments). Nevertheless, it seems that many drawbacks might be in future overcome by using a plasma-based focusing optics. Therefore, the interaction of tightly focused laser beams with matter is currently attracting much attention [s].

This work is structured as follows: the first chapter provides a brief introduction to the classical electromagnetic field theory, including the mathematical derivation of the paraxial Gaussian beam formula. The second chapter summarizes the elementary knowledge of plasma physics and physics of laser-plasma interaction. In the third chapter, one of the most popular numerical methods in plasma physics, particle-in-cell (PIC), is thoroughly discussed. The characteristics and features of the code EPOCH [4], which has been used for the simulations within this work, can be found in the last section of this chapter. The fourth chapter is devoted to the tight-focusing of laser pulses, including a description of algorithm for rigorous calculation of electromagnetic fields at boundaries of simulation domain. This chapter also contains the details about the implementation of the algorithm as well as thorough evaluation of its correctness and the correctness of the implementation. At the end, one may find the overview of currently used experimental methods for tight-focusing. The last chapter demonstrates the results of two-dimensional simulations of tightly focused laser

Introduction

beams interacting with solid targets.

Although the most convenient unit system for most plasma applications is the Gaussian cgs system, throughout this work the SI (System Internationale) units are used, unless explicitly stated. Symbols in bold represent vector quantities, and symbols in italics represent scalar quantities, unless otherwise indicated.

Chapter 1

Electromagnetic field

Since the laser beam is nothing but the superposition of electromagnetic waves with high spatial and temporal coherence, the opening chapter has to be logically devoted to the fundamental physical aspects of the classical electromagnetic field theory based on the Maxwell's equations. The chapter contains a brief description of the microscopic as well as the macroscopic variant of the Maxwell's equations and their general solutions exploiting electrodynamic potentials and Hertz vectors. A short part is devoted also to energy and momentum of the electromagnetic waves. In the last part, one finds the simplest mathematical description of the focused laser beam and corresponding conditions of its validity.

1.1 Maxwell's equations

The electromagnetic field is in theory represented by two vector quantities, the electric field intensity $\mathbf{E}(\mathbf{r}, t)$ and the magnetic induction $\mathbf{B}(\mathbf{r}, t)$. These vectors are finite and continuous functions of position \mathbf{r} and time t . The description of electromagnetic phenomena in classical electrodynamics is provided by the set of Maxwell's equations. The microscopic variant with external sources in vacuum is formulated as follows,

$$\nabla \cdot \mathbf{E} = \frac{\rho}{\varepsilon_0}, \quad (1.1)$$

$$\nabla \cdot \mathbf{B} = 0, \quad (1.2)$$

$$\nabla \times \mathbf{E} + \frac{\partial \mathbf{B}}{\partial t} = 0, \quad (1.3)$$

$$\nabla \times \mathbf{B} - \mu_0 \varepsilon_0 \frac{\partial \mathbf{E}}{\partial t} = \mu_0 \mathbf{J}, \quad (1.4)$$

where $\rho(\mathbf{r}, t)$ is total electric charge density and $\mathbf{J}(\mathbf{r}, t)$ is total electric current density due to the motion of charged particles. These quantities may be continuous as well as discrete.

As might be seen from the Maxwell's equations (1.1 - 1.4), the charge density is the source of the electric field, whilst the magnetic field is produced by the current density. The lack of symmetry in the equations (1.2, 1.3 are homogeneous) is caused by the experimental absence of magnetic charges and currents. The universal constants appearing in the Maxwell's equations (1.1, 1.4) are the electric permittivity of vacuum ε_0 and the magnetic permeability of vacuum μ_0 .

The first equation, 1.1, is Gauss's law for electric field in the differential form. It states that the flux of the electric field through any closed surface is proportional to the total charge inside. The second equation, 1.2, is Gauss's law for magnetic field. It expresses the fact that there are no magnetic monopoles, so the flux of magnetic field through any closed surface is always zero. The third equation, 1.3, is Faraday's law describing how the electric field is associated with a time varying magnetic field. And the last equation, 1.4, is Ampère's law with Maxwell's displacement current, which means that the time varying electric field causes the magnetic field. As a consequence, it predicts the existence of electromagnetic waves that can carry energy and momentum even in a free space.

To describe the effects of an electromagnetic field in the presence of macroscopic substances, the complicated distribution of charges and currents in matter over the atomic scale is not relevant. Thus one shall define a second set of auxiliary vectors that represent fields in which the material properties are already included in an average sense, the electric displacement $\mathbf{D}(\mathbf{r}, t)$ and the magnetic vector $\mathbf{H}(\mathbf{r}, t)$,

$$\mathbf{D} = \varepsilon_0 \mathbf{E} + \mathbf{P} = \varepsilon \mathbf{E}, \quad (1.5)$$

$$\mathbf{H} = \frac{\mathbf{B}}{\mu_0} - \mathbf{M} = \frac{\mathbf{B}}{\mu}, \quad (1.6)$$

where $\mathbf{P}(\mathbf{r}, t)$ and $\mathbf{M}(\mathbf{r}, t)$ are the vectors of polarization and magnetization, respectively. Note that the vectors of polarization and magnetization can be interpreted as a density of electric or magnetic dipole moment of the medium, therefore they are definitely associated with the state of a matter and vanish in vacuum. Similarly as in the case of free space, the factors ε and μ are called electric permittivity of medium and magnetic permeability of medium. In general case, ε and μ are tensors. The constitutive relations above (1.5, 1.6) hold only if the medium is homogeneous and isotropic. For the sake of simplicity, only such materials will be considered in the following text. The macroscopic variant of Maxwell's equations is formulated as follows,

$$\nabla \cdot \mathbf{D} = \rho, \quad (1.7)$$

$$\nabla \cdot \mathbf{B} = 0, \quad (1.8)$$

$$\nabla \times \mathbf{E} + \frac{\partial \mathbf{B}}{\partial t} = 0, \quad (1.9)$$

$$\nabla \times \mathbf{H} - \frac{\partial \mathbf{D}}{\partial t} = \mathbf{J}, \quad (1.10)$$

where $\rho(\mathbf{r}, t)$ and $\mathbf{J}(\mathbf{r}, t)$ now stand for only external electric charge and current density, respectively.

By combining the time derivative of the equation 1.7 with the divergence of the equation 1.10, one obtains the following relation between the electromagnetic field sources,

$$\frac{\partial \rho}{\partial t} + \nabla \cdot \mathbf{J} = 0. \quad (1.11)$$

The important result 1.11, which is frequently referred to as the equation of continuity, expresses nothing but the conservation of total electric charge in an isolated system. In other words, the time rate of change of the electric charge in any closed surface is balanced by the electric current flowing through the surface.

1.2 Electrodynamic potentials

The first-order partial differential Maxwell's equations can be effectively converted to a smaller number of second-order equations by introducing electrodynamic potentials. Hence, one can express the electric and magnetic field as follows,

$$\mathbf{E} = -\nabla\Phi - \frac{\partial \mathbf{A}}{\partial t}, \quad (1.12)$$

$$\mathbf{B} = \nabla \times \mathbf{A}, \quad (1.13)$$

where $\Phi(\mathbf{r}, t)$ is the scalar potential and $\mathbf{A}(\mathbf{r}, t)$ is the vector potential of the corresponding fields. One can clearly see that using the definitions 1.12, 1.13, six vector components are replaced by only four potential functions and two Maxwell's homogeneous equations (1.8, 1.9) are fulfilled identically.

However, by definitions 1.12, 1.13, $\Phi(\mathbf{r}, t)$ and $\mathbf{A}(\mathbf{r}, t)$ are not defined uniquely, thus an infinite number of potentials which lead to the same fields may be constructed. To avoid that, one has to impose a supplementary condition, for example

$$\nabla \cdot \mathbf{A} + \mu\varepsilon \frac{\partial \Phi}{\partial t} = 0. \quad (1.14)$$

The condition 1.14 is called the Lorenz gauge. Lorenz gauge is commonly used in electromagnetism because of its independence of the coordinate system. Furthermore, it leads to the following uncoupled equations,

$$\Delta\Phi - \mu\varepsilon \frac{\partial^2 \Phi}{\partial t^2} = -\frac{\rho}{\varepsilon}, \quad (1.15)$$

$$\Delta\mathbf{A} - \mu\varepsilon \frac{\partial^2 \mathbf{A}}{\partial t^2} = -\mu\mathbf{J}, \quad (1.16)$$

that are in all respects equivalent to the Maxwell's equations and in many situations much simpler to solve.

Equations 1.15, 1.16 correspond to the inhomogeneous wave equations for scalar potential $\Phi(\mathbf{r}, t)$ and vector potential $\mathbf{A}(\mathbf{r}, t)$. Their general solutions are given by the following expressions,

$$\Phi(\mathbf{r}, t) = \frac{1}{4\pi\epsilon} \int \frac{\rho(\mathbf{r}', t')}{\|\mathbf{r} - \mathbf{r}'\|} dV, \quad (1.17)$$

$$\mathbf{A}(\mathbf{r}, t) = \frac{\mu}{4\pi} \int \frac{\mathbf{J}(\mathbf{r}', t')}{\|\mathbf{r} - \mathbf{r}'\|} dV, \quad (1.18)$$

where dV is a volume element and $\|\cdot\|$ stands for the standard Euclidean norm. Note that the solutions 1.17, 1.18 are dependent only on charge and current densities at position \mathbf{r}' at so-called retarded time $t' = t - \sqrt{\mu\epsilon}\|\mathbf{r} - \mathbf{r}'\|$ which takes into account the finite velocity of the wave. In other words, the fields at the observation point \mathbf{r} at the time t are proportional to the sum of all the electromagnetic waves that leave the source elements at point \mathbf{r}' at the retarded time t' .

1.3 Hertz vectors

There exists also other possibilities how to express the electromagnetic field. Under ordinary conditions, an arbitrary electromagnetic field may be defined in terms of a single vector function. This may be helpful for solving of many problems of classical electromagnetic theory, particularly the wave propagation.

First, let us introduce the electric Hertz vector $\boldsymbol{\Pi}_e(\mathbf{r}, t)$ in terms of the scalar and vector potentials,

$$\Phi = -\nabla \cdot \boldsymbol{\Pi}_e, \quad (1.19)$$

$$\mathbf{A} = \mu\epsilon \frac{\partial \boldsymbol{\Pi}_e}{\partial t}. \quad (1.20)$$

Note that the definitions 1.19, 1.20 are consistent with the Lorenz gauge condition 1.14. In the absence of magnetization, it might be easily shown that $\mathbf{J} = \partial\mathbf{P}/\partial t$ and the electric Hertz vector $\boldsymbol{\Pi}_e(\mathbf{r}, t)$ is governed by an inhomogeneous wave equation

$$\Delta \boldsymbol{\Pi}_e - \mu\epsilon \frac{\partial^2 \boldsymbol{\Pi}_e}{\partial t^2} = -\frac{\mathbf{P}}{\epsilon}. \quad (1.21)$$

The equation 1.21 is of the same type as the equations 1.15, 1.16 and has therefore the familiar general solution

$$\boldsymbol{\Pi}_e(\mathbf{r}, t) = \frac{1}{4\pi\epsilon} \int \frac{\mathbf{P}(\mathbf{r}', t')}{\|\mathbf{r} - \mathbf{r}'\|} dV. \quad (1.22)$$

As might be seen from 1.22, the fields derived from the electric Hertz vector $\boldsymbol{\Pi}_e(\mathbf{r}, t)$

can be interpreted as being due to a density distribution of electric dipoles. Every solution of 1.22 then uniquely determines the electromagnetic field through

$$\mathbf{E} = \nabla (\nabla \cdot \boldsymbol{\Pi}_e) - \mu\epsilon \frac{\partial^2 \boldsymbol{\Pi}_e}{\partial t^2}, \quad (1.23)$$

$$\mathbf{B} = \mu\epsilon \left(\nabla \times \frac{\partial \boldsymbol{\Pi}_e}{\partial t} \right). \quad (1.24)$$

Second, one may introduce the magnetic Hertz vector $\boldsymbol{\Pi}_m(\mathbf{r}, t)$ in terms of the scalar and vector potentials by the following expressions,

$$\Phi = 0, \quad (1.25)$$

$$\mathbf{A} = \nabla \times \boldsymbol{\Pi}_m. \quad (1.26)$$

In the absence of polarization, $\mathbf{J} = \nabla \times \mathbf{M}$ and the magnetic Hertz vector $\boldsymbol{\Pi}_m(\mathbf{r}, t)$ defined by 1.25 and 1.26 fulfills an inhomogeneous wave equation

$$\Delta \boldsymbol{\Pi}_m - \mu\epsilon \frac{\partial^2 \boldsymbol{\Pi}_m}{\partial t^2} = -\mu\mathbf{M}. \quad (1.27)$$

As for the previous cases, one may easily find the solution of 1.27,

$$\boldsymbol{\Pi}_m(\mathbf{r}, t) = \frac{\mu}{4\pi} \int \frac{\mathbf{M}(\mathbf{r}', t')}{\|\mathbf{r} - \mathbf{r}'\|} dV, \quad (1.28)$$

thus the fields derived from the magnetic Hertz vector $\boldsymbol{\Pi}_m(\mathbf{r}, t)$ may be imagined to be due to a density distribution of magnetic dipoles. Again, every solution of 1.28 uniquely determines the electromagnetic field via

$$\mathbf{E} = \nabla \times \frac{\partial \boldsymbol{\Pi}_m}{\partial t}, \quad (1.29)$$

$$\mathbf{B} = \nabla \times (\nabla \times \boldsymbol{\Pi}_m). \quad (1.30)$$

Note that the above derivations considered electric and magnetic Hertz vectors as a separate quantities. It is also possible, however, to introduce them together in the form of one six-vector [source].

1.4 Energy and momentum

To be able to describe the interaction of the electromagnetic field with matter, one has to know the energy distribution throughout the field as well as the momentum balance.

By scalar multiplications of 1.9 by $\mathbf{H}(\mathbf{r}, t)$ and of 1.10 by $\mathbf{E}(\mathbf{r}, t)$, following subtraction of both obtained equations and using standard vector identities, one gets the expression

$$\mathbf{E} \cdot \frac{\partial \mathbf{D}}{\partial t} + \mathbf{H} \cdot \frac{\partial \mathbf{B}}{\partial t} + \nabla \cdot (\mathbf{E} \times \mathbf{H}) = -\mathbf{E} \cdot \mathbf{J}. \quad (1.31)$$

The equation 1.31 can be rewritten in the form of conservation law,

$$\frac{\partial u}{\partial t} + \nabla \cdot \mathbf{S} = -\mathbf{E} \cdot \mathbf{J}, \quad (1.32)$$

where

$$u = \frac{1}{2} (\mathbf{E} \cdot \mathbf{D} + \mathbf{H} \cdot \mathbf{B}), \quad \mathbf{S} = \mathbf{E} \times \mathbf{H}. \quad (1.33)$$

The quantity $u(\mathbf{r}, t)$ in 1.33 describes the total energy density in the field and $\mathbf{S}(\mathbf{r}, t)$ is so-called Poynting vector which represents, in the equation 1.32, the energy flow of the field per unit area. Note that the Poynting vector points in the same direction as the vector of the wave propagation.

The important statement 1.32, also referred to as the Poynting theorem, expresses the energy balance for the electromagnetic field. In other words, the time rate of change of the field energy within a certain region and the energy flowing out of that region is balanced by the conversion of the electromagnetic energy into mechanical or heat energy.

Besides energy, the electromagnetic wave can carry also momentum. To derive a balance of linear momentum, one has to know the way how charges and currents interact with the electromagnetic field. This is described by the Lorentz force the density $\mathbf{f}_L(\mathbf{r}, t)$ of which is given by the following expression,

$$\mathbf{f}_L = \rho \mathbf{E} + \mathbf{J} \times \mathbf{B}. \quad (1.34)$$

Thus the electric and magnetic fields can be regarded as a forces produced by charge and current densities.

By replacing sources in 1.34 using macroscopic Maxwell's equations 1.7, 1.10, one may express the density of Lorentz force $\mathbf{f}_L(\mathbf{r}, t)$ entirely in terms of fields,

$$\mathbf{f}_L = (\nabla \cdot \mathbf{D}) \mathbf{E} + (\nabla \times \mathbf{H}) \times \mathbf{B} - \frac{\partial \mathbf{D}}{\partial t} \times \mathbf{B}. \quad (1.35)$$

Note that the last term on the right hand side of 1.35 can be rewritten using the Poynting vector $\mathbf{S}(\mathbf{r}, t)$ derived above,

$$\frac{\partial \mathbf{D}}{\partial t} \times \mathbf{B} = \varepsilon \mu \frac{\partial \mathbf{S}}{\partial t} + \mathbf{D} \times (\nabla \times \mathbf{E}). \quad (1.36)$$

By plugging 1.36 into 1.35 and employing basic vector calculus identities, one eventually gets

the expression for the linear momentum balance in the form of conservation law,

$$\frac{\partial \mathbf{g}}{\partial t} + \nabla \cdot \mathbb{T} = -\mathbf{f}_L, \quad (1.37)$$

where

$$\mathbf{g} = \mathbf{D} \times \mathbf{B}, \quad T_{ij} = -E_i D_j - H_i B_j + \frac{1}{2} (\mathbf{E} \cdot \mathbf{D} + \mathbf{H} \cdot \mathbf{B}) \delta_{ij}. \quad (1.38)$$

The quantity $\mathbf{g}(\mathbf{r}, t)$ in 1.37 may be interpreted as the density of linear electromagnetic momentum and $\mathbb{T}(\mathbf{r}, t)$ is so-called Maxwell stress tensor which represents, the momentum flow per unit area in the equation 1.37. The symbol δ_{ij} in 1.38 stands for the Kronecker delta.

The important statement 1.37, which expresses the linear momentum balance for electromagnetic field, may be used to calculate the electromagnetic forces that act on objects or particles within that field. Notice that the contribution of the electromagnetic field to energy and momentum is completely characterized by the fluxes of $\mathbf{S}(\mathbf{r}, t)$ and $\mathbb{T}(\mathbf{r}, t)$.

1.5 Electromagnetic waves and Gaussian beam

In this section, the simplest mathematical description of a focused laser beam based on approximations to the wave equation is deduced. Since in numerical codes it is a common practice to prescribe the laser beams by their propagation in free space, the set of the microscopic Maxwell's equations 1.1 - 1.4 will be exploited.

In the absence of external sources, it might be easily shown that the equations 1.1 - 1.4 may be alternatively formulated as an uncoupled homogeneous wave equations for electric field $\mathbf{E}(\mathbf{r}, t)$ and magnetic field $\mathbf{B}(\mathbf{r}, t)$,

$$\Delta \mathbf{E} - \frac{1}{c^2} \frac{\partial^2 \mathbf{E}}{\partial t^2} = 0, \quad (1.39)$$

$$\Delta \mathbf{B} - \frac{1}{c^2} \frac{\partial^2 \mathbf{B}}{\partial t^2} = 0, \quad (1.40)$$

where the universal constant $c = 1/\sqrt{\mu_0 \epsilon_0}$ is the speed of light in vacuum, which leads to the essential fact, that the electromagnetic waves propagate in vacuum with the velocity of light c . However, the wave equations 1.39, 1.40 do not provide all the information about the electric and magnetic field of the wave. There are further constraints due to Maxwell's equations restricting the orientation and proportional magnitudes of the fields. From the set 1.1 - 1.4, it might be clearly seen that $\mathbf{E}(\mathbf{r}, t)$ and $\mathbf{B}(\mathbf{r}, t)$ must be mutually perpendicular to each other as well as to the direction of the wave propagation.

Without any loss of generality, consider the laser beam as a monochromatic electromagnetic wave propagating toward the positive direction of the z-axis. In many standard

references [source], the description of such a wave is given by the evolution of a single electric field component linearly polarized along the x-axis of the Cartesian coordinate system (although the more proper way would be to use the vector potential [source]), therefore one has to look for the solution of the equation 1.39.

According to the previous assumptions, the solution is expected to be in the form of the following plane wave,

$$\mathbf{E}(\mathbf{r}_\perp, z, t) = \Re E_0 \Psi(\mathbf{r}_\perp, z) e^{i(k_z z - \omega t)} \hat{\mathbf{e}}_x, \quad (1.41)$$

where $\mathbf{r}_\perp = (x, y)^T$ is the vector of transverse Cartesian coordinates, symbol \Re stands for the real part of the complex quantity, E_0 is a constant amplitude, $\Psi(\mathbf{r}_\perp, z)$ is the part of the wave function which is dependent only on the spatial coordinates, ω denotes the angular frequency, k_z is the z-component of the wave vector $\mathbf{k}(\omega)$, i denotes the imaginary unit and $\hat{\mathbf{e}}_x$ is the unit vector pointing in the direction of the x-axis.

Direct substitution of expression 1.41 into the equation 1.39 yields the time-independent form of the scalar wave equation

$$\Delta \Psi(\mathbf{r}_\perp, z) + 2ik_z \frac{\partial \Psi(\mathbf{r}_\perp, z)}{\partial z} = 0. \quad (1.42)$$

The equation 1.42 is called the Helmholtz equation. Note that it is sufficient to seek solutions to the equation 1.42 since the wave 1.41 is monochromatic.

It turned out, that the geometry of the focused laser beam can be expressed in terms of the laser wavelength λ and the following three parameters,

$$w_0, \quad z_R = \frac{k_z w_0^2}{2} = \frac{\pi w_0^2}{\lambda}, \quad \Theta = \frac{w_0}{z_R} = \frac{\lambda}{\pi w_0}. \quad (1.43)$$

The parameter w_0 in 1.43 is the beam waist, defined as a radius at which the laser intensity fall to $1/e^2$ of its axial value at the focal spot. The second parameter, z_R , is so-called Rayleigh range which is a distance in the longitudinal direction from the focal spot to the point where the beam radius is $\sqrt{2}$ larger than the beam waist w_0 . And the last parameter, Θ , is the divergence angle of the beam that represents the ratio of transverse and longitudinal extent.

Because of the symmetry about the longitudinal axis of the equation 1.42, the following calculations may be made simpler by introducing a dimensionless cylindrical coordinates that use the parameters 1.43,

$$\rho = \frac{\|\mathbf{r}_\perp\|}{w_0}, \quad \zeta = \frac{z}{z_R}. \quad (1.44)$$

After performing a transformation of coordinates, the Helmholtz equation 1.42 becomes

$$\frac{1}{\rho} \frac{\partial}{\partial \rho} \left(\rho \frac{\partial \Psi(\rho, \zeta)}{\partial \rho} \right) + 4i \frac{\partial \Psi(\rho, \zeta)}{\partial \zeta} = -\Theta^2 \frac{\partial^2 \Psi(\rho, \zeta)}{\partial \zeta^2}. \quad (1.45)$$

In the following calculations, the beam divergence angle Θ is assumed to be small ($\Theta \ll 1$),

thus it can be used as an expansion parameter for Ψ and the solution of 1.45 will always be consistent,

$$\Psi = \sum_{n=0}^{+\infty} \Theta^{2n} \Psi_{2n}. \quad (1.46)$$

Next, one shall insert 1.46 into 1.45 and collect the terms with the same power of Θ . Then the zeroth-order function Ψ_0 obeys the following equation,

$$\frac{1}{\rho} \frac{\partial}{\partial \rho} \left(\rho \frac{\partial \Psi_0(\rho, \zeta)}{\partial \rho} \right) + 4i \frac{\partial \Psi_0(\rho, \zeta)}{\partial \zeta} = 0. \quad (1.47)$$

The equation 1.47, which is called the paraxial Helmholtz equation, is the starting point of traditional Gaussian beam theory. One can expect the solution of 1.47 in the form of a Gaussian function with a width varying along the longitudinal direction, thus

$$\Psi_0(\rho, \zeta) = h(\zeta) e^{-f(\zeta)\rho^2}, \quad (1.48)$$

where $f(\zeta)$ and $h(\zeta)$ are unknown complex functions that have to satisfy a condition $f(0) = h(0) = 1$. After plugging 1.48 into 1.47, one gets the following equation,

$$-f(\zeta)h(\zeta) + i \frac{dh(\zeta)}{d\zeta} + \rho^2 h(\zeta) \left(f(\zeta)^2 - i \frac{df(\zeta)}{d\zeta} \right) = 0. \quad (1.49)$$

Since the equation 1.49 has to hold for arbitrary value of ρ , one may find two independent equations that are equivalent to 1.49

$$\frac{1}{f(\zeta)^2} \frac{df(\zeta)}{d\zeta} + i = 0, \quad \frac{1}{f(\zeta)h(\zeta)} \frac{dh(\zeta)}{d\zeta} + i = 0. \quad (1.50)$$

It might be easily shown, that under specified conditions the solutions of equations 1.50 have to be

$$h(\zeta) = f(\zeta), \quad f(\zeta) = \frac{1}{\sqrt{1+\zeta^2}} e^{-i \arctan \zeta}, \quad (1.51)$$

and therefore the complete expression for the zeroth-order wave function $\Psi_0(\rho, \zeta)$ is

$$\Psi_0(\rho, \zeta) = \frac{1}{\sqrt{1+\zeta^2}} \exp \left[-\frac{\rho^2}{1+\zeta^2} + i \left(\frac{\rho^2 \zeta}{1+\zeta^2} - \arctan \zeta \right) \right]. \quad (1.52)$$

In many situations, it is also useful to evaluate the expression 1.52 in terms of Cartesian coordinates, in which the zeroth-order wave function $\Psi_0(\mathbf{r}_\perp, z)$ is

$$\Psi_0(\mathbf{r}_\perp, z) = \frac{w_0}{w(z)} \exp \left[-\frac{\mathbf{r}_\perp^2}{w(z)^2} + i \left(k_z \frac{\mathbf{r}_\perp^2}{2R(z)} - \varphi_G(z) \right) \right], \quad (1.53)$$

where the parameters used to simplify the expression 1.53 are defined as

$$w(z) = w_0 \sqrt{1 + \left(\frac{z}{z_R}\right)^2}, \quad R(z) = z \left[1 + \left(\frac{z_R}{z}\right)^2\right], \quad \varphi_G(z) = \arctan\left(\frac{z}{z_R}\right). \quad (1.54)$$

One shall discuss the physical meaning of the three parameters 1.54. The function $w(z)$ represents the spot size parameter of the beam, that is the radius at which the laser intensity fall to $1/e^2$ of its axial value at any position z along the beam propagation. Note that the minimum of the spot size $w(0) = w_0$, consequently the focal spot is stationary and located at the origin of a Cartesian coordinate system. The second parameter, $R(z)$ is known to be the radius of curvature of the beam's wavefront at any position z along the beam propagation. Note that $\lim_{z \rightarrow 0^\pm} R(z) = \pm\infty$, therefore the beam behaves like a plane wave at focus as required. The last parameter, $\varphi_G(z)$, is the so-called Guoy phase of the beam at any position z along the beam propagation, which describes a phase shift in the wave as it passes through the focal spot.

Finally, by substituting 1.53 for $\Psi(\mathbf{r}_\perp, z)$ in 1.41 and taking the real part of that complex quantity, one obtains the electric field of the so-called paraxial Gaussian beam,

$$\mathbf{E}(\mathbf{r}_\perp, z, t) = E_0 \frac{w_0}{w(z)} \exp\left(-\frac{\mathbf{r}_\perp^2}{w(z)^2}\right) \cos\left(\omega t - k_z \left(z + \frac{\mathbf{r}_\perp^2}{2R(z)}\right) + \varphi_G(z)\right) \hat{\mathbf{e}}_x. \quad (1.55)$$

Although the electric field 1.55 describes the main features of the focused laser beam, it might be clearly seen that it does not satisfy Gauss's law (1.1). The correct electric field cannot vary with the direction of its polarization or has to have at least two non-zero vector components. To fix that, one would have to solve the wave equation for the vector potential 1.16 and afterwards exploit the solution to deduce all components of the electric and magnetic fields.

In addition, since one assumed $\Theta \ll 1$, the solution 1.55 is not accurate for strongly diverging beams. Since the divergence angle is inversely proportional to the beam waist, the previous condition yields $w_0 \gg \lambda$. In other words, it means that 1.55 is not valid for tightly focused laser beams and the need may arise for higher-order corrections.

Chapter 2

Laser-plasma interaction

When a high-power laser pulse is focused onto the surface of a solid target, a high density plasma layer is produced almost immediately due to the presence of strong electromagnetic fields. The dense plasma expanding from the target surface forms a density profile and the laser-plasma interaction takes place in its lower density part. Many different and often non-linear processes are involved in the laser-plasma interaction. A brief introduction to this field of research, which is rich both in physics and in applications, is provided in this chapter.

2.1 Basic plasma parameters

Plasma, one of the four fundamental states of matter, is a quasi-neutral gas of charged and neutral particles which exhibits collective behavior [source]. It is necessary to better explain some terms used in this definition.

By collective behavior one means motion that depends not only on local conditions but on the state of the plasma in remote regions as well. As charged particles move around, they can generate local concentrations of positive or negative charge, which give rise to electric fields. Motion of charges also generates currents, and hence magnetic fields. These fields affect the motion of other charged particles far away [source]. Thus, the plasma supports a wide range of possible motions.

Quasi-neutrality describes the apparent charge neutrality of a plasma over large volumes, while at smaller scales, there can be charge imbalance, which may give rise to local electric fields. This fact can be expressed mathematically as

$$\sum_s q_s n_s \approx 0, \quad (2.1)$$

where q_s and n_s is, respectively, the charge and density of particles of species s . The index of summation is taken over all the particle species of given system.

One of the most important parameters, which allows to predict the behavior of plasmas

more accurately, is the degree of its ionization. For a gas containing only single atomic species in thermodynamic equilibrium, the ionization can be clearly recognized from the Saha-Langmuir equation, which is most commonly written in the following form [source],

$$\frac{n_{k+1}}{n_k} = \frac{2}{n_e h^3} (2\pi m_e k_B T)^{\frac{3}{2}} \frac{g_{k+1}}{g_k} \exp\left(-\frac{\varepsilon_{k+1} - \varepsilon_k}{k_B T}\right). \quad (2.2)$$

Here n_k is the density of atoms in the k -th state of ionization, n_e is the electron density, m_e stands for the mass of electron, k_B is Boltzmann's constant, T is the gas temperature, h is Planck's constant, g_k is the degeneracy of the energy level for ions in the k -th state and ε_k is the ionization energy of the k -th level. From the equation (2.2), it may be clearly seen that the fully ionized plasmas exist only at high temperatures. This is the main reason why plasmas do not occur naturally on Earth (with a few exceptions).

A fundamental characteristics of the plasma behavior is its ability to shield out the electric potentials that are applied to it. Therefore, another important quantity λ_{Ds} , which is called the Debye length of species s , is defined as,

$$\lambda_{Ds} = \sqrt{\frac{\varepsilon_0 k_B T_s}{q_s^2 n_s}}. \quad (2.3)$$

The physical constant T_s denotes the temperature of the particles of species s . It often happens that a different species of particles in plasma have separate distributions with different temperatures, although each species can be in its own thermal equilibrium. The Debye length is a measure of the shielding distance or thickness of the sheath.

In plasma, each particle tries to gather its own shielding cloud. The previously mentioned concept of Debye shielding is valid only if there are enough particles in that cloud. Therefore, another important dimensionless number N_{Ds} , which is called plasma parameter of species s , is established. This parameter is defined as the average number of particles of species s in a plasma contained within a sphere of radius equal to the Debye length, thus

$$N_{Ds} = \frac{4}{3} \pi n_s \lambda_{Ds}^3. \quad (2.4)$$

Charge separation in plasma results in a typical harmonic electrostatic oscillations of charged particles described by the plasma frequency. One may define the plasma frequency for particles of species s ,

$$\omega_{ps} = \sqrt{\frac{q_s^2 n_s}{\varepsilon_0 m_s}}, \quad (2.5)$$

Note that as the ions are much heavier than electrons, they do not respond to the high frequency oscillations of the laser electric field. In many of the phenomena described in this chapter, the ions are treated as an immobile, uniform, neutralizing background. However, if

the frequency of external radiation source or the waves induced in plasmas is close to the ion plasma frequency, the ion motion must also be included. An example may be a stimulated Brillouin scattering.

A typical charged particle in plasma simultaneously undergoes Coulomb collisions with all the other particles in the Debye sphere. The importance of collisions is described by the collision frequency ν_c , which is the inverse of the mean time that it takes for a particle to significantly change its momentum due to collisions. The electron-ion collision frequency ν_{ei} is given by the following relation [source],

$$\nu_{ei} = \frac{Ze^4 n_e}{4\pi\epsilon_0^2 m_e^2 v^3} \ln \Lambda, \quad \Lambda = \frac{\lambda_D}{b_0}. \quad (2.6)$$

The coefficient Z denotes the charge number, v is relative velocity of colliding particles and $\ln \Lambda$ is the so-called Coulomb logarithm. It is ratio of the Debye to Landau length. Landau length b_0 is the impact parameter at which the scattering angle in the center of mass frame is 90° . For many plasmas of interest Coulomb logarithm takes on values between $5 - 15$. In plasma, a single Coulomb collision rarely results in a large deflection. The cumulative effect of the many random small angle collisions, however, is often larger than the effect of the few large angle collisions. Notice that the collision frequency ν_{ei} is proportional to v^{-3} , therefore the effect of collisions in hot plasmas is usually weak.

In a constant and uniform magnetic field, one can find that a charged particle spirals in a helix about the magnetic field line. This helix defines a fundamental time unit and distance scale,

$$\omega_{cs} = \frac{|q_s| \|\mathbf{B}\|}{m_s}, \quad r_{Ls} = \frac{v_\perp}{\omega_{cs}}. \quad (2.7)$$

These are called the cyclotron frequency ω_{cs} and the Larmor radius r_{Ls} of species s . Here v_\perp is a positive constant denoting the speed in the plane perpendicular to \mathbf{B} .

2.2 Plasma description

There exist three different approaches to plasma physics. The particle theory, the kinetic theory and the hydrodynamic theory. Each approach has some advantages and limitations that stem from the simplified assumptions appropriate only for certain phenomena and time scales. Note that the coupling with the Maxwell's equations is usually straightforward, therefore the corresponding relations are not mentioned here. In the following three subsections, all the approaches are briefly discussed.

The time evolution of the system containing charged particles in plasma is influenced by the electromagnetic fields formed due to the motion of particles as well as the external fields (e.g. laser). The particle approach is based on solving the equations of motion for all the particles in the system. In this case, the motion of particles is governed by the Newton's

equations with the Lorentz force,

$$m_s \frac{d^2\mathbf{r}}{dt^2} = q_s (\mathbf{E} + \mathbf{v} \times \mathbf{B}). \quad (2.8)$$

Note that the equation 2.8 holds only for non-relativistic particles.

The particle theory is useful for tracking a single particle motion in prescribed electromagnetic field. Obviously, the general solution for the system of charged particles using this approach can be complicated since the plasma typically consist of a large number of such particles interacting with the self-consistent field. However, the full analysis for certain cases may be applied with the help of computing infrastructures and particle simulation codes.

The plasma kinetic theory takes into account the motion of all charged particles in the system as well. However, the evolution of such system is not described by the exact motion of the particles, but only via certain average properties. The kinetic theory is based on a set of equations for the distribution function $f_s(\mathbf{x}, \mathbf{v}, t)$ of particles of species s in plasma. The distribution function may be interpreted as a statistical description of a large number of interacting particles in the system. If collisions can be neglected (for example in hot plasmas), the distribution function is governed by the collisionless Vlasov equation,

$$\frac{\partial f_s}{\partial t} + \mathbf{v} \cdot \nabla f_s + \frac{q_s}{m_s} (\mathbf{E} + \mathbf{v} \times \mathbf{B}) \cdot \frac{\partial f_s}{\partial \mathbf{v}} = 0. \quad (2.9)$$

The Vlasov equation 2.9 is obtained only by making the assumption that the particle density is conserved in the phase space, such that the time rate of change in a phase-space volume is equal to the flux of particles in or out of that volume. Due to its simplicity, the equation 2.9 is probably the most commonly used equation in the kinetic theory. However, the assumption to neglect collisions in a plasma is not valid generally. If it is necessary to take them into account, the collision term can be approximated using several methods [source].

In spite of the fact that the hydrodynamic theory is the roughest approximation for the description of plasma, it is sufficiently accurate to describe the majority of observed phenomena. The velocity distribution of each species is assumed to be Maxwellian everywhere, so the dependent variables are functions of only space and time coordinates. In other words, the fluid equations are the first three moments of the Vlasov equation (2.9). These yield the following hydrodynamic equations for the density, momentum and the energy,

$$\frac{\partial n_s}{\partial t} + \nabla \cdot (n_s \mathbf{u}_s) = 0, \quad (2.10)$$

$$m_s n_s \left[\frac{\partial \mathbf{u}_s}{\partial t} + (\mathbf{u}_s \cdot \nabla) \mathbf{u}_s \right] + \nabla \cdot \mathbb{P}_s = q_s n_s (\mathbf{E} + \mathbf{u}_s \times \mathbf{B}), \quad (2.11)$$

$$\frac{\partial}{\partial t} \left(\frac{1}{2} n_s m_s u_s^2 + e_s \right) + \nabla \cdot \left(\frac{1}{2} n_s m_s u_s^2 \mathbf{u}_s + e_s \mathbf{u}_s + \mathbb{P}_s \mathbf{u}_s + \mathbf{Q}_s \right) = q_s n_s \mathbf{u}_s \cdot \mathbf{E}. \quad (2.12)$$

The zeroth-order moment (2.10) yields the continuity equation, where $\mathbf{u}_s(\mathbf{x}, t)$ is the velocity of the fluid of species s . This equation essentially states that the total number of particles is conserved. The first-order moment (2.11) leads to a momentum equation. Here $\mathbb{P}_s(\mathbf{x}, t)$ is the pressure tensor. This comes about by separating the particle velocity into the fluid and a thermal component of velocity. The thermal velocity then leads to the pressure term. Finally, the second-order moment (2.12) corresponds to the energy equation, where e_s is the density of the internal energy and \mathbf{Q}_s describes the heat flux density.

It might be clearly seen that the moment equations do not form a closed system. For the system of equations 2.10 - 2.12 to be complete, it has to be supplemented by the equation of state, which describes the relation between pressure and density in the plasma. However, the equations of state are well defined only in local thermodynamic equilibrium. Otherwise, the system cannot provide sufficiently exact description and thus the fluid equations 2.10 - 2.12 are not appropriate. Note that if the magnetic field is dominant in plasma, the set of hydrodynamic equations 2.10 - 2.12 should be replaced by the equations of magnetohydrodynamics [source].

2.3 Electromagnetic waves in plasmas

In laser-plasma interaction, the knowledge how the laser beam propagates through plasma is essential. Therefore, a general properties of the electromagnetic wave propagation in plasmas are closer described in this section. One can find the characteristics of propagation in both, unmagnetized as well as magnetized plasma. Particularly, in the case of magnetized plasmas, the waves traveling parallel to and perpendicular to a constant magnetic field are discussed in greater detail.

2.3.1 Unmagnetized plasmas

To derive the dispersion relation of electromagnetic wave propagating through unmagnetized plasmas, the hydrodynamic approach is exploited. Since one assumes plasma response to a high frequency field, the ions are treated as a stationary, neutralizing background. Thermal motion of particles is also ignored, thus the pressure term in 2.11 can be neglected. One also needs the wave equation for the electric field 1.39. However, it is now necessary to include the current density due to motion of charged particles in plasma. The hydrodynamic equations are coupled with the Maxwell's equations via $\mathbf{J} = q_s n_s \mathbf{u}_s$, thus one shall solve the following set of equation,

$$m_e n_e \left[\frac{\partial \mathbf{u}_e}{\partial t} + (\mathbf{u}_e \cdot \nabla) \mathbf{u}_e \right] = -en_e \mathbf{E}, \quad (2.13)$$

$$\Delta \mathbf{E} - \frac{1}{c^2} \frac{\partial^2 \mathbf{E}}{\partial t^2} = -\mu_0 en_e \frac{\partial \mathbf{u}_e}{\partial t}. \quad (2.14)$$

The system of equations above will be linearized using the methods of perturbation theory. Consider a small perturbations from the stationary state,

$$\mathbf{u}_e = \mathbf{u}_{e0} + \delta\mathbf{u}_e, \quad \mathbf{E} = \mathbf{E}_0 + \delta\mathbf{E}, \quad (2.15)$$

where \mathbf{u}_{e0} and \mathbf{E}_0 are obviously identically equal to zero vector. After substituting perturbed quantities 2.15 into initial system of equations and performing Fourier transform one obtains

$$\delta\mathbf{u}_e = -i\frac{e}{\omega m_e}\delta\mathbf{E}, \quad (2.16)$$

$$\delta\mathbf{E} = i\frac{\omega e n_{e0}}{\varepsilon_0(\omega^2 - c^2 k^2)}\delta\mathbf{u}_e. \quad (2.17)$$

Eliminating $\delta\mathbf{u}_e$ from the equation 2.17 one gets the equation for perturbation of the electric field,

$$(\omega^2 - \omega_{pe}^2 - c^2 k^2)\delta\mathbf{E} = 0. \quad (2.18)$$

The equation 2.18 is the dispersion relation of the electromagnetic wave in plasma. To describe how the electromagnetic waves propagates through given medium, it is useful to introduce the index of refraction $N(\omega) = ck(\omega)/\omega$. Consequently, the dispersion relation may be rewritten as

$$N^2 = 1 - \left(\frac{\omega_{pe}}{\omega}\right)^2. \quad (2.19)$$

The important properties of the waves are distinguished by their cut-offs ($N \rightarrow 0$) and resonances ($N \rightarrow \infty$). In the vicinity of the resonance there is a total absorption, at a cut-off frequency there is a total reflection of incident waves.

In the case of the electromagnetic wave propagating through unmagnetized plasma, it might be clearly seen that there are no resonances. On the other hand, the equation 2.19 exhibits cut-off and the corresponding frequency (including ions) is given by the following expression,

$$\omega = \sqrt{\omega_{pe}^2 + \omega_{pi}^2} \quad (2.20)$$

The condition 2.20 occurs at the so-called critical plasma density $n_c(\omega)$. Note that the electromagnetic wave with frequency ω passing through plasma with densities larger than $n_c(\omega)$ is exponentially damped.

2.3.2 Magnetized plasmas

Next, consider the electromagnetic wave propagating through magnetized plasmas. To derive the dispersion relation, one may use similar treatment as in the previous subsection. The only difference is, that it is now necessary to include the effect of magnetic field. To obtain the wave equations for the oscillating electric and magnetic field, Faraday's law (1.3) and Ampere's

law (1.4) are needed. The system of equations described above will be again linearized using a small perturbations from the stationary state,

$$\mathbf{u}_e = \mathbf{u}_{e0} + \delta\mathbf{u}_e, \quad \mathbf{B} = \mathbf{B}_0 + \delta\mathbf{B}, \quad \mathbf{E} = \mathbf{E}_0 + \delta\mathbf{E}. \quad (2.21)$$

As in the previous case, \mathbf{u}_{e0} and \mathbf{E}_0 are identically equal to zero vector. After substituting perturbed quantities (2.21) into the initial system of equations and performing Fourier transform one obtains

$$\delta\mathbf{u}_e = -i\frac{e}{m_e\omega}\delta\mathbf{E} - i\frac{e}{m_e\omega}\delta\mathbf{u}_e \times \mathbf{B}_0, \quad (2.22)$$

$$\delta\mathbf{B} = \frac{1}{\omega}\mathbf{k} \times \delta\mathbf{E}, \quad (2.23)$$

$$\delta\mathbf{E} = -\frac{1}{\varepsilon_0\mu_0\omega}\mathbf{k} \times \delta\mathbf{B} + i\frac{en_0}{\varepsilon_0\omega}\delta\mathbf{u}_e. \quad (2.24)$$

Eliminating $\delta\mathbf{B}$ and $\delta\mathbf{u}_e$ from the equation 2.24 one gets the equation for perturbation of the electric field,

$$\begin{aligned} & (\omega^2 - \omega_{pe}^2 - c^2k^2)\delta\mathbf{E} + i\frac{\omega_{ce}}{\omega}(\omega^2 - c^2k^2)\delta\mathbf{E} \times \mathbf{e}_B + \\ & + c^2(\mathbf{k} \cdot \delta\mathbf{E})\mathbf{k} + i\frac{\omega_{ce}}{\omega}c^2(\mathbf{k} \cdot \delta\mathbf{E})\mathbf{k} \times \hat{\mathbf{e}}_B = 0. \end{aligned} \quad (2.25)$$

Here $\hat{\mathbf{e}}_B = \mathbf{B}_0/B_0$ is a unit vector in the direction of the magnetic field. If one choose, without the loss of generality, the coordinate system where $\mathbf{B}_0 = (0, 0, B_0)$ and $\mathbf{k} = (k \sin \alpha, 0, k \cos \alpha)$, one obtains the equation $\mathbb{M} \cdot \delta\mathbf{E} = 0$ with the matrix

$$\mathbb{M} = \begin{pmatrix} \omega^2 - \omega_{pe}^2 - c^2k^2 \cos^2 \alpha & i\frac{\omega_{ce}}{\omega}(\omega^2 - c^2k^2) & c^2k^2 \cos \alpha \sin \alpha \\ -i\frac{\omega_{ce}}{\omega}(\omega^2 - c^2k^2 \cos^2 \alpha) & \omega^2 - \omega_{pe}^2 - c^2k^2 & -i\frac{\omega_{ce}}{\omega}c^2k^2 \cos \alpha \sin \alpha \\ c^2k^2 \cos \alpha \sin \alpha & 0 & \omega^2 - \omega_{pe}^2 - c^2k^2 \sin^2 \alpha \end{pmatrix}. \quad (2.26)$$

The system of equations has non-trivial solution if and only if $\det(\mathbb{M}) = 0$. This condition leads to the desired dispersion relation for an arbitrary angle α ,

$$\begin{aligned} & \left[(\omega^2 - \omega_{pe}^2 - c^2k^2 \cos^2 \alpha)(\omega^2 - \omega_{pe}^2 - c^2k^2 \alpha) - \left(\frac{\omega_{ce}}{\omega}\right)^2(\omega^2 - c^2k^2)(\omega^2 - c^2k^2 \cos^2 \alpha) \right] \\ & (\omega^2 - \omega_{pe}^2 - c^2k^2 \sin^2 \alpha) - c^4k^4 \cos^2 \alpha \sin^2 \alpha \left[(\omega^2 - \omega_{pe}^2 - c^2k^2) - \left(\frac{\omega_{ce}}{\omega}\right)^2(\omega^2 - c^2k^2) \right] = 0. \end{aligned} \quad (2.27)$$

Wave	Cut-offs	Resonances
R	$\omega_R = \frac{1}{2}\omega_{ce} + \frac{1}{2}\sqrt{\omega_{ce}^2 + 4\omega_{pe}^2}$	$\omega_{ce} = \frac{eB_0}{m_e}$
L	$\omega_L = -\frac{1}{2}\omega_{ce} + \frac{1}{2}\sqrt{\omega_{ce}^2 + 4\omega_{pe}^2}$	$\omega_{ci} = \frac{ZeB_0}{m_i}$
O	$\omega = \sqrt{\omega_{pe}^2 + \omega_{pi}^2}$	-
X	$\omega = \omega_R, \quad \omega = \omega_L$	$\omega_{lh} = \sqrt{\omega_{ce} \omega_{ci}}, \quad \omega_{uh} = \sqrt{\omega_{pe}^2 + \omega_{ce}^2}$

Table 1: Summary of cut-offs and resonances for all the principal waves. Note that ω_{lh} and ω_{uh} are so-called lower hybrid frequency and upper hybrid frequency, respectively.

Now, it is necessary to find dispersion relations for the two simplest cases, propagation along and perpendicular to the magnetic field. For the waves propagating along \mathbf{B}_0 $\alpha = 0$ and the dispersion relation 2.27 gets relatively simple form,

$$(\omega^2 - \omega_{pe}^2) \left[(\omega^2 - \omega_{pe}^2 - c^2 k^2)^2 - \left(\frac{\omega_{ce}}{\omega} \right)^2 (\omega^2 - c^2 k^2)^2 \right] = 0. \quad (2.28)$$

The equation 2.28 has three solutions. The first describes plasma oscillations at frequency $\omega = \omega_{pe}$. The second and third solutions give right-handed (R) and left-handed (L) circularly polarized waves,

$$N_R^2 = 1 - \frac{(\omega_{pe}/\omega)^2}{1 - \omega_{ce}/\omega}, \quad N_L^2 = 1 - \frac{(\omega_{pe}/\omega)^2}{1 + \omega_{ce}/\omega}. \quad (2.29)$$

In a similar manner, for the waves propagating perpendicular to \mathbf{B}_0 is $\alpha = \pi/2$ and the dispersion relation 2.27 has the following form,

$$(\omega^2 - \omega_{pe}^2 - c^2 k^2) [(\omega^2 - \omega_{pe}^2) (\omega^2 - \omega_{pe}^2 - c^2 k^2) - \omega_{ce}^2 (\omega^2 - c^2 k^2)] = 0. \quad (2.30)$$

The equation 2.30 has two solutions, which give ordinary (O) and extraordinary (X) waves,

$$N_O^2 = 1 - \left(\frac{\omega_{pe}}{\omega} \right)^2, \quad N_X^2 = 1 - \left(\frac{\omega_{pe}}{\omega} \right)^2 \frac{1 - (\omega_{pe}/\omega)^2}{1 - (\omega_{pe}/\omega)^2 - (\omega_{ce}/\omega)^2}. \quad (2.31)$$

The ordinary wave corresponds to a linearly polarized wave with electric field lying along the magnetic field direction, so that the motion remains unaffected. The extraordinary wave has the electric fields that are perpendicular to magnetic field, but with components both

perpendicular and parallel to the wave vector. Note that all of the cut-offs and resonances of waves propagating through magnetized plasmas (including ions) are listed in the table 1.

2.4 Ponderomotive force

The ponderomotive force is one of the most important quantities in the interaction of high intensity laser pulses with plasma. It represents the gradient of the laser intensity that pushes charged particles in plasma into the regions of a lower field amplitude and it consequently leads to a wide range of non-linear phenomena that make the plasma inherently unstable. The ponderomotive force is involved e. g. in filamentation and self-focusing of laser beam, in the formation of cavities and solitons in the plasma profile or various parametric instabilities.

Note that since the mass of the ions is much higher than the electron mass, the ponderomotive force acting on ions is in most cases negligible. However, the ponderomotive force exerted on the electrons may be consequently transmitted to the ions by the electric field which is created due to the charge separation in plasma.

In the following two subsections, one can find the derivation of the ponderomotive force for the non-relativistic as well as the relativistic case. The derivation of the non-relativistic formula for ponderomotive force is easy to understand and clearly depicts its main characteristics that are valid even for the relativistic case. However, one has to be aware that the non-relativistic approximation breaks down if the laser intensity exceeds the values around 10^{18} W/cm². This may be the case of short or tightly focused high-power laser beams. For this reason, the relativistic case is briefly discussed as well in the second subsection.

2.4.1 Non-relativistic case

The ponderomotive force can be derived from the motion of single particle in prescribed electromagnetic field. Thus one may exploit the Newton's equation of motion with the Lorentz force (2.8). As the laser propagates through plasma, one may expect the oscillation of charged particles in a high-frequency electromagnetic field. For the mathematical description, one may exploit the so-called oscillation-center approximation in this case. It consist of splitting the radius vector \mathbf{r} and velocity \mathbf{v} of an arbitrary charged particle into two parts,

$$\mathbf{r} = \mathbf{r}_0 + \delta\mathbf{r}, \quad \mathbf{v} = \mathbf{v}_0 + \delta\mathbf{v}, \quad (2.32)$$

where the index 0 denotes the quantities at the center of oscillation and $\delta\mathbf{x} = \mathbf{x} - \mathbf{x}_0$ stands for the oscillating vector. Note that in the case of non-relativistic derivation, the quantity \mathbf{v}_0 in 2.32 is identically equal to zero vector. Next, one may exploit the Taylor series to expand both, the electric field $\mathbf{E}(\mathbf{r}, t)$ and magnetic field $\mathbf{B}(\mathbf{r}, t)$ around the oscillation center \mathbf{r}_0 ,

$$\mathbf{E}(\mathbf{r}_0 + \delta\mathbf{r}, t) \cong \mathbf{E}(\mathbf{r}_0, t) + (\delta\mathbf{r} \cdot \nabla) \mathbf{E}(\mathbf{r}_0, t), \quad (2.33)$$

$$\mathbf{B}(\mathbf{r}_0 + \delta\mathbf{r}, t) \cong \mathbf{B}(\mathbf{r}_0, t) + (\delta\mathbf{r} \cdot \nabla) \mathbf{B}(\mathbf{r}_0, t). \quad (2.34)$$

Note that taking only the zeroth and first-order terms of the fields is sufficiently accurate approximation for the description of non-relativistic ponderomotive force. By substituting 2.32, 2.33 and 2.34 into 2.8 and collecting the terms of the same order, one obtains the following two equations,

$$m_s \frac{d^2\delta\mathbf{r}}{dt^2} = q_s \mathbf{E}(\mathbf{r}_0, t), \quad (2.35)$$

$$m_s \frac{d^2\mathbf{r}_0}{dt^2} = q_s [(\delta\mathbf{r} \cdot \nabla) \mathbf{E}(\mathbf{r}_0, t) + \delta\mathbf{v} \times \mathbf{B}(\mathbf{r}_0, t)]. \quad (2.36)$$

To solve equations 2.35 and 2.36, assume further the laser fields in the form of standing monochromatic wave,

$$\mathbf{E}(\mathbf{r}_0, t) = \mathbf{E}_0(\mathbf{r}_0) \cos \omega t, \quad \mathbf{B}(\mathbf{r}_0, t) = -\frac{1}{\omega} \nabla \times \mathbf{E}_0(\mathbf{r}_0) \sin \omega t. \quad (2.37)$$

Note that the magnetic field in 2.37 has been obtained by the integration of Faraday's law (1.3). Taking into account the previous considerations, the solution of 2.35 yields the oscillating quantities,

$$\delta\mathbf{r} = -\frac{q_s}{m_s \omega^2} \mathbf{E}_0(\mathbf{r}_0) \cos \omega t, \quad \delta\mathbf{v} = \frac{q_s}{m_s \omega} \mathbf{E}_0(\mathbf{r}_0) \sin \omega t. \quad (2.38)$$

Since the integration constants can be considered as a slowly varying time functions, they have been included in \mathbf{r}_0 . By inserting 2.38 into 2.36 one gets the following formula,

$$m_s \frac{d^2\mathbf{r}_0}{dt^2} = -\frac{q_s^2}{m_s \omega^2} [(\mathbf{E}_0(\mathbf{r}_0) \cdot \nabla) \mathbf{E}_0(\mathbf{r}_0) \cos^2 \omega t + \mathbf{E}_0(\mathbf{r}_0) \times (\nabla \times \mathbf{E}_0(\mathbf{r}_0)) \sin^2 \omega t]. \quad (2.39)$$

To get the quasi-stationary ponderomotive force, one shall compute the time average values over the laser period $T = 2\pi/\omega$. Thus by performing the time average of 2.39 (note that $\langle \sin^2 \omega t \rangle_T = \langle \cos^2 \omega t \rangle_T = 1/2$) one gets

$$m_s \left\langle \frac{d^2\mathbf{r}_0}{dt^2} \right\rangle_T = -\frac{q_s^2}{2m_s \omega^2} [(\mathbf{E}_0(\mathbf{r}_0) \cdot \nabla) \mathbf{E}_0(\mathbf{r}_0) + \mathbf{E}_0(\mathbf{r}_0) \times (\nabla \times \mathbf{E}_0(\mathbf{r}_0))]. \quad (2.40)$$

The first term on the right-hand side of 2.40 contributes to the transverse component of the ponderomotive force, whilst its longitudinal component originates from the second term. Utilizing standard identities of vector calculus, one finally gets the resulting quasi-stationary ponderomotive force $\mathbf{F}_p(\mathbf{r})$ in the non-relativistic case,

$$\mathbf{F}_p = -\nabla \Phi_p, \quad \Phi_p = \frac{q_s^2}{4m_s \omega^2} E_0^2, \quad (2.41)$$

where $\Phi_p(\mathbf{r})$ is the corresponding ponderomotive potential, which may be interpreted as a cycle-averaged oscillation energy. Sometimes, it may be yet useful to have the expression for the ponderomotive force per unit volume $\mathbf{f}_p(\mathbf{r})$. To obtain it, one has to multiply the formula 2.40 by the particle density. In the case of the electron fluid and normal laser light incidence on plasma, one gets the following expression,

$$\mathbf{f}_p = -\frac{\varepsilon_0 \omega_{pe}^2}{4 \omega^2} \nabla E_0^2. \quad (2.42)$$

2.4.2 Relativistic case

The non-relativistic case is based on neglecting the term $\mathbf{v} \times \mathbf{B}$ in the Newton's equation of motion (2.8). However, this approximation is not valid for particles moving with velocities close to the velocity of light c . The derivation of the relativistic ponderomotive force presented in this subsection follows [source].

A system containing a charged particle in an arbitrary electromagnetic field can be rigorously described using Lagrangian mechanics. The relativistic Lagrangian $L(\mathbf{r}, \mathbf{v}, t)$ for this case is given by the following expression,

$$L = -\frac{m_s c^2}{\gamma} - q_s (\Phi - \mathbf{v} \cdot \mathbf{A}), \quad \gamma = \left(1 - \frac{v^2}{c^2}\right)^{-\frac{1}{2}}. \quad (2.43)$$

For the traveling monochromatic wave, the Lagrangian $L(\mathbf{r}, \mathbf{v}, t)$ in 2.43 can be transformed to $L(\varphi)$ using the wave phase $\varphi = \mathbf{k} \cdot \mathbf{r} - \omega t$. The reason of doing this is that the transformed Lagrangian can be used to obtain the average over the wave period of motion,

$$\mathcal{L}_0(\varphi) = \frac{1}{2\pi} \int_{\varphi}^{\varphi+2\pi} \mathcal{L}(\varphi') d\varphi', \quad \mathcal{L}(\varphi) = L(\varphi) \left(\frac{d\varphi}{dt}\right)^{-1}. \quad (2.44)$$

Note that the Langrangian 2.44 depends only on the quantities at the center of oscillation \mathbf{r}_0 and \mathbf{v}_0 defined through φ . Then the motion of the oscillation center is governed by the Lagrange equations,

$$\frac{d}{dt} \left(\frac{\partial \mathcal{L}_0}{\partial \mathbf{v}_0} \right) - \frac{\partial \mathcal{L}_0}{\partial \mathbf{r}_0} = 0, \quad \mathcal{L}_0(\varphi) = \mathcal{L}_0(\varphi) \left(\frac{d\varphi}{dt}\right). \quad (2.45)$$

The complete proof of assertions above can be found in [source].

The relativistic ponderomotive force in the oscillation center system can be easily found from the Lagrange equations 2.45,

$$\mathbf{F}_p \equiv \frac{d}{dt} \left(\frac{\partial \mathcal{L}_0}{\partial \mathbf{v}_0} \right) = -c^2 \nabla m_{\text{eff}}, \quad (2.46)$$

where the so-called effective mass m_{eff} is the space and time dependent quantity that has been introduced as follows,

$$m_{\text{eff}} = -\mathcal{L}_0 \frac{\gamma_0}{c^2} \left(\frac{d\varphi}{dt} \right), \quad \gamma_0 = \left(1 - \frac{v_0^2}{c^2} \right)^{-\frac{1}{2}}. \quad (2.47)$$

Note that the assertion 2.47 holds for any electromagnetic field in vacuum in which it is possible to define the oscillation center. For ordinary conditions, the effective mass m_{eff} can be rewritten as

$$m_{\text{eff}} = m_s \sqrt{1 + \frac{q_s A^2}{\alpha m_s^2 c^2}} \quad (2.48)$$

with $\alpha = 1$ for circular and $\alpha = 2$ for linear polarization of the electromagnetic wave.

2.5 Self-induced transparency (SIT)

As already mentioned in the section 2.3, the electromagnetic wave with frequency ω cannot propagate through plasma with densities greater than the critical density $n_c(\omega)$. However, in the case of intense laser beam, one has to perform a relativistic generalization of the dispersion relation, thus the corresponding cut-off frequency is given by the following formula,

$$\omega = \sqrt{\frac{\omega_{pe}^2}{\gamma} + \omega_{pi}^2}, \quad \gamma = \left(1 - \frac{v^2}{c^2} \right)^{-\frac{1}{2}}. \quad (2.49)$$

Note that one assumes only relativistic electrons in the equation 2.49 (relativistic ions would require laser intensities $I > 10^{24}$ W/cm²). One may immediately see that in the relativistic case, the laser beam actually propagates up to densities $n'_c(\omega) = n_c(\omega) \gamma > n_c(\omega)$. This increase of the effective critical density is called relativistic self-induced transparency (SIT) [source].

Note that in the case of real laser pulse, the ability to penetrate into the overdense plasma depends on the local amplitude. Therefore, there are logically some parts of laser beam that may propagate, while the others cannot. Consequently, both the reflected and transmitted laser intensity profiles reveal temporal chopping that leads to the significant modifications of the pulse shape.

Furthermore, one has to be aware that the plasma does not remain homogeneous during the laser-plasma interaction. As mentioned in the section 2.4, the ponderomotive force pushes electrons in plasma into the regions of a lower field amplitude creating a charge separation layer. Consequently, the plasma density rapidly increases in these regions. Therefore, it is necessary to resolve the propagation of the electromagnetic wave self-consistently with the modification of plasma density profile.

Note that the electromagnetic wave propagating in a relativistically transparent target may be a subject of strong instabilities that lead to an additional plasma heating. Thus this way, the energy of electromagnetic wave may be also absorbed [source]. Furthermore, in the SIT regime, the acceleration of charged particles due to the ponderomotive force may take place in the whole volume of the target.

At the end of this section, an approach to SIT based on a steady state solutions that follows [source] is presented. Consider a laser pulse to be a monochromatic plane wave at normal incidence and with circular polarization. Then the thresholds for SIT in the case of two limit cases, a semi-infinite plasma and an ultrathin plasma slab of thickness l , are given by following two formulas,

$$a_0 \cong \frac{3^{3/2}}{2^3} \left(\frac{n_0}{n_c} \right)^2 \quad \text{for } n = n_0 H(x), \quad (2.50)$$

$$a_0 \cong \frac{\pi l}{\lambda} \frac{n_0}{n_c} \quad \text{for } n = n_0 l \delta(x), \quad (2.51)$$

where $H(x)$ stands for a Heaviside step function and $\delta(x)$ is Dirac delta function. The threshold values are expressed in terms of laser dimensionless potential $a_0 = eE_0/m_e\omega c$. If the conditions 2.50 and 2.51 are fulfilled, laser beam penetrates plasma as a non-linear wave.

Note that the model presented above is based on several simplifications (e.g. the pulse profile or electron oscillations and heating are not included). In general case, the SIT dynamics is obviously much more complicated.

2.6 Laser absorption and electron heating mechanisms

Absorption of laser energy during the laser-plasma interaction is an important research topic. The energy of laser pulses can be absorbed in plasma by various different mechanisms depending on the laser intensity. For the laser intensities considered within this work (above 10^{16} W/cm²), the plasma is predominantly heated by collisionless absorption mechanisms. These mechanisms are generally characterized by the fact that the energy is transferred to a relatively small part of so-called hot electrons. In the following three subsections, the main mechanisms of collisionless plasma heating are briefly described.

2.6.1 Resonance absorption

The energy of laser beam may be absorbed by resonance absorption in the plasma. It is a linear process in which an incident laser wave is partially absorbed by conversion into an electron wave at the critical density of plasma $n_c(\omega)$.

Resonance absorption takes place when a linearly p-polarized laser pulse is obliquely incident on a plasma with an inhomogeneous density profile. A component of the electric

laser field perpendicular to the target surface then resonantly excites an electron plasma wave also along the plasma density gradient, thus a part of the laser wave energy is transferred into the electrostatic energy of the electron plasma wave. This wave propagates into the underdense plasma and is damped either by collision or collisionless absorption mechanisms. Consequently, energy is further converted into the thermal energy which heats the plasma and may possibly produce hot electrons.

Particularly, resonance absorption is the main absorption process for the laser beams of higher intensities and longer wavelengths. The efficiency of the resonance absorption may also be higher in plasma with high temperature, low critical density, or short scale length of the density profile.

2.6.2 Brunel's vaccum heating

Similarly as for the resonance absorption, Brunel's vaccum heating takes place when a linearly p-polarized laser pulse is obliquely incident on a plasma. In this case, however, the incident angle must be relatively large. Moreover, the plasma density profile has to be steep, so the amplitude of the oscillating electrons driven by the electric laser field is larger than the density scale length. Consequently, the energy of laser pulse carried by electrons is transferred into mechanical or heat energy in the overdense plasma region.

The energy absorbed via Brunel's vacuum heating is carried by hot electrons in the bunches ejected once per laser period. To give a physical picture, in the first half of laser cycle, the electrons are pushed inside the plasma gaining only a small amount of energies because the electric laser field is shielded. On the other hand, in the second half of laser cycle, the electrons gain very high energies while they are ejected into vacuum.

The trajectory of charged particles is strongly influenced by the time of their expulsion. Furthermore, a self-consistent electric field may be generated if a large amount of charged particles is ejected at the same time. The majority of the charged particles, however, returns into the plasma and propagates behind the skin layer where the laser electric field is screened so they can travel virtually unhindered into the target. Note that since the charged particles are accelerated by different phases of the laser field, the distribution of such particles can be in most cases considered as a Maxwellian [source].

2.6.3 Relativistic $\mathbf{J} \times \mathbf{B}$ heating

For the relativistic laser beams, the high-frequency $\mathbf{v} \times \mathbf{B}$ component of the Lorentz force becomes important and may contribute to plasma heating. Similarly to the Brunel's vacuum heating, discussed in the previous subsection, $\mathbf{J} \times \mathbf{B}$ heating requires very steep plasma density gradients. On the contrary, this heating scenario works for any polarization apart from circular and is most efficient for the laser pulses normally incident onto the target surface, so there is no oscillating component of the electric field perpendicular to plasma.

In the case of $\mathbf{J} \times \mathbf{B}$ heating, the absorbed energy is carried by bunches of hot electrons

that are ejected twice per laser period. This fact may help to distinguish between the effects of Brunel's and $\mathbf{J} \times \mathbf{B}$ heating. Again, the ejected electrons are pushed back into the plasma by self-consistent electric field generated by charged particles without restoring forces behind the skin layer.

2.7 Mechanisms of laser-driven ion acceleration

Because of the relatively large ion mass, currently achievable laser intensities are not strong enough to accelerate protons or heavier ions directly to sufficiently high energies. However, ions typically respond on slowly varying electric fields in plasma arising from the strong charge separations induced by various phenomena that take place during the interaction of intense laser beam with matter.

As one may see later, ions can be either accelerated in the vicinity of the laser focal spot at the front side of the target as well as in the vicinity of the target-vacuum boundary at the rear side. In the last two subsections of this chapter, the two main mechanisms for ion acceleration in laser-plasma interactions are briefly described.

2.7.1 Radiation pressure acceleration (RPA)

Radiation pressure acceleration (RPA) stands for the mechanism in which the ions are accelerated from the target front side in the vicinity of the laser focal spot. The acceleration is driven by the ponderomotive force (see the section 2.4) which expels the electrons into the regions of a lower laser intensities and consequently generates a strong electrostatic fields as a result of charge separation. In the case of intense laser beams, the radiation pressure is strong enough to push an overdense target inwards whilst changing the shape of its surface and correspondingly the density profile. This process is commonly named hole boring.

For a plane, monochromatic wave at normal incidence onto a target at rest, the balance between the electrostatic pressure and the radiation pressure at the target surface can be expressed as follows,

$$\frac{1}{2}\varepsilon_0 E_{\text{es}}^2 = \frac{(1 + R - T)}{c} I, \quad (2.52)$$

where $\mathbf{E}_{\text{es}}(\mathbf{r}, t)$ is the electrostatic field generated by the charge separation, R and T are the reflection and transmission coefficients of the target, respectively, and I is the intensity of incident laser pulse.

A charge depletion layer is established at the front side of the target due to the radiation pressure of the laser beam. Ions in the depletion layer are accelerated by the electrostatic field $\mathbf{E}_{\text{es}}(\mathbf{r}, t)$, which amplitude can be obtained by solving the Poisson equation. The maximum

energy, that the ions may gain, is then estimated as follows [source],

$$\mathcal{E}_{max} = \frac{Zm_e c^2 a_0^2}{m_i \gamma}, \quad \gamma = \sqrt{1 + \frac{a_0^2}{2}}. \quad (2.53)$$

The RPA regime starts to dominate for a laser beams with peak intensity higher than 10^{21} W/cm². RPA could be more efficient for circularly polarized laser beams normally incident onto a target, because of their ability to suppress the effects of electron heating mechanisms mentioned in the previous section. Note that the RPA mechanism typically produce an ion beam of a large divergence because the critical density interface where the charge separation occurs is curved by the shape of the laser beam.

2.7.2 Target normal sheath acceleration (TNSA)

The interaction of intense laser beam with matter typically produce a population of hot electrons that may pass through the target and propagate beyond its rear side. This leads to generation of a strong electrostatic potential which accelerates the ionized particles in the direction normal to the target rear surface. Therefore, this mechanism is commonly known as target normal sheath acceleration (TNSA). TNSA can be also observed on the target front, because hot electrons are also expelled by the laser pulse into the vacuum on this side of the target.

The approximation for TNSA mechanism can be provided either by the static or dynamic model of the sheath. In the following, a dynamic model based on a free isothermal expansion of electron-ion plasma into vacuum is briefly described.

To find a non-linear solution that corresponds to the isothermal rarefaction wave, one may exploit the hydrodynamic equations for an ion component,

$$\frac{\partial n_i}{\partial t} + \nabla \cdot (n_i \mathbf{u}_i) = 0, \quad (2.54)$$

$$\frac{\partial \mathbf{u}_i}{\partial t} + (\mathbf{u}_i \cdot \nabla) \mathbf{u}_i = \frac{Ze}{m_i} \mathbf{E}. \quad (2.55)$$

Assume that at time $t = 0$, the electron density satisfies the Boltzmann distribution and the ion density occupies a half space with an infinitely sharp boundary, thus

$$n_e = n_{e0} \exp\left(\frac{e\Phi}{k_B T_e}\right), \quad n_i = n_{i0} H(x). \quad (2.56)$$

Assume further that the plasma is locally neutral on the scale length larger than the Debye radius, therefore $n_e = Zn_i$. However, one shall be aware that the condition for the local neutrality does not imply that there is no electrostatic field. The electrostatic field may arise due to the sources coming from the regions where the condition for quasi-neutrality does

not hold. Therefore, the electric field $\mathbf{E}(\mathbf{r}, t)$ in the equation 2.55 may be replaced by the electrostatic field $\mathbf{E}_{es}(\mathbf{r}, t) = -\nabla\Phi(\mathbf{r}, t)$, which one can obtain by taking the gradient of the electron density 2.56. After replacing the electric field $\mathbf{E}(\mathbf{r}, t)$ in the equation 2.55 one gets

$$\frac{\partial \mathbf{u}_i}{\partial t} + (\mathbf{u}_i \cdot \nabla) \mathbf{u}_i = -\frac{c_s^2}{n_i} \nabla n_i, \quad c_s = \sqrt{\frac{Zk_B T_e}{m_i}}, \quad (2.57)$$

where $c_s(\mathbf{r}, t)$ is the ion-acoustic velocity. By performing the Fourier transforms of the equations 2.54 and 2.57, one easily obtains the dispersion relation of the ion-acoustic waves. However, the system has also a non-linear self-similar solution which describes the rarefaction wave. Thus, define a self-similar variable in 1D geometry as $\xi = x/t$. The ion fluid density and velocity then become $n_i(x, t) = N(\xi)$ and $u_i(x, t) = V(\xi)$, respectively. After transformation, the system of equations 2.54 and 2.57 yields

$$\frac{1}{N} \frac{dN}{d\xi} = -\frac{V - \xi}{c_s}, \quad (2.58)$$

$$\frac{dV}{d\xi} = -\frac{1}{N} \frac{dN}{d\xi} (V - \xi). \quad (2.59)$$

Now, the set of equations 2.58, 2.59 can be solved easily. The solution in the original coordinates can be found below,

$$n_i = n_{i0} \exp\left(-\frac{x}{c_s t} - 1\right), \quad u_i = c_s + \frac{x}{t}. \quad (2.60)$$

Note that the solution 2.60 is valid only for $x > -c_s t$ where $u_i > 0$. The condition $x = -c_s t$ describes the rarefaction front propagating backwards into the target at the speed c_s . Finally, by plugging the solution 2.60 into the equation 2.55, one may find the expression for the electric field at the ion front $x = -c_s t$,

$$E_x = \frac{2E_0}{\omega_{pi} t}, \quad E_0 = c_s \sqrt{\frac{n_i m_i}{\varepsilon_0}}. \quad (2.61)$$

The apparent drawback of formula 2.61 is that it has a singularity at time $t = 0$. However, one may find a simple expression for the electric field at $t = 0$ by integration of the Poisson's equation from $x = 0$ to $x = +\infty$,

$$E_x = \sqrt{\frac{2}{e}} E_0. \quad (2.62)$$

A very precise interpolation of the electric field at the ion front, which is valid for any time,

has been already found [source],

$$E_x \cong \frac{2E_0}{\sqrt{2e + \omega_{pi}^2 t^2}}. \quad (2.63)$$

As a consequence of formula 2.63, one may find relatively accurate prediction of the corresponding ion front velocity by solving the equation of motion 2.55 with the electric field 2.63,

$$u_i \cong 2c_s \ln \left[\frac{\omega_{pi} t}{\sqrt{2e}} + \left(\frac{\omega_{pi}^2 t^2}{2e} + 1 \right)^{\frac{1}{2}} \right]. \quad (2.64)$$

The maximum ion energy is then proportional to the temperature of hot electrons, which scales with the ponderomotive potential ($\sim \sqrt{I\lambda^2}$) [source].

The next drawback of the model is that the derived formula for maximum velocity of ions 2.64 diverges logarithmically with time, therefore the system accelerates the ions infinitely. This result comes from the isothermal assumption. Nevertheless, one might overcome this drawback by assuming the finite thickness of plasma or by introducing a maximum acceleration time constant at which the ion acceleration stops [source].

Chapter 3

Particle-in-cell (PIC) method

This chapter is devoted to numerical simulations, particularly to the particle-in-cell (PIC) method, which represents one of the most popular numerical algorithms in plasma physics. The mathematical background of this method, description of the individual steps of the computational cycle as well as the stability conditions are all discussed. The last section provides a brief overview of the particle-in-cell code EPOCH, which has been used for simulations within this work.

3.1 Mathematical derivation

Laser-plasma interaction involves a collective behavior of particles and electromagnetic fields which is in general complex and strongly non-linear problem to solve. The investigation of such systems cannot be usually carried out only through the theoretical and experimental work. Since a large amount of simultaneous processes with many degrees of freedom may be present there, analytical modeling seems to be impractical. On the other hand, many of the significant details of laser-plasma interaction may be extremely difficult or even impossible to obtain experimentally. Hence, other tools and techniques are required for the further progress in this field of research [5].

Numerical simulations help researchers to develop models covering a wide range of physical scenarios as well as to investigate their properties. With the advent of powerful computational systems, numerical simulations now play an important role as an essential tool in developing theoretical models and understanding experimental results in various fields of modern science [6]. These so-called computer experiments are often faster and much cheaper than a single real experiment in laboratory [7]. In addition, one numerical code can solve a broad range of tasks only by modification of its initial and boundary conditions.

Nowadays, it is clear that detailed understanding of the physical mechanisms in the laser-plasma interaction can be achieved only through the combination of theory, experiment and simulation. Development of parallel algorithms that are able to provide sufficiently exact

solutions in reasonable time, however, belongs to the most challenging fields of modern science.

The PIC method refers to a technique that has been used to solve a certain class of partial differential equations. The method has been proposed in the mid-fifties and it has early gained a great popularity in the field of plasma physics [source]. It is based on the kinetic approach, thus the evolution of the system is described in principle via the motion of the charged particles.

However, real systems are often extremely large in terms of the number of particles they contain. In order to make simulations computationally tractable, so-called macro-particles are used. The macro-particle is a finite-size computational particle representing a group of physical particles that are near each other in the phase space. Notice that it is allowed to rescale the number of particles, because the Lorentz force depends only on the charge to mass ratio, which is invariant to this transformation. Thus, the macro-particle will follow the same trajectory as the corresponding real particles would [8].

Although this approach significantly reduces the number of computational particles in simulation, the binary interactions for every pair in the system cannot be taken into account. The cost would scale quadratically as the number of particles increases and that makes the computational effort unmanageable in the case of larger systems. Fortunately, many of the phenomena occur in high-temperature plasmas where the collective behavior dominates and the collisional effects are very weak (see 2.6), thus one can neglect them. Otherwise, one has to exploit other techniques to estimate the collisional effects [9].

In the collisionless plasma, the phase space particle distribution function $f_s(\mathbf{r}, \mathbf{v}, t)$ for a given species s is governed by the Vlasov equation (2.9). The mathematical formulation of the PIC method is obtained by assuming that the distribution function $f_s(\mathbf{r}, \mathbf{v}, t)$ is given by the sum of distribution functions for macro-particles $f_{p,s}(\mathbf{r}, \mathbf{v}, t)$,

$$f_s = \sum_p f_{p,s}. \quad (3.1)$$

Index p denotes hereafter the quantities attributable to macro-particles. The distribution function for each macro-particle is further assumed to be

$$f_{p,s}(\mathbf{r}, \mathbf{v}, t) = w_p S_r(\mathbf{r} - \mathbf{r}_p(t)) S_v(\mathbf{v} - \mathbf{v}_p(t)), \quad (3.2)$$

where w_p is a weight depending on the number of physical particles represented by each macro-particle, and $S_r(\mathbf{r} - \mathbf{r}_p(t))$, $S_v(\mathbf{v} - \mathbf{v}_p(t))$ are the so-called shape functions for the spatial and velocity coordinate, respectively.

The shape functions cannot be chosen arbitrarily. They have to fulfill several special properties. Let S_ξ be the shape function of the phase space coordinate ξ . Then:

1. The support of the shape function is compact, $\exists R > 0$, $\text{supp } S_\xi \subset (-R, R)$.



Figure 1: Computational cycle of the particle-in-cell method

2. Integral of the shape function is unitary, $\int_{-\infty}^{+\infty} S_\xi(\xi) d\xi = 1$.
3. The shape function is symmetrical, $S_\xi(\xi) = S_\xi(-\xi)$.

While these restrictive conditions still offer a wide range of options, the standard PIC method is essentially determined by the choice of the shape function in the velocity coordinate as a Dirac delta function and in the spatial coordinate as a m-th order b-spline basis function b_m . Note that the choice of the shape functions has strong impact on the stability and accuracy of the simulation. Higher-order basis functions result in less numerical noise and reduce non-physical phenomena in simulations, obviously at the cost of increased computational time.

Substituting the discretization 3.1 into the Vlasov equation 2.9 and taking into account the properties of shape functions mentioned above, one obtains the set of equations of motion for macro-particle p as the first moments,

$$\frac{d\mathbf{r}_p}{dt} = \mathbf{v}_p, \quad \frac{d\mathbf{p}_p}{dt} = \mathbf{F}_p, \quad (3.3)$$

where \mathbf{p}_p is particle momentum and $\mathbf{F}_p(t)$ represents a spatial average of the force acting on the macro-particle,

$$\mathbf{F}_p = q_s (\mathbf{E}_p + \mathbf{v}_p \times \mathbf{B}_p). \quad (3.4)$$

The fields at the macro-particle position $\mathbf{E}_p(t)$ and $\mathbf{B}_p(t)$ in 3.4 are given by the spatial shape function, which implies some form of interpolation. This will be closer discussed in the fourth section of this chapter.

The PIC method combines Lagrangian and Eulerian frame of reference. It means that

the macro-particles are tracked in continuous phase space, whereas the electromagnetic fields are calculated only on stationary grid points. Therefore, it is necessary to perform the discretization of the spatial coordinates $\mathbf{r} \rightarrow \mathbf{r}_{ijk}$ where $(i, j, k) \in \mathbb{Z}^3$ are grid indices. It is also necessary to perform discretization of the temporal coordinate $t \rightarrow t^n$, where $n \in \mathbb{N}$ is the time level index. The algorithm will be outlined for a three-dimensional equidistant rectangular grid, thus $\mathbf{r}_{ijk} = (i\Delta x, j\Delta y, k\Delta z)$, where $\Delta x, \Delta y, \Delta z$ are the spatial steps in each direction and $t^n = n\Delta t$, where Δt is the time step. Each quantity $A(\mathbf{r}_{ijk}, t^n)$ will be hereafter denoted as A_{ijk}^n .

The computational cycle of the PIC method is shown in Figure 1. Individual steps are closer described in several following sections. The influence of the choice of the time and spatial step on the stability and accuracy of the PIC method will be demonstrated as well.

3.2 Particle pusher

As one could already see from 3.3, the motion of macro-particles in simulation is governed by the Newton equations with spatially averaged Lorentz force. Since the particles can reach velocities near the velocity of light, it is necessary to perform relativistic generalization,

$$\mathbf{u}_p = \gamma \mathbf{v}_p, \quad \gamma = \sqrt{1 + \left(\frac{\mathbf{u}_p}{c}\right)^2}. \quad (3.5)$$

Assume that the electric and magnetic fields are interpolated from the grid points to the particles at the time level t^n . Then the equations of motion to be integrated are

$$\frac{d\mathbf{r}_p}{dt} = \frac{\mathbf{u}_p}{\gamma}, \quad \frac{d\mathbf{u}_p}{dt} = \frac{q_s}{m_s} \left(\mathbf{E}_p + \frac{\mathbf{u}_p}{\gamma} \times \mathbf{B}_p \right). \quad (3.6)$$

To discretize the equations of motion 3.6, a time-centered leap-frog scheme is used. One obtains

$$\frac{\mathbf{r}_p^{n+1} - \mathbf{r}_p^n}{\Delta t} = \frac{\mathbf{u}_p^{n+1/2}}{\gamma^{n+1/2}}, \quad (3.7)$$

$$\frac{\mathbf{u}_p^{n+1/2} - \mathbf{u}_p^{n-1/2}}{\Delta t} = \frac{q_s}{m_s} \left(\mathbf{E}_p^n + \frac{\mathbf{u}_p^{n+1/2} + \mathbf{u}_p^{n-1/2}}{2\gamma^n} \times \mathbf{B}_p^n \right). \quad (3.8)$$

Although these equations appear to be very simple, the solution is one of the most time-consuming parts of the simulation, because they must be solved for every single macro-particle at each time step. Standard approach for particle pushing in plasma simulation PIC codes involves Boris method, which completely separates the effect of electric and magnetic

fields [10]. Substitute

$$\mathbf{u}_p^{n-1/2} = \mathbf{u}_p^- - \frac{q_s \mathbf{E}_p^n}{m_s} \frac{\Delta t}{2}, \quad \mathbf{u}_p^{n+1/2} = \mathbf{u}_p^+ + \frac{q_s \mathbf{E}_p^n}{m_s} \frac{\Delta t}{2} \quad (3.9)$$

into the equation 3.8, then the electric field cancels entirely,

$$\frac{\mathbf{u}_p^+ - \mathbf{u}_p^-}{\Delta t} = \frac{q_s}{2\gamma^n m_s} (\mathbf{u}_p^+ + \mathbf{u}_p^-) \times \mathbf{B}_p^n. \quad (3.10)$$

The equation 3.10 describes a rotation of the vector \mathbf{u}_p^- to \mathbf{u}_p^+ in one simulation time step Δt . The angle θ between the vector \mathbf{u}_p^- and \mathbf{u}_p^+ is expected to be $\theta = \omega_c \Delta t$.

To implement the Boris method, first add half the electric impulse \mathbf{E}_p^n to $\mathbf{u}_p^{n-1/2}$, then perform the full rotation by the angle θ , and finally, add another half the electric impulse \mathbf{E}_p^n . From the basic geometry Boris derived following steps to obtain $\mathbf{u}_p^{n+1/2}$. From the first of the equations 3.9, express the vector \mathbf{u}_p^- ,

$$\mathbf{u}_p^- = \mathbf{u}_p^{n-1/2} + \frac{q_s \mathbf{E}_p^n}{m_s} \frac{\Delta t}{2} \quad (3.11)$$

and construct an auxiliary vector \mathbf{u}_p' , which is simultaneously perpendicular to $(\mathbf{u}_p^+ - \mathbf{u}_p^-)$ and to \mathbf{B}_p^n ,

$$\mathbf{u}_p' = \mathbf{u}_p^- + \mathbf{u}_p^- \times \mathbf{t}, \quad \mathbf{t} = \frac{q_s \mathbf{B}_p^n}{\gamma^n m_s} \frac{\Delta t}{2}. \quad (3.12)$$

The vector \mathbf{t} has to be logically parallel to \mathbf{B}_p^n with the length of $\tan(\theta/2) \approx \theta/2$ for small angles. Next, exploit the fact that the vector $(\mathbf{u}_p' \times \mathbf{B}_p^n)$ is parallel to $(\mathbf{u}_p^+ - \mathbf{u}_p^-)$ and express the vector \mathbf{u}_p^+ ,

$$\mathbf{u}_p^+ = \mathbf{u}_p^- + \mathbf{u}_p' \times \mathbf{s}, \quad \mathbf{s} = \frac{2\mathbf{t}}{1+t^2}. \quad (3.13)$$

Here the vector \mathbf{s} is parallel to \mathbf{B}_p^n and its length has to fulfill the condition $\|\mathbf{u}_p^+\| = \|\mathbf{u}_p^-\|$. The transition from \mathbf{u}_p^- to \mathbf{u}_p^+ can be written more clearly using the matrix,

$$\mathbf{u}_p^+ = \mathbb{M} \mathbf{u}_p^-, \quad (3.14)$$

where

$$\mathbb{M} = \begin{pmatrix} 1 - s_2 t_2 - s_3 t_3 & s_2 t_1 + s_3 & s_3 t_1 - s_2 \\ s_1 t_2 - s_3 & 1 - s_1 t_1 - s_3 t_3 & s_3 t_2 + s_1 \\ s_1 t_3 + s_2 & s_2 t_3 - s_1 & 1 - s_1 t_1 - s_2 t_2 \end{pmatrix}. \quad (3.15)$$

Finally, substitute the vector \mathbf{u}_p^+ into the second from the equations 3.9,

$$\mathbf{u}_p^{n+1/2} = \mathbf{u}_p^+ + \frac{q_s \mathbf{E}_p^n}{m_s} \frac{\Delta t}{2}. \quad (3.16)$$

The position of macro-particle is then advanced according to

$$\mathbf{r}_p^{n+1} = \mathbf{r}_p^n + \frac{\mathbf{u}_p^{n+1/2}}{\gamma^{n+1/2}} \Delta t, \quad \gamma^{n+1/2} = \sqrt{1 + \left(\frac{\mathbf{u}_p^{n+1/2}}{c} \right)^2}. \quad (3.17)$$

3.3 Field solver

As already mentioned, the behavior of the time varying electromagnetic field in free space is governed by the microscopic variant of Maxwell equations (1.1 - 1.4). A typical numerical technique to resolve the Maxwell's equations with respect to time is finite-difference time-domain method (FDTD), because it is probably the simplest technique in terms of the implementation.

The vector components of the fields \mathbf{E}_{ijk}^n and \mathbf{B}_{ijk}^n are spatially staggered about rectangular cells of the computational grid,

$$\mathbf{E}_{ijk}^n \rightarrow \left[(E_x)_{i, j+1/2, k+1/2}^n, (E_y)_{i+1/2, j, k+1/2}^n, (E_z)_{i+1/2, j+1/2, k}^n \right], \quad (3.18)$$

$$\mathbf{B}_{ijk}^n \rightarrow \left[(B_x)_{i+1/2, j, k}^n, (B_y)_{i, j+1/2, k}^n, (B_z)_{i, j, k+1/2}^n \right]. \quad (3.19)$$

This scheme, which has proven to be very robust, is now known as a Yee lattice [11]. The illustration of a standard Cartesian Yee cell used for FDTD is shown in Figure 2. Components of the current density \mathbf{J}_{ijk}^n are defined in the same way as the components of \mathbf{E}_{ijk}^n , charge density ρ_{ijk}^n is defined in the middle of the cell,

$$\mathbf{J}_{ijk}^n \rightarrow \left[(J_x)_{i, j+1/2, k+1/2}^n, (J_y)_{i+1/2, j, k+1/2}^n, (J_z)_{i+1/2, j+1/2, k}^n \right], \quad (3.20)$$

$$\rho_{ijk}^n \rightarrow \rho_{i+1/2, j+1/2, k+1/2}^n. \quad (3.21)$$

For marching in time, the leap-frog scheme is used. Therefore, discretized Maxwell's equations 1.1 - 1.4 have the following form,

$$\nabla^+ \cdot \mathbf{E}_{ijk}^n = \frac{\rho_{ijk}^n}{\epsilon_0}, \quad (3.22)$$

$$\nabla^- \cdot \mathbf{B}_{ijk}^{n+1/2} = 0, \quad (3.23)$$



Figure 2: Standard Cartesian Yee cell used for FDTD method

$$\frac{1}{c^2} \frac{\mathbf{E}_{ijk}^{n+1} - \mathbf{E}_{ijk}^n}{\Delta t} = \nabla^+ \times \mathbf{B}_{ijk}^{n+1/2} - \mu_0 \mathbf{J}_{ijk}^{n+1/2}, \quad (3.24)$$

$$\frac{\mathbf{B}_{ijk}^{n+1/2} - \mathbf{B}_{ijk}^{n-1/2}}{\Delta t} = -\nabla^- \times \mathbf{E}_{ijk}^n. \quad (3.25)$$

Notice that this scheme achieves second-order accuracy in both, space and time. Discrete operators (∇^+) and (∇^-) used in 3.22 - 3.25 act on a scalar field f_{ijk} as follows,

$$\nabla^+ f_{ijk} = \left(\frac{f_{i+1,j,k} - f_{i,j,k}}{\Delta x}, \frac{f_{i,j+1,k} - f_{i,j,k}}{\Delta y}, \frac{f_{i,j,k+1} - f_{i,j,k}}{\Delta z} \right), \quad (3.26)$$

$$\nabla^- f_{ijk} = \left(\frac{f_{i,j,k} - f_{i-1,j,k}}{\Delta x}, \frac{f_{i,j,k} - f_{i,j-1,k}}{\Delta y}, \frac{f_{i,j,k} - f_{i,j,k-1}}{\Delta z} \right). \quad (3.27)$$

These operators have the following properties,

$$\nabla^- \cdot \nabla^- \times = \nabla^+ \cdot \nabla^+ \times = 0, \quad \nabla^- \cdot \nabla^+ = \nabla^+ \cdot \nabla^- = \Delta^\pm. \quad (3.28)$$

Symbol Δ^\pm stands for the discrete Laplace operator in central differences,

$$\Delta^\pm f_{i,j,k} = \frac{f_{i-1,j,k} - 2f_{i,j,k} + f_{i+1,j,k}}{\Delta x^2} + \frac{f_{i,j-1,k} - 2f_{i,j,k} + f_{i,j+1,k}}{\Delta y^2} + \frac{f_{i,j,k-1} - 2f_{i,j,k} + f_{i,j,k+1}}{\Delta z^2}. \quad (3.29)$$

Before trying to find the solution of discretized Maxwell equations 3.22 - 3.25, one must realize that this system of equations is not independent. In the three-dimensional case, there

are eight first-order differential equations, but only six unknown vector components. Acting on the equations 3.24 and 3.25 by operators $(\nabla^- \cdot)$ and $(\nabla^+ \cdot)$, respectively, one obtains

$$\frac{\nabla^- \cdot \mathbf{B}_{ijk}^{n+1/2} - \nabla^- \cdot \mathbf{B}_{ijk}^{n-1/2}}{\Delta t} = 0, \quad (3.30)$$

$$\frac{\rho_{ijk}^{n+1} - \rho_{ijk}^n}{\Delta t} + \nabla^+ \cdot \mathbf{J}_{ijk}^{n+1/2} = 0. \quad (3.31)$$

It means that it is possible to solve only the equations 3.24 and 3.25, while the divergence equations 3.22, 3.23 can be considered as the initial conditions. Note that in this case, the continuity equation in the finite differences (3.31) has to be fulfilled.

3.4 Particle and field weighting

In order to solve the Maxwell's equations, as shown in the previous section of this chapter, one has to know the source terms produced by the motion of the charged particles. In other words, it is necessary to assign charge and current densities from the continuous macro-particle positions to the discrete grid points. This simulation step is usually referred to as particle weighting and it involves some form of interpolation.

According to the kinetic theory, charge density $\rho(\mathbf{x}, t)$ and current density $\mathbf{J}(\mathbf{x}, t)$ are given by the following integrals over the velocity space,

$$\rho(\mathbf{x}, t) = \sum_s q_s \int f_s(\mathbf{x}, \mathbf{v}, t) d\mathbf{v}, \quad \mathbf{J}(\mathbf{x}, t) = \sum_s q_s \int f_s(\mathbf{x}, \mathbf{v}, t) \mathbf{v} d\mathbf{v}. \quad (3.32)$$

After discretization of 3.32 using macro-particles and exploiting the properties of the shape functions, one gets immediately

$$\rho_{ijk}^n = \sum_p q_p S_r(\mathbf{r}_{ijk} - \mathbf{r}_p^n), \quad \mathbf{J}_{ijk}^n = \sum_p q_p \mathbf{v}_p^n S_r(\mathbf{r}_{ijk} - \mathbf{r}_p^n), \quad (3.33)$$

where $q_p = q_s w_p$. However, using the formulas 3.33 for charge and current deposition in PIC codes may violate the discrete continuity equation (3.31) and in turn cause errors in Gauss's law (3.22). In this case, one would have to solve the Poisson's equation for the correction of the electric field at every simulation time step or use a numerical scheme that satisfies the continuity equation exactly. These schemes are referred to as a charge conservation methods ([12], [13], [source]).

Similarly, to advance macro-particle positions, as shown in the second section of this chapter, one has to know the force acting on them. Hence, it is necessary to assign electric and magnetic fields that are calculated at the discrete grid points to the continuous macro-particle positions. This simulation step is usually referred to as field weighting.

By analogy to the particle weighting, one may exploit the shape functions to calculate the spatial averages of the electric and magnetic field components,

$$\mathbf{E}_p^n = \sum_{ijk} \mathbf{E}_{ijk}^n S_r(\mathbf{r}_{ijk} - \mathbf{r}_p^n), \quad \mathbf{B}_p^n = \sum_{ijk} \mathbf{B}_{ijk}^n S_r(\mathbf{r}_{ijk} - \mathbf{r}_p^n). \quad (3.34)$$

Note that it is recommended to use the same weighting for both, particles and fields, in order to eliminate a self-force and ensure the conservation of momentum [14].

3.5 Stability and accuracy

The stability and accuracy of the standard PIC method is directly dependent on the size of the spatial and temporal simulation steps. In order to find correct parameters, one has to know the absolute accuracy and corresponding stability conditions.

The effect of the spatial grid is the smoothing of the interaction forces and the coupling of plasma perturbations to perturbations at other wavelengths, called aliases. It may lead to non-physical instabilities and numerical heating. To avoid these effects, the spatial step should approximately resolve the Debye length (see 2.3). Thus, it is desirable to fulfill the following condition,

$$\Delta x, \Delta y, \Delta z \leq \lambda_D. \quad (3.35)$$

In the general electromagnetic case, the time step has to satisfy the Courant–Fridrichs–Levy (CFL) condition [5],

$$C = c^2 \Delta t^2 \left(\frac{1}{\Delta x^2} + \frac{1}{\Delta y^2} + \frac{1}{\Delta z^2} \right), \quad (3.36)$$

where the dimensionless number $C \leq 1$ is called the CFL number. This condition limits the range of motion of all objects in the simulation during one time step. It ensures that particles would not cross more than one cell in one simulation time step. When this condition is violated, the growth of non-physical effects can be very rapid. Another condition on the time step comes from the requirement to avoid aliasing, i.e. the time step must resolve all important frequencies according to the Nyquist-Shannon theorem $\omega \Delta t \leq 2$ ($\omega = \max(\omega_p, \omega_L)$).

The leap-frog scheme, used to solve the field equations and equations of motion, is second-order accurate in both, time and space. In addition, this scheme is explicit and time-reversible. An extensive study of PIC method can be found in [source].

3.6 Extendable PIC Open Collaboration (EPOCH)

The abbreviation EPOCH refers to an Extendable PIC Open Collaboration project [4]. EPOCH is a multi-dimensional, relativistic, electromagnetic code designed for plasma physics simulations based on the PIC method. The code, which has been developed at University

of Warwick, is written in FORTRAN and parallelized using MPI library. EPOCH is able to cover physical processes that may take place at ultra-high laser intensities, such as barrier suppression ionization, quantum electrodynamics emission and pair production.

The main computational features include dynamic load balancing option for making optimal use of all processors when run in parallel, allowing restart on an arbitrary number of processors. The setup of EPOCH is controlled through a customizable input deck. An input deck is a text file which can be used to set simulation parameters for EPOCH without necessity to edit or recompile the source code. Most aspects of the simulation can be controlled, such as the number of grid points in the simulation domain, the initial distribution of particles and the initial electromagnetic field configuration. In addition, EPOCH has been written to add more modern features and to structure the code in such a way that the future expansion of the code may be made as easily as possible. The entire core of the code uses SI units.

By default, EPOCH uses triangular particle shape functions with the peak located at the position of computational particle and a width of two cells, which provides relatively clean and fast solution. However, user can select higher order particle shape functions based on a spline interpolation by enabling compile-time option in the makefile.

The electromagnetic field solver uses FDTD scheme with second order of accuracy. The field components are spatially staggered on a standard Cartesian Yee cell. The solver is directly based on the scheme derived by Hartmut Ruhl [15]. The particle pusher is relativistic, Birdsall and Landon type [10] and uses Villasenor and Buneman current weighting [12].

EPOCH offers several types of boundary conditions for fields and particles, such as periodic, transmissive, reflecting and also Convolutional Perfectly Matched Layer (CPML) [source] boundary conditions. Laser beams can be attached to an arbitrary boundary via special boundary condition as well.

As a side project within this work, the code EPOCH has been instrumented to enable in situ diagnostics and visualization of the electromagnetic fields using ParaView Catalyst [source]. The increasing demands of the simulations need more data to be stored on a disk and analysed. However, the capabilities of computing environment which is responsible for transferring the data and communication have not grown up as rapid as the computational power. Dumping and processing of all the data calculated during the simulation would take too much time, so in practice this usually means that they are stored only at several time steps or at much coarser resolution than the original data. The rest is just discarded and the significant part of information may be potentially lost.

In situ visualization describes techniques where data can be visualized in real-time as it is generated during a simulation and without it being stored on a storage resource. By coupling the visualization and simulation, the data transfer bottleneck can be overcome. Furthermore, this approach allows scientists to monitor and interact with a running simulation, allowing for its parameters to be modified and allowing to immediately view the effects of these changes.

While a simulation is running, a user can see the size of the datasets that the simulation

produces. But none of this data is physically stored on a storage system. The computationally expensive operations are carried out using ParaView’s graphical interface. So, the user can select data structures and analyze them in the same way as in post-processing. But there is one difference, the simulation is in progress so a user can observe the data as it is being generated. With Catalyst, it is also possible to pause the simulation or specify a break-point at a selected time step. This can be helpful if a user expects some interesting behavior of investigated phenomena or for identifying regions where numerical instability arises. For the implementation details, see appendix B.

The main goal of this work has been to implement a solution that would enable to simulate tightly focused laser beams using simulation code EPOCH. This will be closer described in the following chapter.

Chapter 4

Tight-focusing of laser pulses

The investigation of laser-matter interactions also involves exploring of specific themes of the ultra-relativistic regime, which requires extremely high intensities of the external field. Tight-focusing and the plasma-based optics could potentially increase the laser pulse intensity by an order of magnitude in comparison with the conventional focusing approaches and thus the laser intensities of the order 10^{22} W/cm² could be reached by Petawatt laser systems. Such intensities would then allow a broad spectrum of many new physics discoveries and applications.

As mentioned in the previous chapter, various aspects of the electromagnetic interaction are usually studied using sophisticated numerical simulation codes. Vast majority of these codes, however, use a paraxial approximation (closer described in chapter 1) to prescribe the laser fields at the boundaries, and afterwards, a field solver propagates the beam across the simulation domain. As already mentioned, the paraxial approximation is valid only if the angular spectrum of the laser pulse is sufficiently narrow. Therefore, it is not possible to simulate tightly focused laser beams using this approach. As will be seen later, the paraxial approximation in this case leads to a distorted field profiles which would have strong impact on the laser-matter interaction results.

Several interesting solutions, how to simulate strongly focused beams, have been already proposed [source]. Within this work, a simple and efficient algorithm for a Maxwell consistent calculation of the electromagnetic fields at the boundaries of the computational domain [source] (also called laser boundary conditions) has been used and implemented into the PIC code EPOCH [source]. Note that this algorithm is able to describe laser beams with an arbitrary shape in the focal spot.

4.1 Laser boundary conditions

In this section, another mathematical description of a focused laser beam based on a rigorous solution of the wave equation 1.39 is presented. The following calculations are reproduced

from the work of Illia Thiele et al. [source]. Assume that the laser beam propagates in vacuum without external sources along the z-axis of the Cartesian coordinate system. The wave equation 1.39 in temporal Fourier space has the following form,

$$\Delta \hat{\mathbf{E}}(\mathbf{r}, \omega) + \frac{\omega^2}{c^2} \hat{\mathbf{E}}(\mathbf{r}, \omega) = 0, \quad (4.1)$$

where the hat symbol placed on the top of a variable denotes the Fourier transform with respect to time. Next, one shall perform a spatial Fourier transform of 4.1 with respect to transverse coordinates \mathbf{r}_\perp only,

$$\left(-k_x^2 - k_y^2 + \frac{\partial^2}{\partial z^2} \right) \bar{\mathbf{E}}(k_x, k_y, z, \omega) + \frac{\omega^2}{c^2} \bar{\mathbf{E}}(k_x, k_y, z, \omega) = 0, \quad (4.2)$$

where the bar symbol placed on the top of a variable denotes the Fourier transform with respect to time and spatial transverse coordinates. The equation 4.2 can be simplified as follows,

$$k_z^2(\mathbf{k}_\perp, \omega) \bar{\mathbf{E}}(\mathbf{k}_\perp, z, \omega) + \frac{\partial^2}{\partial z^2} \bar{\mathbf{E}}(\mathbf{k}_\perp, z, \omega) = 0. \quad (4.3)$$

where $k_z(\mathbf{k}_\perp, \omega) = \sqrt{-\mathbf{k}_\perp^2 + \omega^2/c^2}$ and $\mathbf{k}_\perp = (k_x, k_y)^T$. The fundamental solution of the equation 4.3 consists of the forward (+) and backward (-) propagating waves,

$$\bar{\mathbf{E}}^\pm(\mathbf{k}_\perp, z, \omega) = \bar{\mathbf{E}}_0^\pm(\mathbf{k}_\perp, \omega) e^{\pm i k_z(\mathbf{k}_\perp, \omega)(z-z_0)}. \quad (4.4)$$

Where $\bar{\mathbf{E}}_0^\pm(\mathbf{k}_\perp, \omega)$ is the electric laser field at some plane $z = z_0$. It might be clearly seen, that only two out of six vector components of the electric and magnetic fields are independent, therefore one may prescribe for example the transverse components $\bar{\mathbf{E}}_{0,\perp}^\pm(\mathbf{k}_\perp, \omega)$ at the plane $z = z_0$ and all other components can be derived from the Maxwell's equations 1.1, 1.3,

$$\bar{\mathbf{E}}_\perp^\pm(\mathbf{k}_\perp, z, \omega) = \bar{\mathbf{E}}_{0,\perp}^\pm(\mathbf{k}_\perp, \omega) e^{\pm i k_z(\mathbf{k}_\perp, \omega)(z-z_0)}, \quad (4.5)$$

$$\bar{E}_z^\pm(\mathbf{k}_\perp, z, \omega) = \mp \frac{\mathbf{k}_\perp \cdot \bar{\mathbf{E}}_\perp^\pm(\mathbf{k}_\perp, z, \omega)}{k_z(\mathbf{k}_\perp, \omega)}, \quad (4.6)$$

$$\bar{\mathbf{B}}_\perp^\pm(\mathbf{k}_\perp, z, \omega) = \frac{1}{\omega k_z(\mathbf{k}_\perp, \omega)} \mathbb{R}^\pm(\mathbf{k}_\perp, \omega) \bar{\mathbf{E}}^\pm(\mathbf{k}_\perp, z, \omega), \quad (4.7)$$

where

$$\mathbb{R}^\pm(\mathbf{k}_\perp, \omega) = \begin{pmatrix} \mp k_x k_y & \mp [k_z^2(\mathbf{k}_\perp, \omega) + k_y^2] & 0 \\ \pm [k_z^2(\mathbf{k}_\perp, \omega) + k_x^2] & \pm k_x k_y & 0 \\ -k_y k_z(\mathbf{k}_\perp, \omega) & -k_x k_z(\mathbf{k}_\perp, \omega) & 0 \end{pmatrix}. \quad (4.8)$$

Analogically, one could solve the wave equation for the magnetic field 1.40, prescribe two transverse components of $\bar{\mathbf{B}}_{0,\perp}^\pm(\mathbf{k}_\perp, \omega)$ at the plane $z = z_0$ and afterwards calculate all other fields using Maxwell's equations 1.2, 1.4. The complete proof, that the fields 4.5 - 4.7 are consistent with the Maxwell's equations in vacuum 1.1 - 1.4 can be found in the original paper [source].

Note that for $k_\perp^2 > \omega^2/c^2$, $k_z(\mathbf{k}_\perp, \omega)$ becomes imaginary and equation 4.4 describes evanescent waves that are unphysical in free space. Thus the Fourier spectrum of laser waves has to be filtered in the transverse Fourier space. On the other hand, if the spatial Fourier spectrum contains only components with $k_\perp^2 \ll \omega^2/c^2$, then $k_z(\mathbf{k}_\perp, \omega)$ can be approximated using the first few terms of a Taylor series,

$$k_z(\mathbf{k}_\perp, \omega) \approx \frac{|\omega|}{c} - \frac{c}{2|\omega|} k_\perp^2. \quad (4.9)$$

Note that by plugging 4.9 into equations 4.5 - 4.7 one gets the paraxial approximation.

In the last part of this section, the practical algorithm for implementation of the boundary conditions based on the previously derived solution of Maxwell's equations is presented. Assume that the laser beam propagates in a forward direction along the z -axis. In the beginning, it is necessary to prescribe the electric laser field $\mathbf{E}_{0,\perp}(\mathbf{r}_\perp, t)$ in the plane \mathcal{P} at $z = z_0$. Note, that it can be defined by arbitrary function of space and time. The goal is then to find the fields $\mathbf{E}_B(\mathbf{r}_\perp, t)$ and $\mathbf{B}_B(\mathbf{r}_\perp, t)$ at the corresponding boundary $z = z_B$.

Consider that the transverse part of simulation domain is made of equidistant rectangular grid described by x^i, y^j , where $i, j \in \{1, \dots, N_{x,y}\}$, and the grid steps $\delta x, \delta y$. The simulation time t^n , where $n \in \{1, \dots, N_t\}$, is also divided into equidistant time steps of size δt .

The algorithm allows to calculate fields $\mathbf{E}_B^{ij}(t)$ and $\mathbf{B}_B^{ij}(t)$ for any given time t from the interval $[t^1 - \frac{z_B - z_0}{c}, t^{N_t} - \frac{z_B - z_0}{c}]$. In order to preserve clarity, the algorithm below is given in the exact form as in the original paper [source].

1. Calculate $\hat{\mathbf{E}}_{0,\perp}^{ijn}$ via discrete Fourier transforms in time:

$$\omega^n = \frac{2\pi}{N_t \delta t} \left(-\frac{N_t}{2} + n \right), \quad (4.10)$$

$$\hat{\mathbf{E}}_{0,\perp}^{ijn} = \frac{\delta t}{2\pi} \sum_{l=1}^{N_t} \mathbf{E}_{0,\perp}^{ijl} e^{i\omega^n t^l}, \quad n \in \{1, \dots, N_t\}. \quad (4.11)$$

2. Calculate $\bar{\mathbf{E}}_{0,\perp}^{ijn}$ via two-dimensional discrete Fourier transforms in transverse space:

$$k_x^i = \frac{2\pi}{N_x \delta x} \left(-\frac{N_x}{2} + i \right), \quad k_y^j = \frac{2\pi}{N_y \delta y} \left(-\frac{N_y}{2} + j \right), \quad (4.12)$$

$$\bar{\mathbf{E}}_{0,\perp}^{ijn} = \frac{\delta x \delta y}{(2\pi)^2} \sum_{l,m=1}^{N_x, N_y} \hat{\mathbf{E}}_{0,\perp}^{lmn} e^{-i(k_x^i x^l + k_y^j y^m)}, \quad i, j \in \{1, \dots, N_{x,y}\}. \quad (4.13)$$

3. Calculate transverse electric field components at the boundary $z = z_B$:

$$k_z^{ijn} = \Re \sqrt{\frac{(\omega^n)^2}{c^2} - (k_x^i)^2 - (k_y^j)^2}, \quad (4.14)$$

$$\bar{\mathbf{E}}_{B,\perp}^{ijn} = \begin{cases} \bar{\mathbf{E}}_{0,\perp}^{ijn} e^{ik_z^{ijn}(z_B - z_0)} & \text{for } k_z^{ijn} > 0 \\ 0 & \text{for } k_z^{ijn} = 0 \end{cases}. \quad (4.15)$$

4. Calculate longitudinal electric field components at the boundary $z = z_B$:

$$\bar{E}_{B,z}^{ijn} = \begin{cases} -\frac{k_x^i \bar{E}_{B,x}^{ijn} + k_y^j \bar{E}_{B,y}^{ijn}}{k_z^{ijn}} & \text{for } k_z^{ijn} > 0 \\ 0 & \text{for } k_z^{ijn} = 0 \end{cases}. \quad (4.16)$$

5. Calculate the magnetic field at the boundary $z = z_B$:

$$\mathbb{R}^{ijn} = \begin{pmatrix} -k_x^i k_y^j & (k_x^i)^2 - (\omega^n)^2/c^2 \\ (\omega^n)^2/c^2 - (k_y^j)^2 & k_x^i k_y^j \\ -k_y^j k_z^{ijn} & k_x^i k_z^{ijn} \end{pmatrix}, \quad (4.17)$$

$$\bar{\mathbf{B}}_B^{ijn} = \begin{cases} (\omega^n k_z^{ijn})^{-1} \mathbb{R}^{ijn} \bar{\mathbf{E}}_{B,\perp}^{ijn} & \text{for } k_z^{ijn} > 0 \\ 0 & \text{for } k_z^{ijn} = 0 \end{cases}. \quad (4.18)$$

6. Calculate $\hat{\mathbf{E}}_B^{ijn}$, $\hat{\mathbf{B}}_B^{ijn}$ via two-dimensional inverse discrete Fourier transforms:

$$\hat{\mathbf{E}}_B^{ijn} = \frac{(2\pi)^2}{N_x N_y \delta x \delta y} \sum_{l,m=1}^{N_x, N_y} \bar{\mathbf{E}}_B^{lmn} e^{i(k_x^l x^i + k_y^m y^j)}, \quad (4.19)$$

$$\hat{\mathbf{B}}_B^{ijn} = \frac{(2\pi)^2}{N_x N_y \delta x \delta y} \sum_{l,m=1}^{N_x, N_y} \bar{\mathbf{B}}_B^{lmn} e^{i(k_x^l x^i + k_y^m y^j)}. \quad (4.20)$$

7. Calculate $\mathbf{E}_B^{ij}(t)$, $\mathbf{B}_B^{ij}(t)$ for any given time $t \in [t^1 - \frac{z_B - z_0}{c}, t^{N_t} - \frac{z_B - z_0}{c}]$.

$$\mathbf{E}_B^{ij}(t) = \frac{2\pi}{N_t \delta t} \sum_{n=1}^{N_t} \hat{\mathbf{E}}_B^{ijn} e^{-i\omega^n t}, \quad (4.21)$$

$$\mathbf{B}_B^{ij}(t) = \frac{2\pi}{N_t \delta t} \sum_{n=1}^{N_t} \hat{\mathbf{B}}_B^{ijn} e^{-i\omega^n t}. \quad (4.22)$$

4.2 Implementation

One of the main goals of this work has been to implement the algorithm mentioned in the previous section, to evaluate its correctness in several test simulations and finally, to exploit resulting implementation for simulations of tightly focused Gaussian beams in laser-matter interaction. The main requirement on implementation was fast integration with the 2D version of particle-in-cell simulation code EPOCH [source]. For this reason, several possible solutions have been taken into account.

The final decision was to create a static library, which will be able to compute desired quantities and will provide functions for communication with the main simulation code. The essential advantage is that it could be basically linked with any laser-plasma simulation code. Also, since it is necessary to call only two additional functions, the instrumentation will be fast, easy and the main simulation code will not be excessively disturbed. Furthermore, the implementation itself come with the CMake [source] support, which simplify the compilation process using platform and compiler independent configuration files.

The library has been written in C++ language in the object-oriented style, so the algorithm can be easily extended to the three dimensional geometry. In order to speedup the whole underlying computation, the algorithm has been parallelized using hybrid techniques. The time domain has been decomposed into the stripes corresponding to individual computational processes, the communication between these processes is ensured by MPI library. Furthermore, the computationally most expensive cycles are parallelized using OpenMP implementation of multi-threading. Later on, the speedup and parallel scaling performance will be briefly discussed.

Fourier transforms form the core of the computational process and their performance is crucial for the overall performance of the code. For this reason, many currently available libraries have been considered. Eventually, the Fourier transforms in the algorithm can be computed using FFTW [source] library, Intel® MKL [source] library or it is also possible to directly evaluate the formulas without using any additional library. User specifies his option before the compilation of the code. Regarding both libraries, a threaded versions of 1D in-place complex fast Fourier transforms have been used throughout the code. According to several measures, there is no significant difference between the speed of both libraries. On Intel® architectures, the MKL library [source] has slightly better performance though.

One potential bottleneck could happen during the computation of spatial Fourier transforms since the arrays with spatial data are decomposed into different processes. The cluster versions of functions performing the Fourier transforms have been tested, however they did not bring any significant speedup. The reason is as follows. They require to have the global array in memory and use its own distribution which involves overlapping. Since the size of

global arrays is usually not so large and since it is necessary to perform a lot of different Fourier transforms, the majority of computational time is spent rather for communication, mainly if many of computational cores are used.

This issue has been solved by gathering the data on master process, performing the Fourier transforms in space by only one processor and scattering the data back to corresponding processes. This is the reason why the code does not scale well, however, the time to compute all desired quantities is in most cases negligible in comparison with the time required by the main simulation cycle. Nevertheless, this could be a suggestion for future improvement.

Since it is necessary to compute the whole time evolution of the laser field at boundary for each grid point before the simulation starts, the resulting amount of data can be significantly large and does not have to fit in a computer RAM. Thus, it is inevitable to dump the data into a file, which will be then accessed by the main simulation code. Due to the performance purposes, each computational process stores its data into a shared file with corresponding offset and in binary coding. Therefore, the output operations are as fast as possible and save the storage resources. Library then provide a function which allows to seek an arbitrary position in a file. This function is then called each time step of the main simulation loop to fill the laser source arrays with all the relevant data. This way of accessing data does not cause any significant slowdown or memory overhead.

The EPOCH [source] code require only transverse components of the laser electric field, all other quantities are computed by the FDTD solver. The implementation of the library allows full connection with EPOCH [source]. In practice, if user wants to simulate tight-focusing, it is necessary to enable the corresponding flag as a compile-time option and then to specify all required parameters in the input file. The code then automatically computes all necessary data. It works generally regardless the number of lasers in the simulation or boundaries that they are attached to.

The current version of library does not work for obliquely incident laser pulses, because in this case one cannot exploit the advantage of an efficient computation with fast Fourier transforms. However, the code allows to compute the laser fields at boundary by evaluating Fourier integrals directly, so it could be easily extended. Second, it is at the moment possible to simulate only Gaussian laser pulses. However, user can prescribe its own shape and position of the beam in focal plane by modifying corresponding part of the code.

Several most important data structures, functions and methods that form the core of the library for tight-focusing can be seen in appendix B.

4.3 Evaluation

To evaluate the correctness of the algorithm presented in the previous section of this chapter as well as to demonstrate the drawbacks of the paraxial approximation, several test simulations in 2D geometry have been performed. In the following text, a two limit cases are



Figure 3: Transverse (E_y) and longitudinal (E_x) electric laser field components captured at the time step of their maximal intensity at the focal spot. The cases (a), (b) correspond to the laser pulse initialized using the paraxial approximation, whilst (c), (d) come from the simulation where the beam at the boundary is given by the Maxwell consistent approach. In the case of paraxial approximation, both components reveal strong distortions and asymmetry, their focal spot is located about 1λ closer to the left boundary than specified and the corresponding amplitude is significantly lower. The laser has been attached to the left hand side boundary.

presented. The first pair of simulations employs tightly focused Gaussian laser beam with the size at focus comparable with the center laser wavelength, whilst the second one shows the case of the Gaussian beam with the size at focus one order of magnitude larger than the center laser wavelength, where both approaches should return identical results. Note, that all the simulations have been computed using 2D version of PIC code EPOCH [source] instrumented with library for tight-focusing.

The simulation of a tightly focused Gaussian beam is considered first. The p-polarized laser pulse with center wavelength $\lambda = 1 \mu\text{m}$ propagates from left hand side boundary to the right. Its duration has been chosen to $\tau = 20 \text{ fs}$ in FWHM and amplitude $E_0 = 1 \cdot 10^{15} \text{ V/m}$. The beam waist $w_0 = 0.7 \mu\text{m}$ is shorter than the laser wavelength, which implies that non-

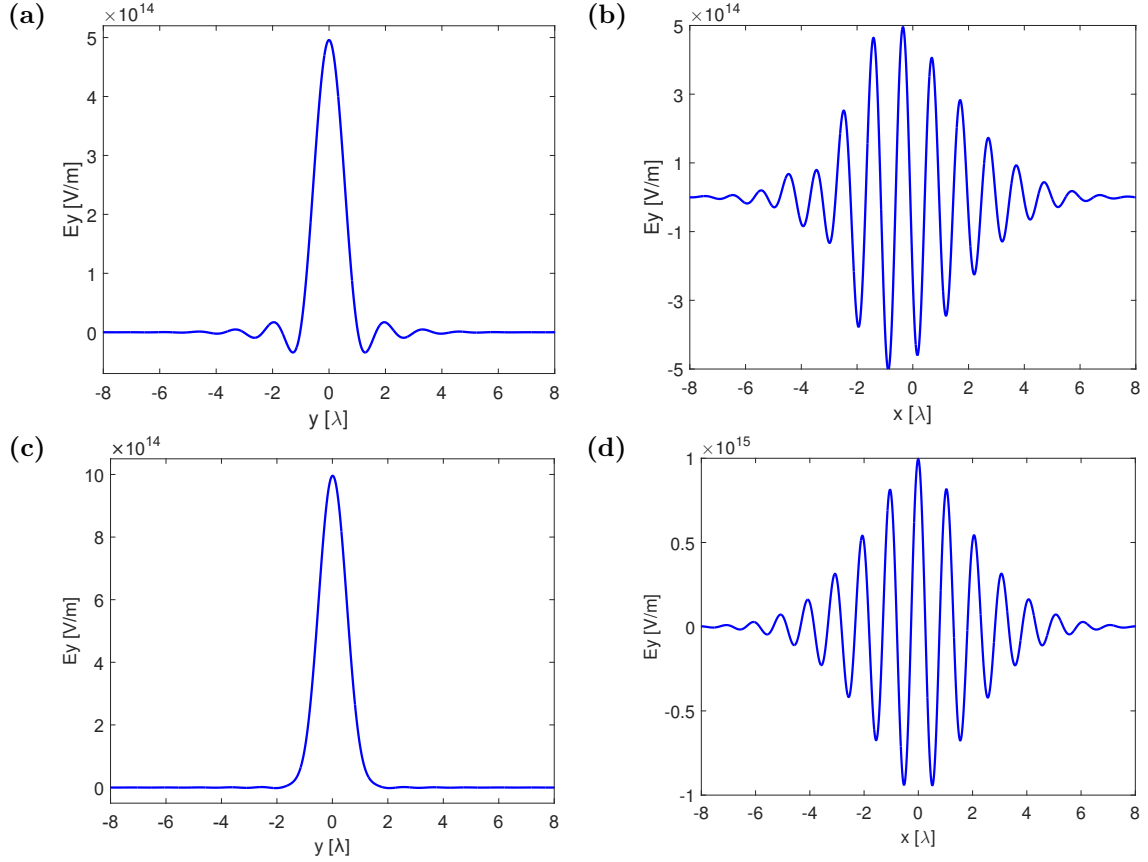


Figure 4: Transverse (a), (c) and longitudinal (b), (d) slices of the transverse electric laser field (E_y) at the time step when it reaches maximal intensity at the focal spot. The cases (a), (b) correspond to the laser pulse initialized using the paraxial approximation, whilst (c), (d) come from the simulation where the beam at the boundary is given by the Maxwell consistent approach. In the case of paraxial approximation, one can clearly see strong side-wings in the spatial beam profile (a) as well as the asymmetry of the field in the longitudinal line-out (b).

negligible parts of $\bar{\mathbf{E}}_{0,\perp}(k_x, \omega)$ are evanescent. The focus is located at a distance $x = 8 \mu\text{m}$ from the boundary that the laser is attached to.

The size of the simulation domain is $16\lambda \times 48\lambda$, with 100 cells per laser wavelength in both directions, thus $\Delta x = \Delta y = \lambda/100 = 10 \text{ nm}$. The simulation time step is chosen to satisfy the CFL condition [source] $\Delta t = 0.95\sqrt{2}\lambda/100c \approx 0.05 \text{ fs}$ and the whole simulation time is $t = 150 \text{ fs}$. The pulse propagates in vacuum in order to get rid of all effects that could be potentially caused by plasma. All the simulation parameters can be found in the attached input files in the appendix A.

In the following paragraph, the results of the first simulation are discussed in more details. Fig. 3 shows the transverse and longitudinal electric field components at their maximal intensity at focus for two cases. First, for the laser beam which has been initialized using the

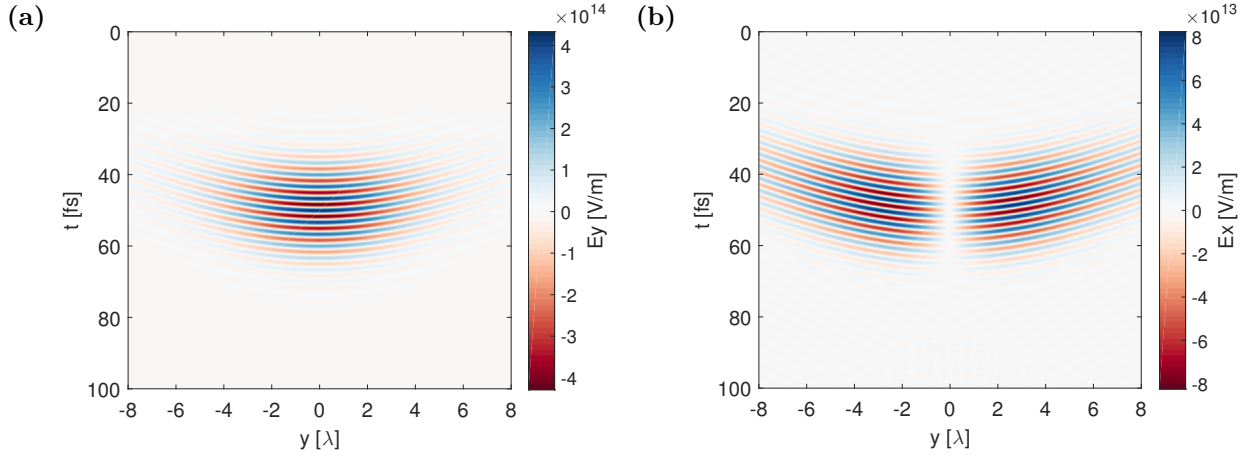


Figure 5: The time evolution of transverse (E_y) (a) and longitudinal (E_x) (b) electric laser field components at the boundary that the laser is attached to. Both components have been calculated according to the Maxwell consistent approach.

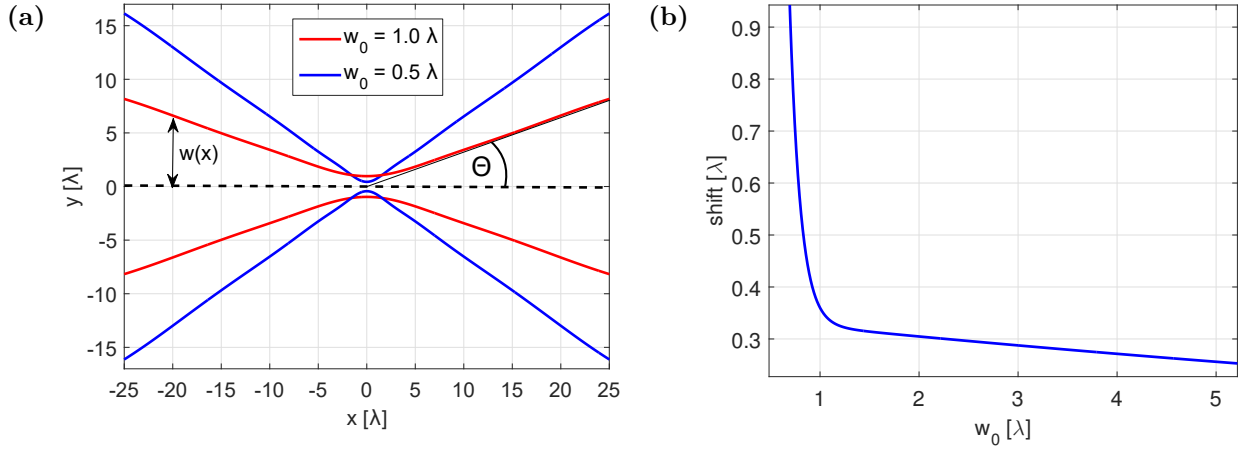


Figure 6: (a) Graph of the spot size parameter $w(x)$ of the beams with $w_0 = 1\lambda$ and 0.5λ calculated using Maxwell consistent approach. From the plotted lines, one can roughly estimate the beam divergence angle Θ . The divergence angles for both beams are surprisingly in a good accordance with the formula for divergence angles of corresponding Gaussian beams. (b) Dependency of the absolute focal point shift on the beam waist w_0 for the laser beam initialized using the paraxial approximation. One can see sharp increase of the error for $w_0 < \lambda$. In both cases, values have been dumped at discrete time intervals and interpolated.

paraxial approximation (fig. 3-a, 3-b), i.e. the electric field at the boundary is given by the equation 1.55, and second, according to the approach consistent with the Maxwell's equations (fig. 3-c, 3-d). In the case of paraxial approximation, one can clearly see strong distortions and asymmetry in the shape of both electric field components. In addition, the focus location

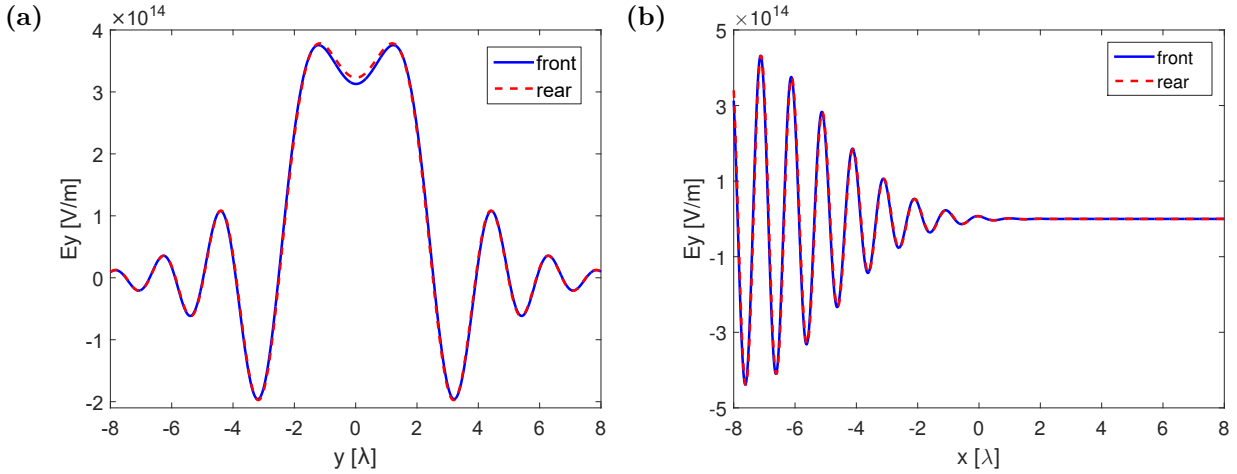


Figure 7: Transverse (a) and longitudinal (b) slice of the transverse electric laser field (E_y) when it reaches its maximal intensity at the front (blue) and rear (red) boundary. The results come from the simulation where the laser beam at the boundary has been calculated using the Maxwell consistent approach. For better comparison, the field at the rear boundary in (b) has been horizontally flipped. The exact match between the field shapes at a different time steps of simulation proves the correctness of the laser beam propagation.

is shifted about $1 \mu\text{m}$ closer to the left boundary and the corresponding amplitude at focus is less than half the required value. In contrast, the fields produced by the simulation using Maxwell consistent calculation of laser fields at boundary are symmetric with respect to the focal spot and without any distortions. Furthermore, the focus location as well as the amplitude fulfills the initial requirements precisely.

Fig. 4 shows transverse and longitudinal slices of transverse electric field component at focus for the case of the laser beam initialized using the paraxial approximation (fig. 4-a, 4-b) as well as for the case where the beam at the boundary is given by the Maxwell consistent approach (fig. 4-c, 4-d). For the case of paraxial approximation, one can clearly see the asymmetry of the field shape in the longitudinal slice (fig. 4-b), which consequently leads to a decrease of the amplitude at focus and to the strong side-wings in the spatial beam profile, as might be better seen from the transverse slice (fig. 4-a). On the other hand, Maxwell consistent approach calculates fields of perfect symmetry with respect to the focal spot (fig. 4-c) and no side-wings or distortions are present (fig. 4-d).

In fig. 5 one can look through the time evolution of transverse (fig. 5-a) and longitudinal (fig. 5-b) electric field components at the boundary as computed using the Maxwell consistent approach. Note that one must chose carefully the transverse size of the domain, since the beam width at boundary may be much larger than at focus because of a diffraction. To estimate the beam width at the boundary, one has to know the beam divergence angle Θ . In fig. 6-a, one can find a graph of the spot size parameter w as calculated using the Maxwell consistent approach for the beams focused to $w_0 = 1 \lambda$ and 0.5λ . From the plotted lines,



Figure 8: (a) Graph of the transverse (E_y) electric laser field amplitude with respect to the distance from the focal spot. The values on vertical axis are given in a percentage of the amplitude at focus $E_{y,0}$. (b) Graph of the maximal instantaneous laser intensity with respect to the distance from focal spot. The values on vertical axis are given in a percentage of the laser intensity at focus I_0 . In both cases, values have been computed using the Maxwell consistent approach, dumped at discrete time intervals and interpolated.

one can roughly estimate the beam divergence angle Θ . For the beam focused to $w_0 = 1 \lambda$, the beam divergence angle has been around $\Theta = 18.2^\circ$ which is almost identical value as for the Gaussian beam of the same parameters. For the beam with $w_0 = 0.5 \lambda$ the divergence has been estimated to $\Theta = 32.9^\circ$, while the Gaussian beam with the same size at focus has divergence $\Theta = 36.5^\circ$. Consequently, in spite of the fact that the divergence of the tightly focused beams calculated using the Maxwell consistent approach is a little bit lower, both approaches are in quite a good accordance regarding this parameter and one can use the angle Θ given by the equation 1.43 as a rough estimate even for tight-focusing.

To evaluate a correctness of the propagation of the beam prescribed using the Maxwell consistent approach, several criteria has been defined. The correctness of the amplitude and beam waist as well as the right focus location has already been verified. Additional criteria has been set on a beam symmetry. In fig. 7, one can find a comparison of the transverse electric laser field component when it achieves its maximal intensity at front and rear boundary. One can clearly see the exact match between the field shapes at different time steps of the simulation in transverse (fig. 7-a) and longitudinal (fig. 7-b) slices. Moreover, all the aforementioned criteria has been fulfilled also in other simulations with different input parameters that are not presented here. Consequently, these observations prove the correctness of the simulation at least for the tightly focused Gaussian laser beams.

In fig. 6-b, one may find the estimate of the absolute focal point shift with respect to the prescribed position of the beam waist. The interpolated values come from the simulations where the laser beam has been initialized using paraxial approximation. One can clearly see the sharp increase of the error for $w_0 < \lambda$. On the other hand, for $w_0 = 5 \lambda$ the shift is

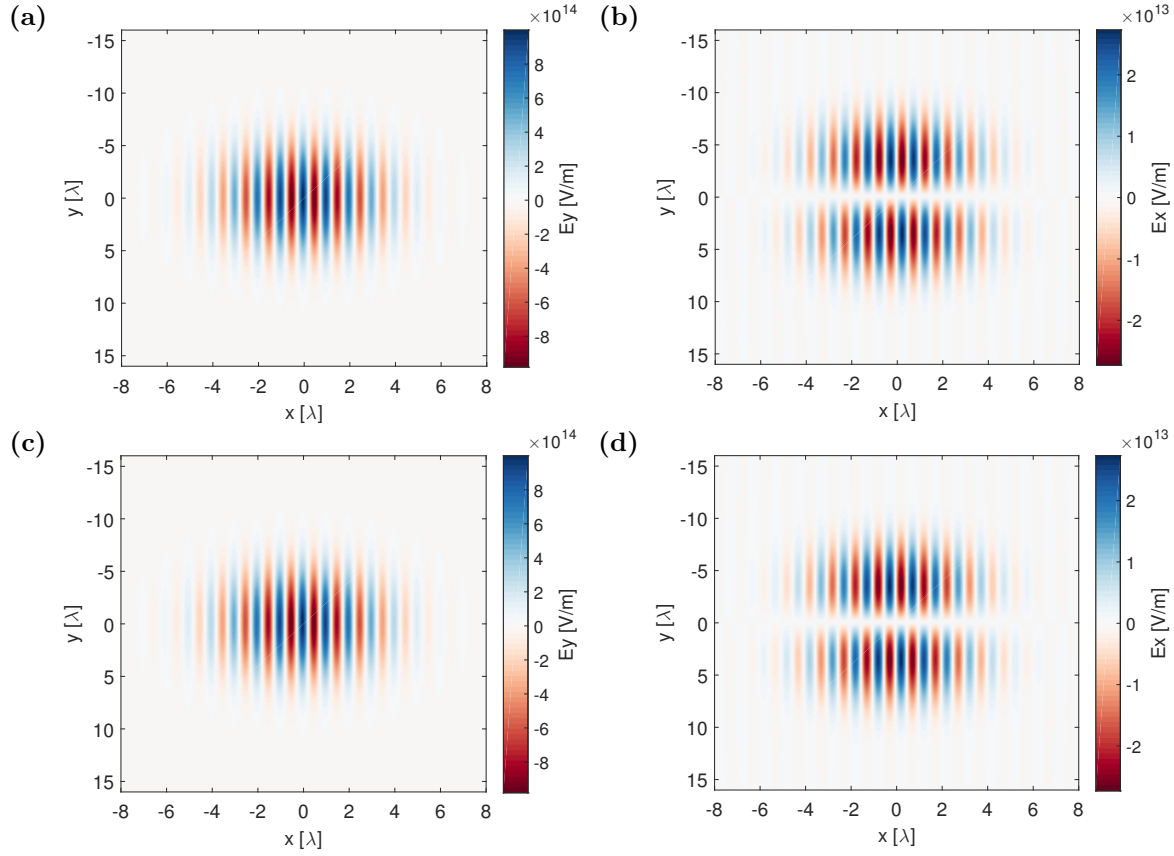


Figure 9: Transverse (E_y) and longitudinal (E_x) electric laser field components captured at the time step of their maximal intensity at the focal spot. The cases (a), (b) correspond to the laser pulse initialized using the paraxial approximation, whilst (c), (d) come from the simulation where the beam at the boundary is given by the Maxwell consistent approach. The size of the focus has been chosen to be one order of the magnitude larger than the center laser wavelength. One can clearly see, that there is no significant difference between the shapes of the electric field components.

around 0.2λ which is negligible in comparison with the Rayleigh range.

In fig. 8-a, one can see the amplitude of the transverse electric laser field with respect to the distance from the focal spot calculated using Maxwell consistent approach. This could be particularly useful for experiments since it is not always easy to focus the beam onto the target surface perfectly. Sometimes, one might be more interested in the laser intensity rather than the amplitude of the electric field. For this reason, fig. 8-b shows the instantaneous maximal laser intensity in the narrower spatial interval calculated from the values of the electric field amplitude.

Up to now, we have demonstrated the results of simulations with tight-focusing. In the following, comparison of the two numerical methods for the beam focused to a larger spot size characterized by $w_0 = 5 \lambda$ is presented. Except for the beam waist, all the input parameters



Figure 10: Transverse (a) and longitudinal (b) slices of the transverse electric laser field (E_y) at the time step when it reaches maximal intensity at focus. Red lines correspond to the laser pulse initialized using the paraxial approximation, whilst blue lines come from the simulation where the beam at the boundary is calculated by the Maxwell consistent approach (LBCS). The size of the focus has been chosen to be one order of magnitude larger than the center laser wavelength. In the case of paraxial approximation, the focus is slightly shifted closer to the left boundary (b), otherwise the size of the focus as well as the amplitude is correct for both cases (a).

remained the same. The parameter $w_0 = 5 \lambda$ is about the limit case for the beam initialized using the paraxial approximation. Thus, one expects that the simulation results of both methods should be almost identical.

Similarly as in fig. 3, fig. 9 shows again transverse and longitudinal electric field components at their maximal intensity at focus for both cases, laser beam initialized using the paraxial approximation (fig. 9-a, 9-b) and according to the approach consistent with the Maxwell's equations (fig. 9-c, 9-d). Here, one cannot register any difference between the results corresponding to both approaches. Also, the transverse slice of the transverse electric laser field component at focus (fig. 10-a) shows the correct shape and amplitude for both cases. The longitudinal slice (fig. 10-b), however, points out the fact that the location of the focal spot is still a little bit shifted closer to the left hand side boundary. Nevertheless, this difference could be neglected in practice. At the end of the day, the beam diameter at focus should be at least one order of magnitude larger than the center laser wavelength for the Gaussian beams propagating in the paraxial approximation.

In conclusion, one should be aware that the propagation of tightly focused laser pulses cannot be described by paraxial approximation. It has been shown above that for the beams focused to a spot with the size comparable to a center laser wavelength, paraxial approximation leads to a shifted location of the focus, asymmetric laser field profiles with distortions and lower amplitude. These deviations are far from negligible and have without doubt a strong impact on the laser-matter or laser-plasma interaction results. On the other hand,

the propagation of tightly focused Gaussian laser beams prescribed at boundaries according to the Maxwell consistent approach has been proven to be correct.

It has been also verified that the paraxial approximation can be safely used when the beam size at focus is about one order of magnitude larger than the center laser wavelength, such that $w_0 \geq 5 \lambda$. In this case, the laser fields are symmetric with respect to the focal point, the laser intensity fulfills specified requirements precisely, only the location of the focus is shifted about 0.2λ closer to the boundary at which the laser is attached to. However, in this case, the simulations generally produce physically relevant results, therefore the effect of the focal point shift can be neglected in practice.

Regarding the validity and trustworthiness of simulation results, no exact threshold for the size of the focal spot for laser beams initialized using the paraxial approximation has been determined. The rate of unphysical effects also depends on investigated phenomena and other laser pulse properties, such as intensity or duration. Thus the frequently used simulation set-up for beams with the waist $w_0 = 3 \lambda$ can be in many situations justified.

4.4 Overview of experimental methods

In this section, several possible approaches for focusing a laser beam in experiments are discussed. Before providing a brief overview of currently used methods, it is necessary to introduce a few most fundamental parameters that describe any optical system.

First, one defines a numerical aperture of an optical system NA , which is a dimensionless number characterizing the range of angles over which the system can accept or emit light. Second characteristic of any optical system is a focal length f describing a distance between the center of the aperture and the point in space over which collimated light rays are brought to a focus. Finally, one defines a f-number $f/\#$ as a ratio of the focal length f to the size of the aperture D . The f-number is thus dimensionless and stands for a quantitative measure of a speed of the optical system.

In experiments, focusing of laser beams is usually achieved by means of an optical system, such as a lens or a curved mirror. However, when dealing with short pulses, lenses (in general transmissive optics) are not preferred because they may affect the beam and consequently the quality of the focal spot (Strehl ratio, encircled energy) by frequency-dependent effects, such as chromatic aberration and other nonlinear optical distortions. On the other hand, reflective optics are generally able to produce a diffraction limited focus without chromatic effects.

4.4.1 Off-axis parabolic mirror

An off-axis parabolic mirror is a frequently used tool to focus an incoming collimated beam. It is made by cutting out a small section from a full parabolic mirror and thus it allows to deviate the beam path off the optical axis. Therefore, the focal point is at more accessible

location and the target is not blocking the incoming collimated laser beam as in the case of a complete parabolic mirror. Obviously, the off-axis parabolic mirror is able to work reversibly, so it can take the light coming from a point source and produce a collimated beam. These physical properties make the off-axis parabolic mirror a valuable tool for many different optical purposes.

As the laser intensities exceed 10^{13} W/cm^2 , the surface of any material becomes strongly ionized. Therefore, in order to keep the energy density on the optical components below the damage threshold, the beam diameter has to be increased. The beam diameter is usually constrained by the cost of the optical components.

The focal spot can be decreased by implementing a small f-number focusing optic. However, since their focal length is inevitably very short and therefore they must be placed in close proximity to the interaction region, additional care has to be taken to protect the optical components because they can be easily damaged from debris induced by the exploded target flow. Note that such optics are typically very expensive.

4.4.2 Focusing plasma mirror

In the case of focusing at low f-numbers (tight-focusing), the conventional solid state optics are inappropriate. Nevertheless, many of the drawbacks mentioned above might be overcome by using a plasma-based focusing optic. As already mentioned in the chapter 2, when the laser pulse with intensity higher than 10^{16} W/cm^2 hits a solid target, a thin dense plasma layer is immediately formed on its surface. Under certain conditions, the plasma becomes dense enough and the reflectivity of otherwise non-reflecting target strongly increases. The incident laser light is reflected at the critical plasma density, thus the dense plasma acts as a mirror. For this reason, such optical components are called plasma mirrors.

Plasma mirrors are able to operate under much higher energy density than the conventional solid state optics, therefore the diameter of the optics aperture can be more than one order of magnitude smaller. Consequently, plasma mirrors can be mass-produced at much lower cost, which is crucial since they are single-use and therefore have to be replaced after each shot. In addition, the concerns about damage from target debris are naturally eliminated.

To induce focusing, the surface of plasma mirror has to be curved similarly as in the case of conventional optics. However, since the distance between the mirror and the interaction region can be very small, the corresponding f-number is also small, thus enabling to focus an incident laser beam theoretically to a spot size smaller than the laser wavelength. In addition, plasma mirrors are attractive also due to their ability to improve the temporal and spatial contrast ratio of the laser pulse, which is crucial for many applications of the laser-matter interaction.

The diagram in fig. 11-a schematically shows an experimental configuration for tight-focusing. A conventional off-axis parabolic mirror is aligned in such a way that the focus coincides with the first focal point of the ellipsoidal focusing plasma mirror. The ellipsoidal



Figure 11: (a) Schematic diagram showing the experimental set-up for tight-focusing. The incoming laser beam is focused by a conventional off-axis parabolic mirror to the first focal point of the ellipsoidal plasma mirror. Beyond the first focus light diverges and is reflected from the dense plasma created on the surface of plasma mirror. The beam is then imaged to the second focal spot where the target should be placed. (b) Photo taken at Extreme Light Infrastructure (ELI) laser facility capturing a very long and frustrating procedure of the off-axis parabolic mirror set-up.

shape of the mirror provides point-to-point imaging, possesses no spherical aberration and allows relatively simple alignment procedure. The light reflected from the plasma mirror is then imaged to the second focal spot, where the target is placed. The fig. 11-b shows the set-up of the off-axis parabolic mirror with an ellipsoidal plasma mirror in practice.

4.4.3 Plasma lens

Alternative to a plasma mirror could be a plasma lens. This concept is based on creating a short plasma channel which is able to guide an intense laser pulse. The plasma channel can be formed by variations in either the laser intensity across the beam regions or a plasma density. In the higher laser intensity region, plasma is pushed aside in the radial direction of the beam due to the ponderomotive force (see chapter 2). This effect reduces the plasma density locally and consequently increases the index of refraction of the plasma. The resulting index of refraction is seen by the laser pulse as a focusing lens, thus prevents it from further spreading. Note that apart from ponderomotive force, there is a variety of other mechanisms that lead to a change of the refractive index of plasma. These include collisions, thermal, or relativistic effects.

Similarly as for the plasma mirrors, plasma lenses would tolerate energy densities above the damage threshold for conventional solid state optics and allow to manipulate with the laser beam in close proximity to the interaction region. The focal length of the plasma lens is expected to be independent of the laser intensity as long as the interaction regime

is non-relativistic. The plasma lens may, in principle, be tuned by controlling the plasma density. Consequently, it would be possible to change the position of the focal point without physically moving any optical element [source].

4.4.4 Conical targets

Recently, it has also been shown by PIC simulations that a tightly focused laser beams could be potentially obtained by using cone-shaped targets. More specifically, the inner surface of the hollow cone that is open at both ends interacts with the outer parts of incoming collimated laser beam leading to the surface ionization and generation of dense plasmas. The laser beam structure is in turn modified and its energy is gradually squeezed due to the multiple reflections. In spite of the laser energy absorption by the target walls, the laser pulse is nonlinearly guided to the cone tip that can result in a highly localized spot of around wavelength radius with the peak intensity amplified by an order of magnitude.

The PIC simulations have also shown, that after leaving the cone-tip opening, the tightly focused laser beam is still fairly coherent and can propagate over a distance of several wavelengths before it starts to diffract. This fact indicates that the hollow cone might act as an optical device that focuses down the laser pulse to a wavelength level.

The cone-focusing effect is mainly characterized by the material, the opening angle and the cone tip size of the target. By controlling these parameters, a laser pulse can be focused efficiently and the quality of the focal spot can be significantly enhanced. However, the tip of the cone channel has to be of a dimension comparable to the laser wavelength, making the manufacturing process difficult at present. Such a small conical channel should be realizable in the near future with the rapid advances in nanofabrication.

Chapter 5

2D simulations of focused laser beams

In this chapter, the results of several large-scale simulations are presented. More specifically, 2D3V PIC simulations of tightly focused p-polarized Gaussian laser beams interacting with solid targets at normal incidence have been performed. Note that all the simulations have been computed using the code EPOCH (see chapter 3) which has been instrumented with the library enabling to simulate tightly focused laser beams (see chapter 4). The calculated data have been processed and thoroughly analyzed. Emphasis has been placed mainly on identifying the effects of the laser beam focal spot size on the laser-matter interaction results.

5.1 Simulation model and initial conditions

In total, three sets of simulations have been conducted. The first set contains simulations of laser pulses with constant energy $E \approx 30$ mJ and four different sizes of the focal spot characterized by $w_0 = 0.5, 1.0, 2.0$ and $4.0 \mu\text{m}$. Two more sets for the same beam waists as before and constant peak intensities $I = 10^{20} \text{ W/cm}^2$ and $I = 10^{21} \text{ W/cm}^2$ have been calculated to be able to better distinguish between the intensity-dependent effects and the effects of the focal spot size.

Apart from the laser intensity I and the beam waist w_0 , all the input parameters remained identical for all simulations. The p-polarized Gaussian laser pulse with the wavelength $\lambda = 0.8 \mu\text{m}$ and the duration $\tau = 30$ fs in FWHM propagates from the left hand side boundary to the right. The focal spot is located at the surface of a solid target at the distance $x = 8 \mu\text{m}$ from the boundary that the laser is attached to. The laser pulse is incident normally.

The size of the simulation domain is $15 \mu\text{m} \times 40 \mu\text{m}$, with 1875 cells in the x-direction and 5000 cells in the y-direction. This domain set-up corresponds to 100 cells per λ in both directions, thus the simulation cell sizes $\Delta x = \Delta y = \lambda/100 = 8 \text{ nm}$ are similar to the minimum Debye length in the simulation box. The simulation time step is chosen to fulfill the CFL condition [source] $\Delta t = C\sqrt{2}\lambda/100c$, where the CFL constant is $C = 0.95$, thus $\Delta t \approx 0.035$ fs. The peak laser intensity hits the target at $t \approx 100$ fs, the whole simulation

time has been then specified to $t = 150$ fs.

The distance between the left hand side boundary and the front side of the solid target of density $100 n_c(\omega)$ is $8 \mu\text{m}$, the width of the target is $30 \mu\text{m}$ and the thickness $2 \mu\text{m}$. The target is initially at rest and is made of electrons and protons that are represented by weighted computational particles, which number per one simulation cell is 2000 for electrons and 100 for protons. Therefore, each electron represents 5 % of $n_c(\omega)$ and each proton 100 % of $n_c(\omega)$. The initial temperature of both particle species is constant throughout the target and equal to 100 eV.

The boundary conditions are thermalizing to the initial temperature for particles and CPML with thickness of 16 cells for fields on all sides of the simulation box. The collisions of plasma particles are not accounted for since their contribution to laser energy absorption can be neglected under considered conditions. The quantum electrodynamics effects are not included as well.

In total, the simulation domain contains $9.6 \cdot 10^6$ cells and $2 \cdot 10^9$ computational particles ($1.9 \cdot 10^9$ electrons, $9.4 \cdot 10^7$ protons). The whole simulation requires approximately 4125 time steps. The template for all the simulation input files can be found in the appendix A.

5.2 Simulation results

In this section, the results of simulations performed within this work are presented. Due to the limited space, we decided to attach figures only for the beams focused down to $w_0 = 2.0 \mu\text{m}$ and $w_0 = 0.5 \mu\text{m}$. These represent the cases of the focal spot larger than the center laser wavelength and the focal spot of a sub-wavelength level. Nevertheless, the results of simulations for other focal spot sizes are compared and briefly discussed as well. In spite of the fact that in terms of physical relevance it would be more proper to compare the results of simulations with constant beam energies, they are discussed here only very briefly, because it is too difficult to recognize and distinguish only the effects of the focal spot size on the laser-matter interaction results.

First, the results have been analyzed in terms of the laser energy absorption efficiency. The comparison of the total laser light absorption in plasma for all performed simulations is shown in the table 2. It might be clearly seen that there is no significant difference between the absorption rates for the simulations where the beam is focused to a focal spot larger than the center laser wavelength whilst its peak intensity remains constant. On the other hand, in the case of the sub-wavelength focus, the rate of the energy absorption sharply increases. The ratio between the absorption of the beam focused to $w_0 = 1.0 \mu\text{m}$ and $w_0 = 0.5 \mu\text{m}$ is 1.7 in the case of the laser intensity $I = 10^{20} \text{ W/cm}^2$ and 1.34 in the case of the intensity $I = 10^{21} \text{ W/cm}^2$.

The absorption rates for the laser beam with constant energy strongly depends on the laser intensity at focus. As can be seen from the table 3, the simulations consequently result in increasing the hot electron temperature and maximum ion energy as the focal spot size

w_0 [μm]	Total absorption of laser energy [%]		
	const. $E \approx 30$ mJ	const. $I = 10^{20}$ W/cm 2	const. $I = 10^{21}$ W/cm 2
0.5	20.12	16.23	31.77
1.0	9.59	9.59	23.76
2.0	5.27	8.26	23.82
4.0	3.49	8.29	23.71

Table 2: Total laser energy absorption in plasma for several different sizes of the focal spot and different laser intensities.

w_0 [μm]	$k_B T$ of hot electrons [MeV]	maximum energy of ions [MeV]
0.5	0.93	4.73
1.0	0.64	1.71
2.0	0.32	0.74
4.0	0.16	0.43

Table 3: Temperature of hot electrons estimated by fitting the energy distributions at the time $t = 100$ fs by Maxwellian functions and the maximum ion energy at the time $t = 150$ fs for the laser beam with constant energy $E \approx 30$ mJ and several different sizes of the focal spot.

decreases. Therefore, to better understand the dependency of the energy absorption on the size of the focal spot, it is better to further study the results of laser-matter interaction for the laser beams with constant intensities.

The temporal evolution of the kinetic energy of particles normalized to the laser pulse energy can be seen in the fig. 12. The maximum kinetic energy of electrons occurs when the peak intensity reaches the target at the time $t = 100$ fs. Even before that, when the hot electron population becomes significant (~ 80 fs) ion acceleration sets in. In the case of these intensities and the p-polarization, it is dominated by the TNSA processes closer described in the chapter 2. The plots indicate that as the focal spot size increases, the energy transfer to ions is faster. This may have two reasons. Either the electric field induced by the expanding hot electrons on the target surface is higher or it decays more slowly with time. Note that even if the absorption is lower for larger spot size, the amount of energy absorbed in the target is higher because of the four times higher laser energy. Nevertheless, to understand the energy transfer from hot electrons to ions, one has to identify the main plasma heating and energy absorption mechanisms.

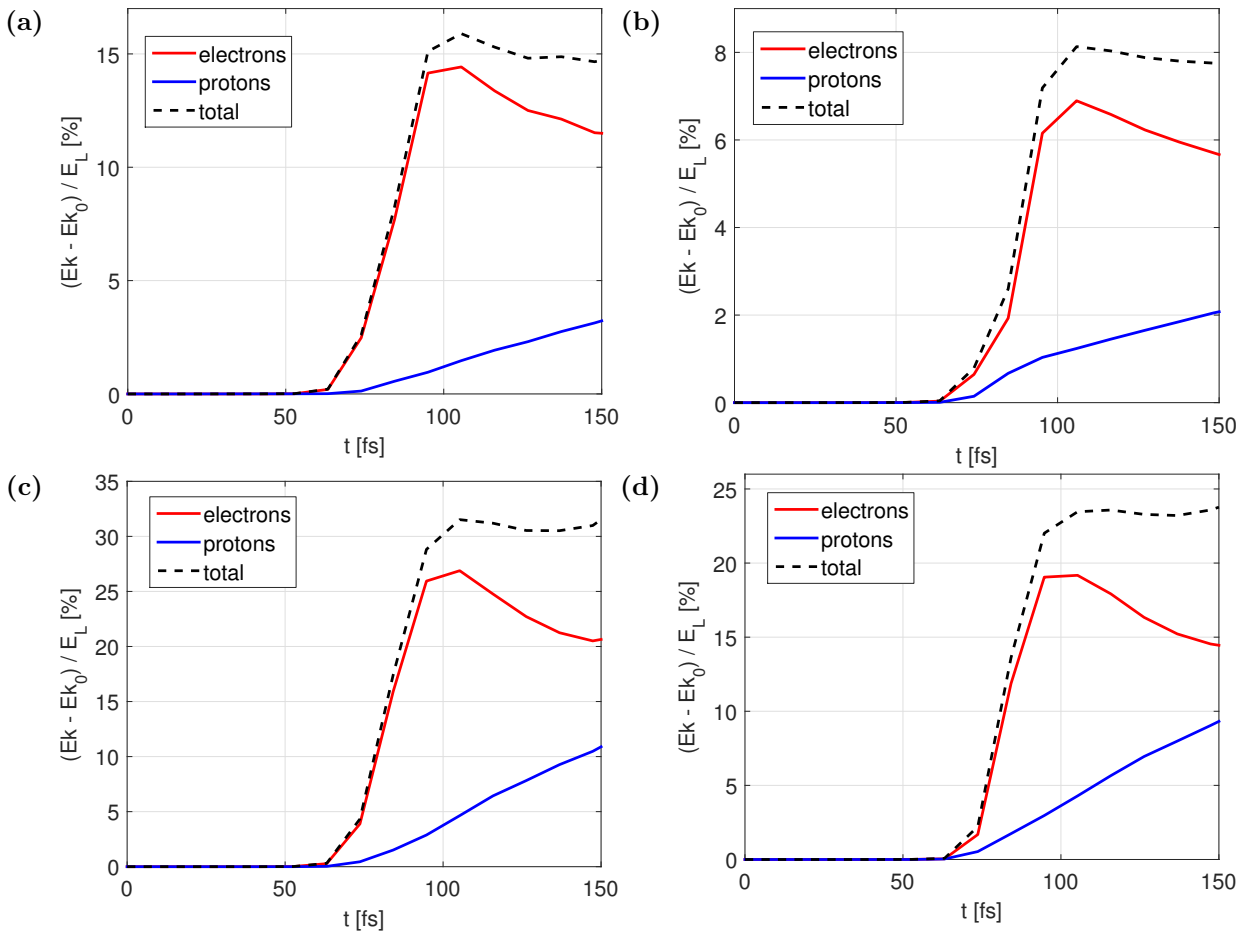


Figure 12: The kinetic energy E_k of particles (E_{k0} denotes the initial kinetic energy of particles) normalized to the laser pulse energy E_L in time for the case of simulations with the laser intensity $I = 10^{20} \text{ W/cm}^2$ and with the beam waist (a) $w_0 = 0.5 \mu\text{m}$, (b) $w_0 = 2.0 \mu\text{m}$ and for the case of simulations with the laser intensity $I = 10^{21} \text{ W/cm}^2$ and with the beam waist (c) $w_0 = 0.5 \mu\text{m}$, (d) $w_0 = 2.0 \mu\text{m}$.

It is expected that the dominating absorption mechanism is $\mathbf{J} \times \mathbf{B}$ heating for the laser intensities used in the simulations. The phase space of the parallel component of the momentum and the x-coordinate of all electrons in the simulation domain at the time $t = 100 \text{ fs}$ is shown in the fig. 13. The bunches of hot electrons that are ejected twice per laser period due to the $\mathbf{J} \times \mathbf{B}$ heating are more compact and clearly visible in the case of $w_0 = 2.0 \mu\text{m}$. The peak longitudinal momentum $p_x \approx 8 m_e c$ in the case of the laser intensity $I = 10^{20} \text{ W/cm}^2$ and $p_x \approx 22 m_e c$ in the case of the intensity $I = 10^{21} \text{ W/cm}^2$ independently of the focal spot size. On the other hand, the phase space looks similar in the region $|p_x| < 0.5$ of non-relativistic hot electrons. The main difference is that the number of these hot electrons is higher for the larger spot size. Yet another qualitative difference can be observed, there is

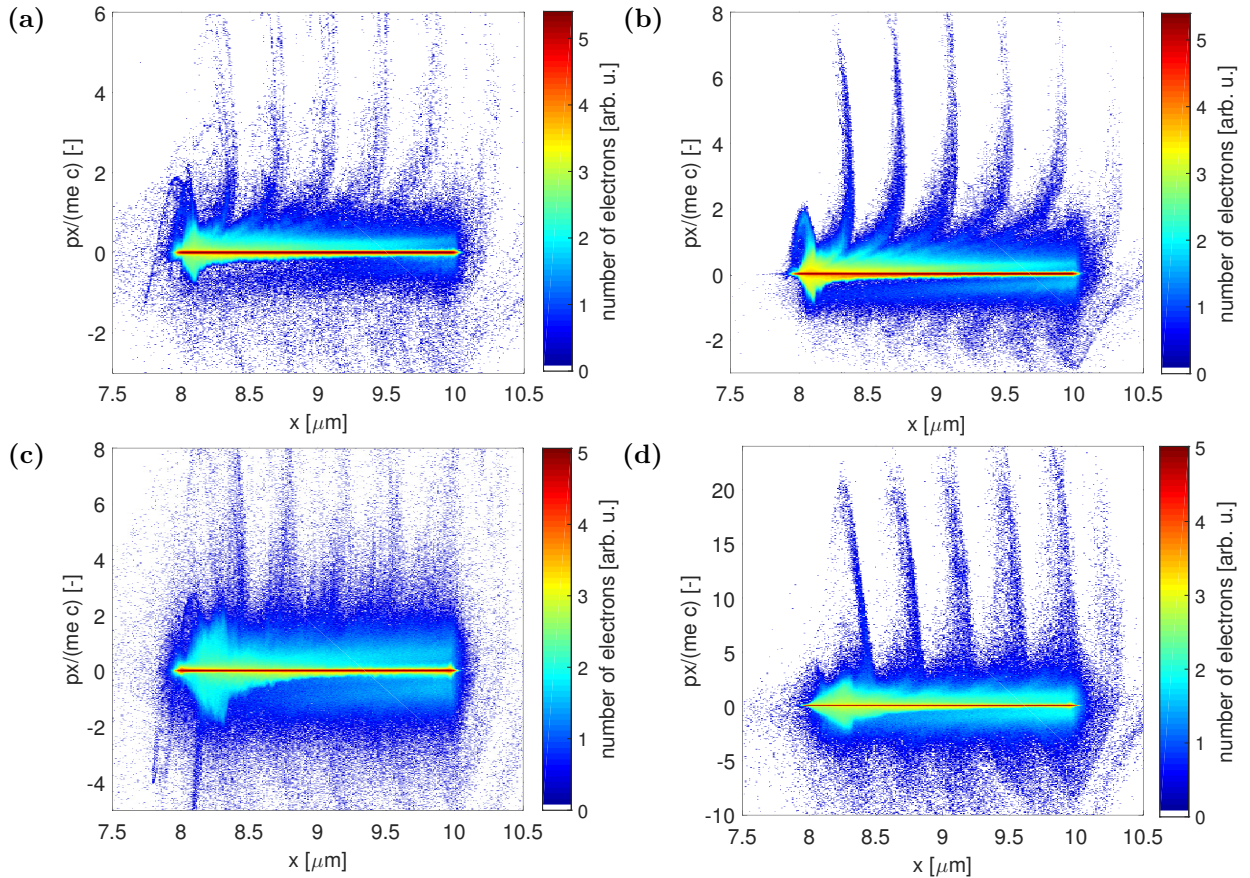


Figure 13: The phase space of the parallel component of the momentum (p_x) and the x-coordinate of all electrons in the simulation domain at the time $t = 100$ fs for the case of simulations with the laser intensity $I = 10^{20}$ W/cm 2 and with the beam waist (a) $w_0 = 0.5$ μm , (b) $w_0 = 2.0$ μm and for the case of simulations with the laser intensity $I = 10^{21}$ W/cm 2 and with the beam waist (c) $w_0 = 0.5$ μm , (d) $w_0 = 2.0$ μm . The color scales are logarithmic and the units are arbitrary, but the same for all sub-figures.

a significant cloud of hot electrons in front of the target for the smaller spot size which is missing for the larger one.

For deeper understanding, it might be useful to track trajectories of hot electrons. The fig. 14 shows such trajectories for the laser intensity $I = 10^{20}$ W/cm 2 . These electrons are tracked during three laser periods around the peak laser intensity and we show a randomly chosen 10 % of hot electrons that have the final γ factor at least two times higher than the initial one for this time interval. It turned out that most of the trajectories can be split up into two groups. The first type of trajectories corresponds to electrons that move along the front surface of the target towards the focal spot and in the vicinity of the focus, these electrons are pushed into the target by $\mathbf{J} \times \mathbf{B}$ force (fig. 14-a, 14-c). The second type of



Figure 14: Two types of trajectories of randomly chosen electron samples for the case of simulations with the laser intensity $I = 10^{20} \text{ W/cm}^2$ and with the beam waist **(a)**, **(b)** $w_0 = 0.5 \mu\text{m}$ and **(c)**, **(d)** $w_0 = 2.0 \mu\text{m}$. The trajectories are colored according to the Lorentz γ factor of corresponding particles.

trajectories corresponds to electrons that are initially inside the target, they come out to the target front surface as a return current and are pushed back to the plasma by $\mathbf{J} \times \mathbf{B}$ force (fig. 14-b, 14-d). Note that there is a significant quantitative difference between the two focal spot sizes for both types of trajectories. In the case of $w_0 = 0.5 \mu\text{m}$, there is approximately 59 % of electrons with the trajectories of the first type (fig. 14-a) and 41 % of the second type (fig. 14-b). On the contrary, for the simulation of $w_0 = 2.0 \mu\text{m}$, there is about 22 % of electrons with the trajectories of the first type (fig. 14-c) and 78 % of the second type (fig. 14-d). It also seems that the beam of accelerated electrons is more divergent in the case of the smaller spot size.

The electron trajectories are determined mainly by the field of incident laser pulse. In the fig. 15, one can see the longitudinal and transverse components of the ponderomotive force for the laser beam with intensity $I = 10^{20} \text{ W/cm}^2$ propagating in vacuum. The magnitude of longitudinal component is almost the same for both focal spot sizes (for the tight-focusing,



Figure 15: The longitudinal ($F_{p,x}$) (a) and the transverse ($F_{p,y}$) (b) component of the ponderomotive force for the case of the laser beam with intensity $I = 10^{20} \text{ W/cm}^2$ and the beam waist $w_0 = 0.5 \mu\text{m}$ propagating in vacuum. The longitudinal ($F_{p,x}$) (c) and the transverse ($F_{p,y}$) (d) component of the ponderomotive force for the case of the laser beam with intensity $I = 10^{20} \text{ W/cm}^2$ and the beam waist $w_0 = 2.0 \mu\text{m}$ propagating in vacuum. The ponderomotive force has been calculated according to the non-relativistic formula 2.41.

the force is not plotted exactly at the time of the peak laser intensity due to the discrete time step), but the transverse component is approximately 3.5 times higher in the case of $w_0 = 0.5 \mu\text{m}$. The ratio of the longitudinal component of the ponderomotive force to the transverse component is approximately 3.2 : 1 in the case of $w_0 = 0.5 \mu\text{m}$ (fig. 15-a, 15-b) and 12.8 : 1 in the case of $w_0 = 2.0 \mu\text{m}$ (fig. 15-c, 15-d). Note that for the laser intensity $I = 10^{21} \text{ W/cm}^2$, the values of ponderomotive force are one order of magnitude higher, but the ratios between longitudinal and transverse components remain identical.

The spatial distribution of the mean kinetic energy of electrons at the time $t = 80 \text{ fs}$ is shown in the fig. 16. The direction of electrons moving forward is given by the ratio of

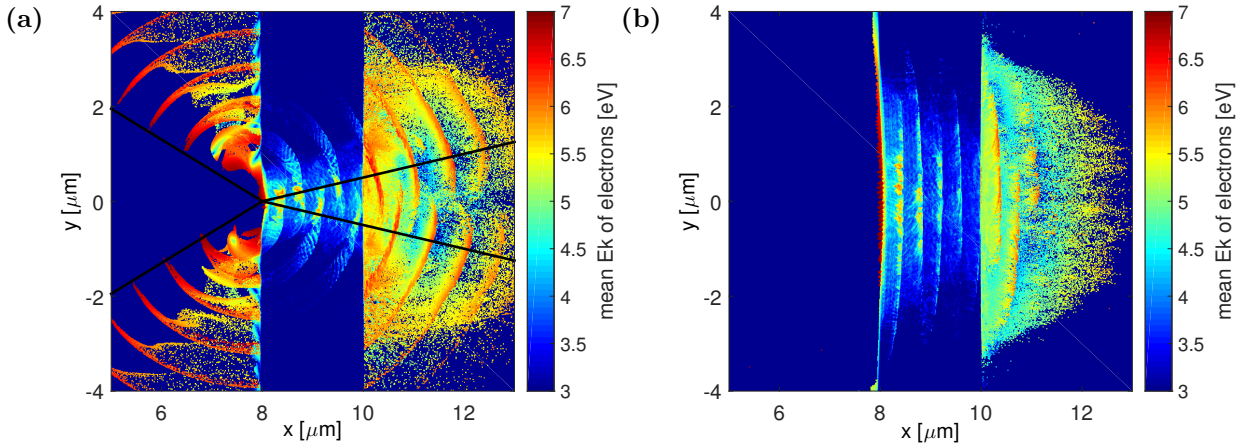


Figure 16: The spatial distribution of the mean kinetic energy of electrons at the time $t = 80$ fs for the case of simulations with the laser intensity $I = 10^{21} \text{ W/cm}^2$ and with the beam waist **(a)** $w_0 = 0.5 \mu\text{m}$, **(b)** $w_0 = 2.0 \mu\text{m}$. The color scales are logarithmic.

longitudinal component of the ponderomotive force to the transverse component. In the case of $w_0 = 0.5 \mu\text{m}$, the angle (marked by a black line in the fig. 16-a) is estimated to 17.4° , whilst in the case of $w_0 = 2.0 \mu\text{m}$ (fig. 16-b), the angle is only 4.5° . In both cases, one may see the bunches of hot electrons that are ejected twice per laser period. In addition, in the case of $w_0 = 0.5 \mu\text{m}$, one may also clearly see the electrons that move backwards. Their movement is restricted by the incoming laser beam (the laser divergence angle is marked by a black line in front of the target in the fig. 16-a).

The perpendicular component of the current density at the time $t = 100$ fs is shown in the fig. 17. In the case of $w_0 = 0.5 \mu\text{m}$ (fig. 17-a), one may register the electric current caused by the electrons ejected into vacuum at the front side. The charge unbalance is then compensated by the electric current along the front surface of the target and this might be the reason, why there is more electrons with the trajectories of the first type in this case. The fig. 17 also indicates a different shape of the target deformed during the hole boring phase. Therefore, one may be interested in contour lines of ion critical density that are shown in the fig. 18. Notice that in the case of $w_0 = 0.5 \mu\text{m}$, the plasma in the vicinity of incoming laser beam expands rapidly due to the space charge induced by electrons ejected into vacuum (marked by blue lines in the fig. 18-a, 18-b). It means that the absorption processes which take place when the laser pulse is obliquely incident on a plasma density gradient (such as resonance absorption or vacuum heating) may also significantly contribute to the overall laser energy absorption (table 2), e.g. the incidence angles for the laser intensity $I = 10^{21} \text{ W/cm}^2$ are about 20° and 1.5° for $w_0 = 0.5 \mu\text{m}$ and $w_0 = 2.0 \mu\text{m}$, respectively.

The spatial distribution of the mean kinetic energy of electrons at the time $t = 120$ fs in a global view is shown in the fig. 19. Again, one can clearly see that in the case of $w_0 = 0.5 \mu\text{m}$ (fig. 19-a), hot electrons spread out in the transverse direction more quickly than in the case

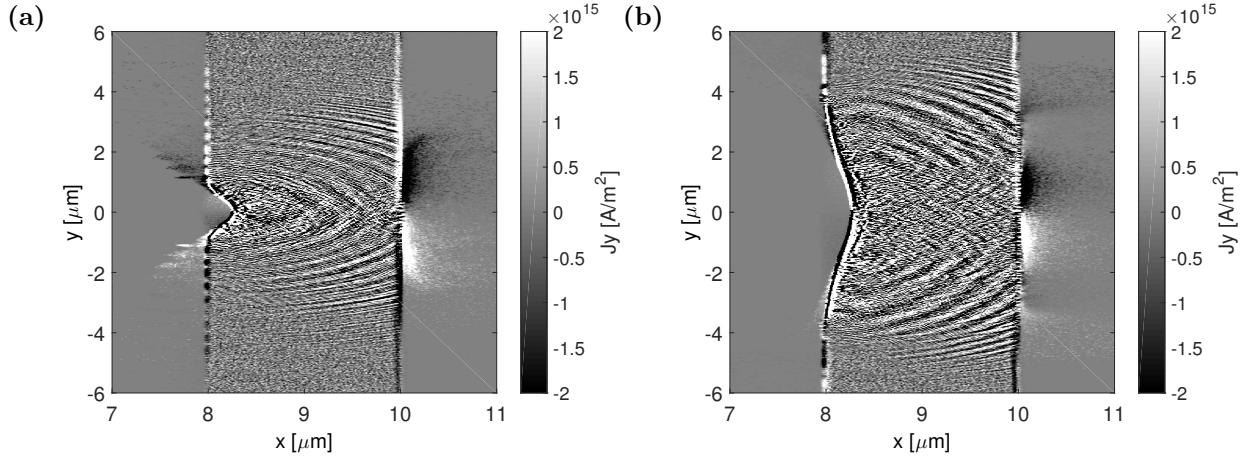


Figure 17: Perpendicular component of the current density J_y at the time $t = 100$ fs for the case of simulations with the laser intensity $I = 10^{21} \text{ W/cm}^2$ and with the beam waist (a) $w_0 = 0.5 \mu\text{m}$, (b) $w_0 = 2.0 \mu\text{m}$. The color scale is saturated to demonstrate the features of the transverse return current. The real current density in the focal region is much higher.

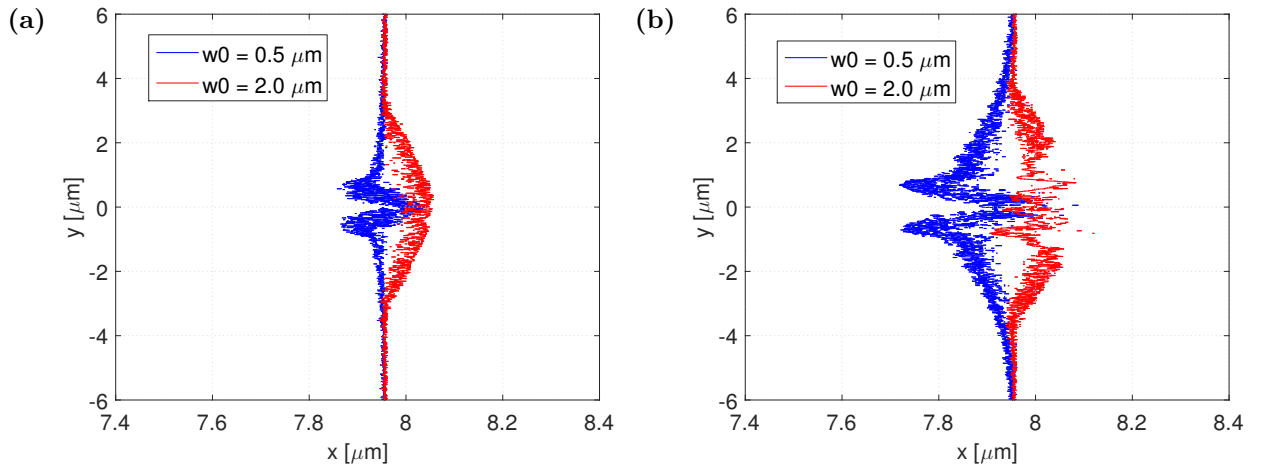


Figure 18: A contour lines of ion critical density for two different beam waists at the time $t = 100$ fs for the case of simulations with the laser intensity (a) $I = 10^{20} \text{ W/cm}^2$ and (b) $I = 10^{21} \text{ W/cm}^2$.

of $w_0 = 2.0 \mu\text{m}$ (fig. 19-b). For the laser intensity $I = 10^{21} \text{ W/cm}^2$, however, the difference is less noticeable (fig. 19-c, 19-d).

Additionally, the longitudinal component of the electric field in the simulation box at the time $t = 120$ fs is demonstrated in the fig. 20. Note that in the case of $w_0 = 2.0 \mu\text{m}$, the longitudinal electric field is slightly stronger, which is not observed in the fig. 20 due to the color saturation. As already mentioned, the hot electron energy is consequently transferred to ions faster. However, this is not the maximum longitudinal electric field, which occurs at



Figure 19: The spatial distribution of the mean kinetic energy of electrons at the time $t = 120$ fs for the case of simulations with the laser intensity $I = 10^{20}$ W/cm 2 and with the beam waist **(a)** $w_0 = 0.5$ μm , **(b)** $w_0 = 2.0$ μm and for the case of simulations with the laser intensity $I = 10^{21}$ W/cm 2 and with the beam waist **(c)** $w_0 = 0.5$ μm , **(d)** $w_0 = 2.0$ μm . The color scales are logarithmic and saturated.

$t = 100$ fs and it is stronger for smaller spot size at lower intensity. As a result, the field decays faster for the case of $w_0 = 0.5$ μm which is in agreement with higher divergence of hot electrons observed in this case. For the higher laser intensity the maximum longitudinal electric field is higher for the larger spot size so one cannot make the same conclusion about its faster decay. There is also a large difference between the shapes of the reflected laser light for both cases. While in the case of $w_0 = 2.0$ μm (fig. 20-b, 20-d) the laser light is reflected in a relatively narrow beam, in the case of $w_0 = 0.5$ μm (fig. 20-a, 20-c) the reflected light spreads radially outwards from the focal point. Nevertheless, divergence of the incident and the reflected laser beams are not much different.

The phase space of the parallel and the perpendicular components of the momentum of all

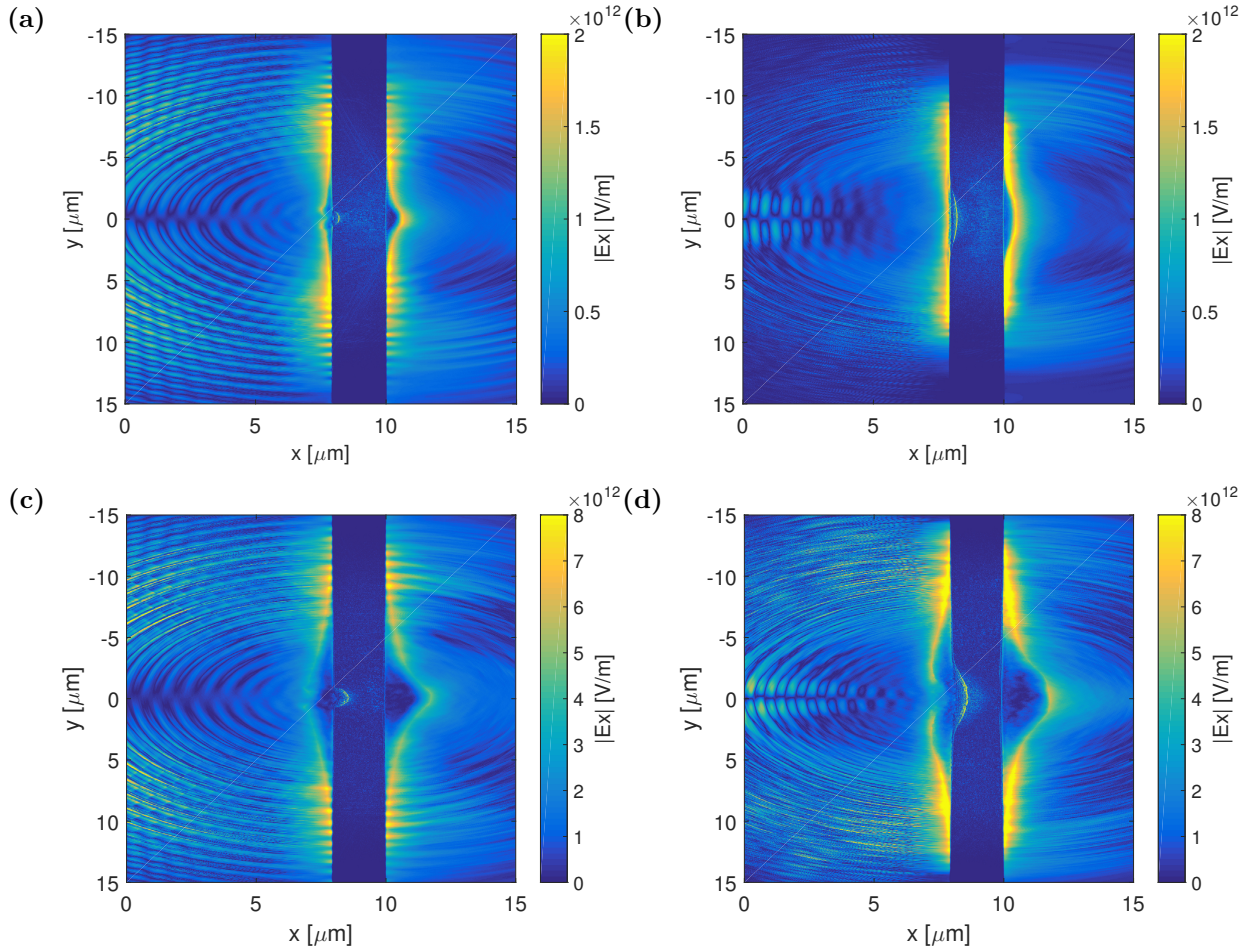


Figure 20: Longitudinal component of the electric field (E_x) at the time $t = 120$ fs for the case of simulations with the laser intensity $I = 10^{20}$ W/cm 2 and with the beam waist **(a)** $w_0 = 0.5$ μm , **(b)** $w_0 = 2.0$ μm and for the case of simulations with the laser intensity $I = 10^{21}$ W/cm 2 and with the beam waist **(c)** $w_0 = 0.5$ μm , **(d)** $w_0 = 2.0$ μm . Note that in the case of $w_0 = 2.0$ μm , the color scales are saturated.

electrons in the simulation domain at the time $t = 100$ fs is shown in the fig. 21. This might be particularly useful for determining the propagation direction of electrons. As one can clearly see, electrons propagate forward in a more collimated beam in the case of $w_0 = 0.5$ μm (fig. 21-a) than in the case of $w_0 = 2.0$ μm (fig. 21-b). For the laser intensity $I = 10^{21}$ W/cm 2 , there is no significant difference between the shape of both electron distribution functions (fig. 21-c, 21-d). Note that the first statement would be in a contradiction with the previous observations. The fig. 21, however, does not provide a complete information about the high-energy electrons.

The fig. 22 demonstrates the angular distribution of electrons in the whole simulation

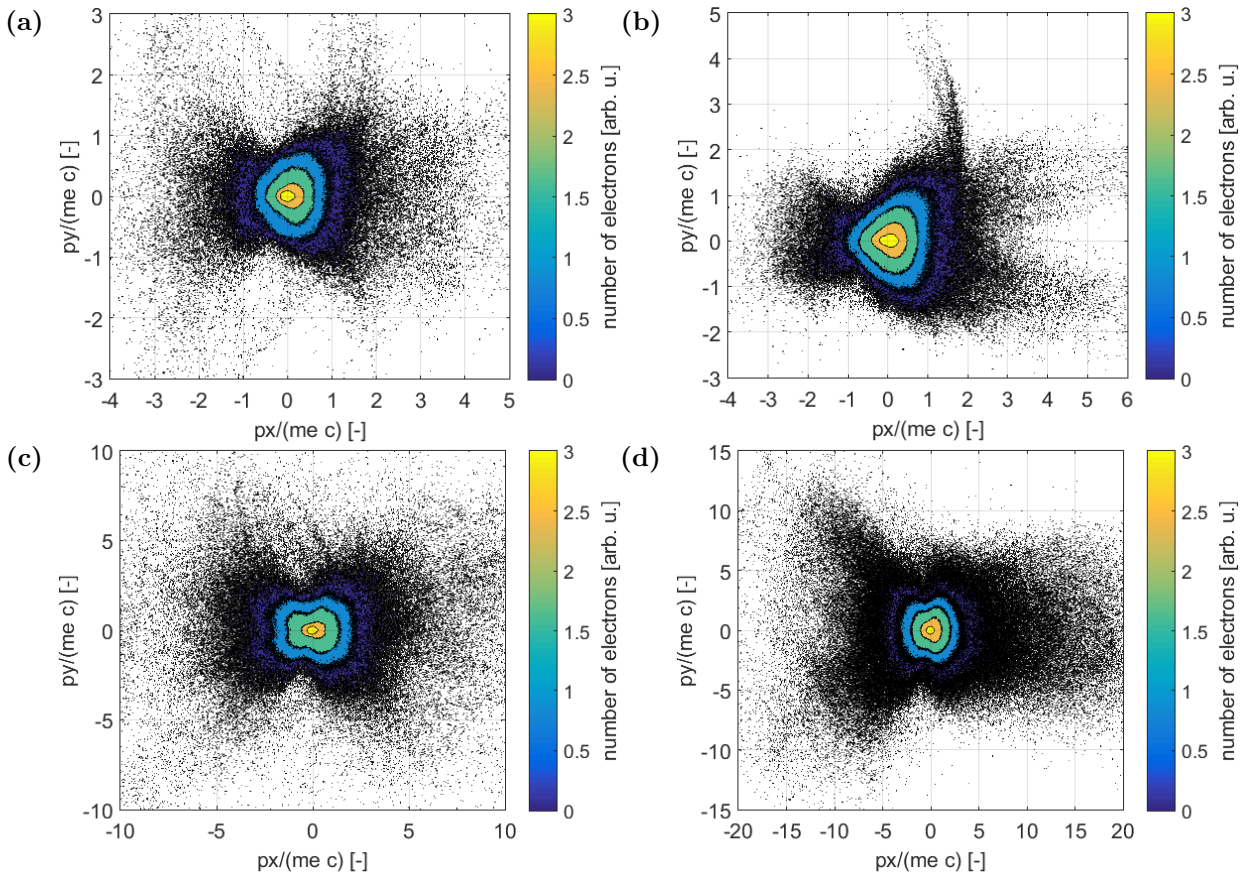


Figure 21: Phase space of the parallel (p_x) and the perpendicular (p_y) components of the momentum of all electrons in the simulation domain at the time $t = 100$ fs for the case of simulations with the laser intensity $I = 10^{20} \text{ W/cm}^2$ and with the beam waist **(a)** $w_0 = 0.5 \mu\text{m}$, **(b)** $w_0 = 2.0 \mu\text{m}$ and for the case of simulations with the laser intensity $I = 10^{21} \text{ W/cm}^2$ and with the beam waist **(c)** $w_0 = 0.5 \mu\text{m}$, **(d)** $w_0 = 2.0 \mu\text{m}$. The color scales are logarithmic and the units are arbitrary, but the same for all sub-figures.

domain at the time $t = 100$ fs. It might be seen that in the case of $w_0 = 0.5 \mu\text{m}$, the lower-energy electrons (green and blue lines in the fig. 22-a) propagate forward in a narrower beam than in the case of $w_0 = 2.0 \mu\text{m}$ (green and blue lines in the fig. 22-b) which is in accordance with the fig. 21. The divergence angle of the high-energy electrons propagating forward is almost identical for both cases (red line in the fig. 22-a, 22-b). However, in the case of $w_0 = 0.5 \mu\text{m}$, there is much more electrons spreading in the transverse direction (angle of $\pm\pi/2$) with respect to the incidence direction of the incoming laser pulse. Regarding the laser intensity $I = 10^{21} \text{ W/cm}^2$, the angular distribution of lower-energy electrons is more isotropic (green and blue lines in the fig. 22-c, 22-d). The high-energy electrons propagate forward in a more collimated beam in the case of $w_0 = 2.0 \mu\text{m}$ (red line in the fig. 22-d).

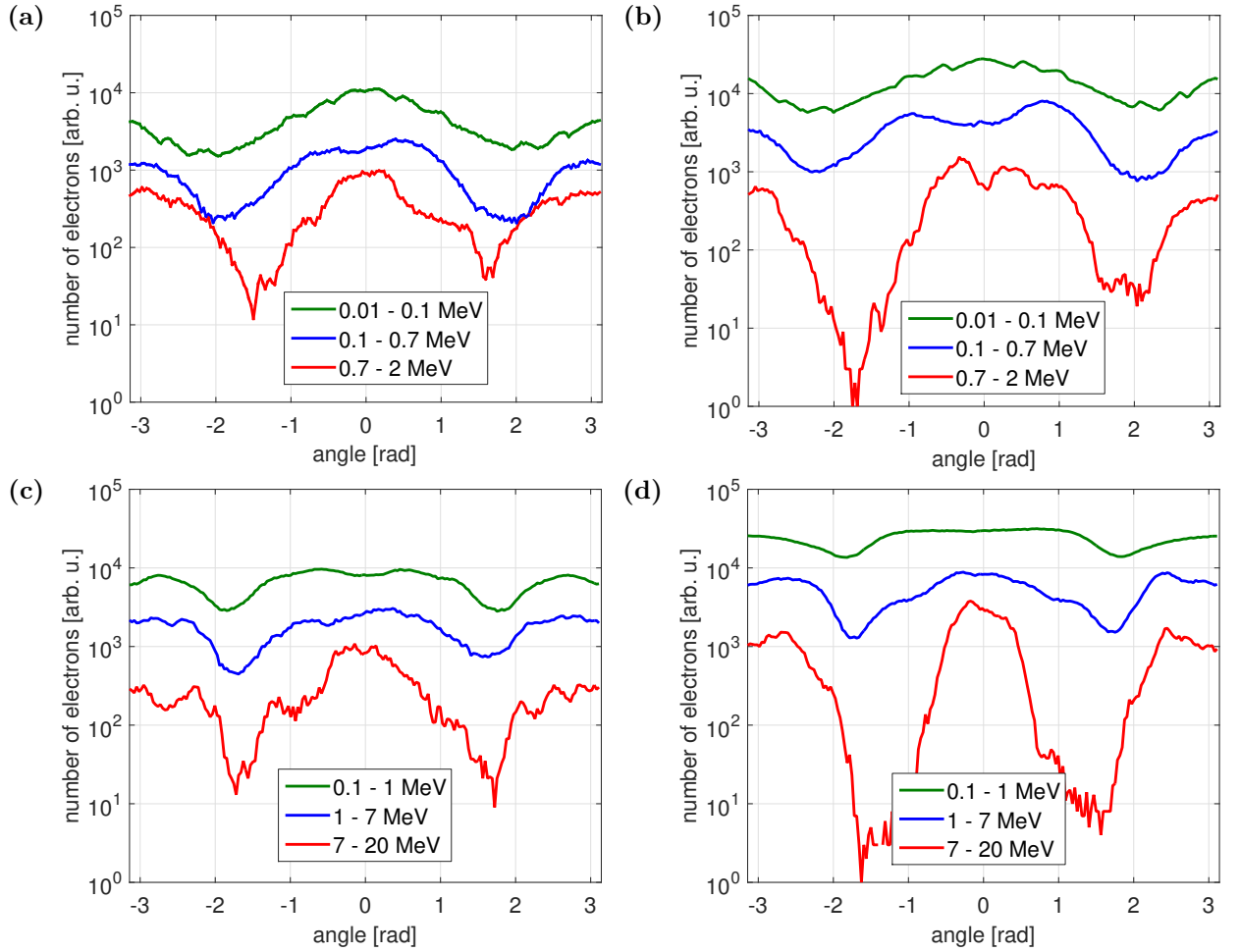


Figure 22: Angular distribution of electrons (the angle is measured with respect to the laser incidence direction) in the whole simulation domain at the time $t = 100 \text{ fs}$ for the case of simulations with the laser intensity $I = 10^{20} \text{ W/cm}^2$ and with the beam waist (a) $w_0 = 0.5 \mu\text{m}$, (b) $w_0 = 2.0 \mu\text{m}$ and for the case of simulations with the laser intensity $I = 10^{21} \text{ W/cm}^2$ and with the beam waist (c) $w_0 = 0.5 \mu\text{m}$, (d) $w_0 = 2.0 \mu\text{m}$. The electrons are divided according to their kinetic energy into three separated intervals.

However, in the case of $w_0 = 0.5 \mu\text{m}$ (red line in the fig. 22-c), there is again larger amount of electrons spreading to the sides with respect to the incoming laser pulse.

The electron energy distribution functions at the time $t = 100 \text{ fs}$ as well as the ion energy distributions at the time $t = 150 \text{ fs}$ are shown in the fig. 23. Apart from the case of $w_0 = 0.5 \mu\text{m}$, the high-energy tail of distribution functions has a similar slope which indicates the same hot electron temperatures (fig. 23-a). In the case of $w_0 = 0.5 \mu\text{m}$, the temperature of hot electrons is significantly higher (blue line in the fig. 23-a). Regarding the laser intensity $I = 10^{21} \text{ W/cm}^2$, the energy distribution function of electrons in the case

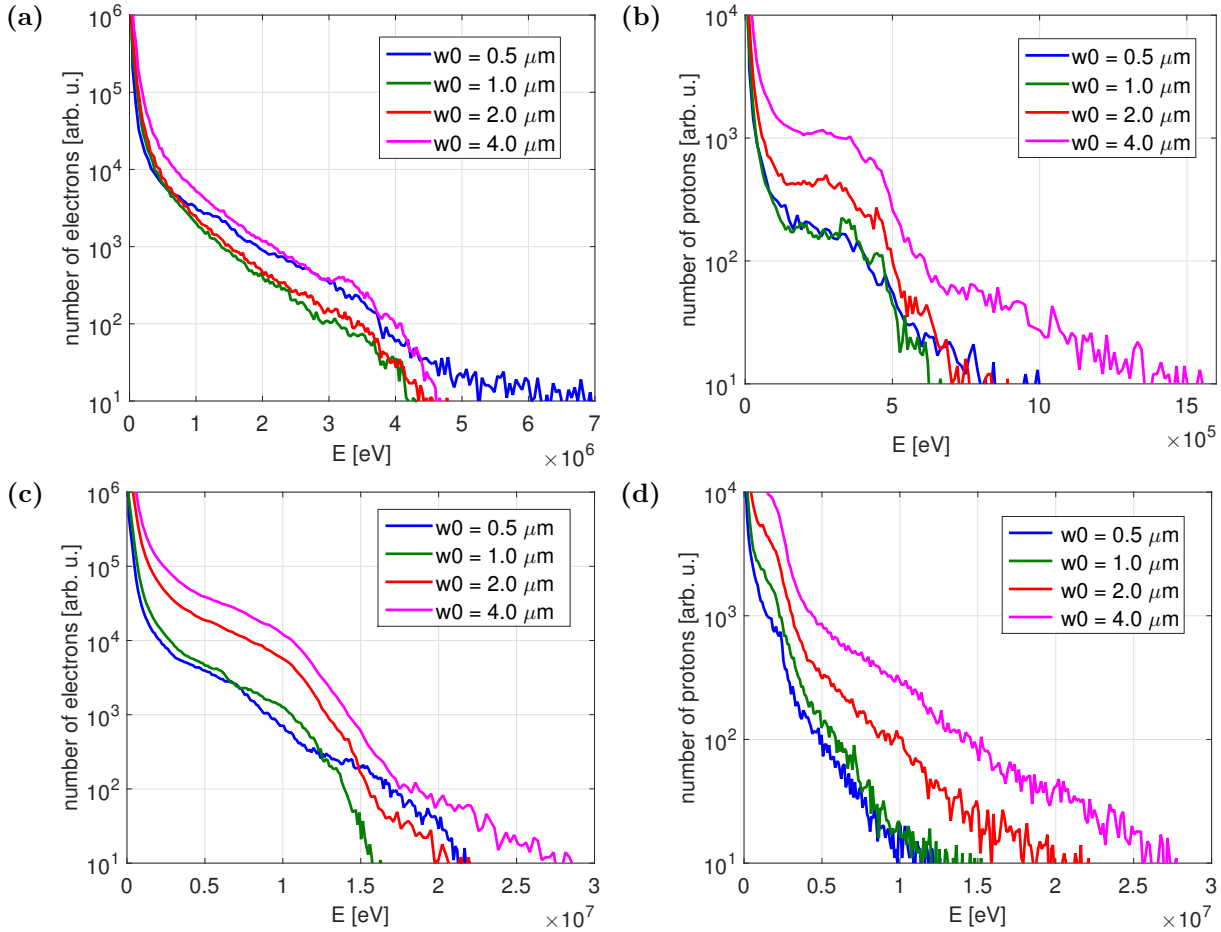


Figure 23: Electron energy distribution in the whole simulation domain for four different beam waists at the time $t = 100 \text{ fs}$ for the case of simulations with the laser intensity (a) $I = 10^{20} \text{ W/cm}^2$ and (c) $I = 10^{21} \text{ W/cm}^2$. Ion energy distribution in the whole simulation domain for four different beam waists at the time $t = 150 \text{ fs}$ for the case of simulations with the laser intensity (b) $I = 10^{20} \text{ W/cm}^2$ and (d) $I = 10^{21} \text{ W/cm}^2$.

of $w_0 = 0.5 \mu\text{m}$ (blue line in the fig. 23-c) is quantitatively different than the distribution functions for the other focal spot sizes. However, as one can see in the fig. 12, ion acceleration sets in at this time so the energy distributions of hot electrons are also influenced by the TNSA process.

Concerning the maximum ion energies (fig. 23-b, 23-d), one can clearly see that they increase with the focal spot size. As already discussed, the electric field decays more slowly for larger spot sizes because it takes more time for hot electrons to spread transversally. Moreover, for the higher intensity, even the peak longitudinal electric field is higher. Therefore, in spite of the fact that the absorption is lower for larger spot size, ion acceleration efficiency is similar to the case of smaller spot size and the cut-off energy of ions is significantly higher.

Conclusion

The beginning of this work summarizes the knowledge required for the further understanding of the laser-plasma interaction. In the first chapter, the fundamental physical aspects of the classical electromagnetic field theory based on the Maxwell's equations as well as the description of Gaussian laser pulse using the paraxial approximation are provided. The second chapter is focused on basic physical processes which take place during the interaction of intense laser pulse with plasma. It includes approaches for plasma description, propagation of electromagnetic wave in plasma, laser absorption and plasma heating mechanisms or mechanisms of laser-driven ion acceleration. In the third chapter, one may find a mathematical derivation of the particle-in-cell method, description of individual steps of the algorithm as well as conditions of its stability. The last section of this chapter is dedicated to code EPOCH, which has been used for simulations within this work.

Starting from the fourth chapter, the work is devoted mainly to tight-focusing. This chapter contains a description, implementation and evaluation of the algorithm for rigorous calculation of electromagnetic fields at boundaries of simulation domain as well as a brief overview of currently used experimental methods for tight-focusing. The fifth chapter then presents results of several large-scale simulations employing tightly focused laser beams interacting with solid targets.

The main benefit of this work is a successful implementation of laser boundary conditions that allow simulate tightly focused laser beams using the two-dimensional version of the computational code EPOCH. The correctness of the algorithm as well as the proper implementation have been verified by plenty of simulations and numerical tests. It has been shown, that the laser beam initialized using the paraxial approximation can lead to unexpected field profiles in the case of tight-focusing - the focal spot is shifted, field profiles are distorted and asymmetric and the peak laser amplitude is lower. These deviations are far from negligible and have a strong impact on laser-matter or laser-plasma simulation results. On the other hand, the simulations of tight-focusing where the beam at the boundary has been prescribed using the Maxwell consistent approach fulfills specified requirement precisely.

The instrumented code has been further exploited for several two-dimensional large-scale simulations employing tightly focused laser beams interacting with solid targets. Obtained results have been processed and thoroughly analyzed while the emphasis has been placed mainly on identifying the effects of the laser beam focal spot size on the laser-matter inter-

Conclusion

action results. The results and observations may be summarized as follows:

Acknowledgments

I wish express my gratitude to both, my supervisor doc. Ing. Ondřej Klímo, Ph.D. and consultant Dr. Stefan Andreas Weber for constant support and guidance, as well as for providing invaluable advice and direction.

Access to computing and storage facilities owned by parties and projects contributing to the National Grid Infrastructure MetaCentrum, provided under the programme "Projects of Large Infrastructure for Research, Development, and Innovations" (LM2010005), is greatly appreciated.

Access to the CERIT-SC computing and storage facilities provided under the programme Center CERIT Scientific Cloud, part of the Operational Program Research and Development for Innovations (reg. no. CZ.1.05/3.2.00/08.0144) is greatly appreciated.

This work was supported by the project ELI: Extreme Light Infrastructure (reg. no. CZ.02.1.01/0.0/0.0/15_008/0000162) from European Regional Development.

The development of the EPOCH code was funded in part by the UK EPSRC grants EP/G054950/1, EP/G056803/1, EP/G055165/1 and EP/M022463/1.

Bc. Petr Valenta

Bibliography

- [1] V. T. Tikhonchuk, A. Colaïtis, A. Vallet, E. L. Aisa, G. Duchateau, P. Nicolaï, and X. Ribeyre, “Physics of laser-plasma interaction for shock ignition of fusion reactions,” *Plasma Physics and Controlled Fusion*, vol. 58, no. 1, p. 014018, 2016.
- [2] D. Batani, S. Baton, A. Casner, S. Depierreux, M. Hohenberger, O. Klimo, M. Koenig, C. Labaune, X. Ribeyre, C. Rousseaux, G. Schurtz, W. Theobald, and V. Tikhonchuk, “Physics issues for shock ignition,” *Nuclear Fusion*, vol. 54, no. 5, p. 054009, 2014.
- [3] R. Betti *et al.*, “Shock ignition: A new approach to high gain inertial confinement fusion on the national ignition facility,” *Phys. Rev. Lett.*, vol. 103, no. 4, 2009.
- [4] T. D. Arber, K. Bennett, C. S. Brady, A. Lawrence-Douglas, M. G. Ramsay, N. J. Sircombe, P. Gillies, R. G. Evans, H. Schmitz, A. R. Bell, and C. P. Ridgers, “Contemporary particle-in-cell approach to laser-plasma modelling,” *Plasma Physics and Controlled Fusion*, vol. 57, no. 11, p. 113001, 2015.
- [5] D. A. Jaroszynski, R. Bingham, and R. A. Cairns, *Laser-Plasma Interactions*. Scottish Graduate Series, CRC Press, 2009.
- [6] T. Pang, *An introduction to computational physics*. Cambridge University Press, 2 ed., 2006.
- [7] H. Gould, J. Tobochnik, and W. Christian, *An introduction to computer simulation methods: applications to physical systems*. Addison–Wesley series in physics, Addison–Wesley, 3 ed., 2007.
- [8] R. W. Hockney and J. W. Eastwood, *Computer Simulation Using Particles*. CRC Press, 2010.
- [9] G. Lapenta, “Particle in cell methods with application to simulations in space weather.” Lecture notes.
- [10] C. K. Birdsall and A. B. Langdon, *Plasma Physics via Computer Simulation*. Series in Plasma Physics, CRC Press, 2004.

- [11] K. Yee, “Numerical solution of initial boundary value problems involving maxwell’s equations in isotropic media,” *IEEE Transactions on Antennas and Propagation*, vol. 14, no. 3, 1966.
- [12] J. Villasenor and O. Buneman, “Rigorous charge conservation for local electromagnetic field solvers,” *Computer Physics Communications*, vol. 69, no. 2-3, 1992.
- [13] T. Z. Esirkepov, “Exact charge conservation scheme for particle-in-cell simulation with an arbitrary form-factor,” *Computer Physics Communications*, vol. 135, no. 2, 2001.
- [14] H. Fehske, R. Schneider, and A. Weiße, *Computational Many-Particle Physics*. Springer, 2008.
- [15] K. Germaschewski, W. Fox, N. Ahmadi, L. Wang, S. Abbott, H. Ruhl, and A. Bhattacharjee, “The plasma simulation code: A modern particle-in-cell code with load-balancing and gpu support,” *arXiv preprint arXiv:1310.7866*, 2013.

Appendices

Appendix A

Input files

This part contains input files of several most important simulations that have been performed for the purposes within this work. All the files below are accepted by the PIC simulation code EPOCH (see chapter 3). Due to the limited space, provided input files shall be taken as a templates where several parameters have been frequently changing (such as beam waist and the laser intensity).

Listing A.1: Input file for evaluation of the implemented algorithm for tight-focusing (chapter 4). In this case, the laser beam propagates according to the Maxwell consistent approach.

```
1 begin:control
2   nx = 1600
3   ny = 4800
4   x_min = -8 * micron
5   x_max = 8 * micron
6   y_min = -24 * micron
7   y_max = 24 * micron
8   t_end = 150 * femto
9   field_order = 2
10  stdout_frequency = 1
11  smooth_currents = T
12  dt_multiplier = 0.95
13 end:control
14
15 begin:boundaries
16   cpml_thickness = 16
17   cpml_kappa_max = 20
18   cpml_a_max = 0.2
19   cpml_sigma_max = 0.7
20   bc_x_min_field = cpml_laser
21   bc_x_max_field = cpml_outflow
22   bc_x_min_particle = thermal
23   bc_x_max_particle = thermal
24   bc_y_min_field = cpml_outflow
25   bc_y_max_field = cpml_outflow
26   bc_y_min_particle = thermal
```

```
27   bc_y_max_particle = thermal
28 end:boundaries
29
30 begin:laser
31   boundary = x_min
32   id = 1
33   fwhm_time = 20 * femto
34   t_0 = 50 * femto
35   w_0 = 0.7 * micron # 5.0 * micron
36   pos = 0.0 * micron
37   focus = 0.0 * micron
38   amp = 1.0e15
39   lambda = 1.0 * micron
40   pol_angle = 0.0 * pi
41   t_start = 0.0 * femto
42   t_end = 300 * femto
43 end:laser
44
45 begin:output
46   name = fields
47   file_prefix = field
48   dump_at_times = 50.00 * femto,
49     76.685127616 * femto, 103.370255232 *
50     femto
51   grid = always + single
52   ex = always + single
53   ey = always + single
54   bz = always + single
55   dump_first = F
56   dump_last = F
57   restartable = F
58 end:output
```

Listing A.2: Input file for identifying the conditions for which the propagation of the laser beam under the paraxial approximation is valid (chapter 4).

```

1 begin:control
2   nx = 1600
3   ny = 4800
4   x_min = -8 * micron
5   x_max = 8 * micron
6   y_min = -24 * micron
7   y_max = 24 * micron
8   t_end = 150 * femto
9   field_order = 2
10  stdout_frequency = 1
11  smooth_currents = T
12  dt_multiplier = 0.95
13 end:control
14
15 begin:boundaries
16   cpml_thickness = 16
17   cpml_kappa_max = 20
18   cpml_a_max = 0.2
19   cpml_sigma_max = 0.7
20   bc_x_min_field = cpml_laser
21   bc_x_max_field = cpml_outflow
22   bc_x_min_particle = thermal
23   bc_x_max_particle = thermal
24   bc_y_min_field = cpml_outflow
25   bc_y_max_field = cpml_outflow
26   bc_y_min_particle = thermal
27   bc_y_max_particle = thermal
28 end:boundaries
29
30 begin:constant
31   cell_xsize = (x_max - x_min) / nx
32   cell_ysize = (y_max - y_min) / ny
33   las_lambda0 = 1.0 * micron
34   las_omega = 2.0 * pi * c / las_lambda0
35   las_time = 2.0 * pi / las_omega
36   theta = 0
37   w0 = 0.7 * micron # 5.0 * micron
38   fwhm_time = 20 * femto
39   w_time = fwhm_time / (2.0 * (sqrt(loge
        (2.0))))
40   xfocus = 8 * micron
41   yc = -xfocus * tan(theta)
42   zR = pi * w0^2 / las_lambda0
43   lfocus = xfocus / cos(theta)
44   wl = w0 * sqrt(1.0+(lfocus^2)/(zR^2))
45   w_y = wl / cos(theta)
46   r_curv = lfocus * (1.0+(zR^2)/(lfocus^2))
47   intensity_fac2d = 1.0 / sqrt(1.0+lfocus^2/
      zR^2) * cos(theta)
48   n_crit = critical(las_omega)
49 end:constant
50
51 begin:laser
52   boundary = x_min
53   amp = 1.8895615869e14
54   lambda = 1.0 * micron
55   pol_angle = 0.0 * pi
56   phase = -2.0*pi*(y-yc)*sin(theta) /
     las_lambda0 + pi/(las_lambda0)*((y-yc)*
     cos(theta))^2*1.0/r_curv - atan(((yc-y)*
     sin(theta)+lfocus)/zR)
57   profile = gauss(y, yc, sqrt(2)*w_y)
58   t_profile = gauss(time, 50*femto, w_time)
59   t_start = 0.0 * femto
60   t_end = 300 * femto
61 end:laser
62
63 begin:output
64   name = fields
65   file_prefix = field
66   dump_at_times = 50.00 * femto,
     76.685127616 * femto, 103.370255232 *
     femto
67   grid = always + single
68   ex = always + single
69   ey = always + single
70   bz = always + single
71   dump_first = F
72   dump_last = F
73   restartable = F
74 end:output

```

Listing A.3: Input file for the large-scale simulations of tightly focused laser beams interacting with solid targets (chapter 5).

```

1 begin:control
2   nx = 1875
3   ny = 5000
4   x_min = 0 * micron
5   x_max = 15 * micron
6   y_min = -20 * micron
7   y_max = 20 * micron
8   t_end = 200 * femto
9   field_order = 2
10  stdout_frequency = 1
11  smooth_currents = T
12  dt_multiplier = 0.95
13 end:control
14
15 begin:boundaries
16   cpml_thickness = 16
17   cpml_kappa_max = 20
18   cpml_a_max = 0.2
19   cpml_sigma_max = 0.7
20   bc_x_min_field = cpml_laser
21   bc_x_max_field = cpml_outflow
22   bc_x_min_particle = thermal
23   bc_x_max_particle = thermal
24   bc_y_min_field = cpml_outflow
25   bc_y_max_field = cpml_outflow
26   bc_y_min_particle = thermal
27   bc_y_max_particle = thermal
28 end:boundaries
29
30

```

```

30 begin:species
31   name = electron
32   charge = -1.0
33   mass = 1.0
34   npart_per_cell = 2000
35   density = if((x gt 8 * micron) and (x lt
36     10 * micron) and (abs(y) lt 15 * micron),
37     100.0 * n_crit, 0.0)
38   temp_ev = 100
39 end:species
40
41 begin:species
42   name = proton
43   charge = 1.0
44   mass = 1836.2
45   npart_per_cell = 100
46   density = density(electron)
47   temp_ev = 100
48 end:species
49
50 begin:laser
51   boundary = x_min
52   id = 1
53   fwhm_time = 30 * femto
54   t_0 = 60 * femto
55   w_0 = 0.5 * micron
56   pos = 0.0 * micron
57   focus = 8.0 * micron
58   intensity_w_cm2 = 1.0e20
59   lambda = 0.8 * micron
60   pol_angle = 0.0 * pi
61   t_start = 0.0 * femto
62   t_end = 300 * femto
63 end:laser
64
65 begin:subset
66   name = tenth
67   random_fraction = 0.1
68   include_species:electron
69   include_species:proton
70 end:subset
71
72 begin:output
73   name = particles
74   file_prefix = part
75   dt_snapshot = 10 * femto
76   particle_grid = tenth + single
77   px = tenth + single
78   py = tenth + single
79   pz = tenth + single
80   particle_weight = tenth + single
81   dump_first = F
82 end:output
83
84 begin:output
85   name = fields
86   file_prefix = field
87   dt_snapshot = 10 * femto
88   grid = always + single
89   ex = always + single
90   ey = always + single
91   bz = always + single
92   dump_first = F
93   dump_last = F
94   restartable = F
95 end:output
96
97 begin:output
98   name = density
99   file_prefix = dens
100  dt_snapshot = 10 * femto
101  mass_density = always + single + species
102  charge_density = always + single + species
103  number_density = always + single + species
104  dump_first = F
105  dump_last = F
106  restartable = F
107 end:output
108
109 begin:output
110  name = diag
111  file_prefix = diag
112  dt_snapshot = 10 * femto
113  ekbar = always + single + species
114  ekflux = always + single + species
115  poynt_flux = always + single
116  temperature = always + single + species
117  total_energy_sum = always
118  dump_first = F
119  dump_last = F
120  restartable = F
121 end:output
122
123 begin:output
124  name = restart
125  file_prefix = r
126  dt_snapshot = 50.0 * femto
127  dump_first = F
128  dump_last = F
129  restartable = T
130 end:output

```


Appendix B

Code listings

Below, one can find the most important functions and methods that has been created within this work to provide some new functionalities and features into the code EPOCH. These serve mainly for the computations of laser fields at boundaries that are consistent with the Maxwell's equations using discrete Fourier transforms. Also, one can find the methods for the data manipulation and routines that interface corresponding C++ functions into the FORTRAN simulation code. Finally, the C++ and FORTRAN adaptors for ParaView Catalyst that enable in-situ visualization and diagnostics with a sample visualization Python script pipeline are all attached.

The following part is provided as it is, only with a short captions. It is mainly intended for those who are interested in the way of implementation and do not want to browse in the full source code, which can be found on the attached CD. Closer details are discussed in the third and fourth chapter of this work.

Listing B.1: Function performing forward fast Fourier transform using Intel® MKL library

```
1 std::vector<std::complex<double>> fft::mkl_fft_forward(std::vector<std::complex<double>> in) {
2     DFTI_DESCRIPTOR_HANDLE desc;
3     MKL_LONG status;
4     DftiCreateDescriptor(&desc, DFTI_DOUBLE, DFTI_COMPLEX, 1, static_cast<MKL_LONG>(in.size()));
5     DftiCommitDescriptor(desc);
6     status = DftiComputeForward(desc, in.data());
7     if (status != 0) {
8         std::cerr << DftiErrorMessage(status) << std::endl;
9         abort();
10    }
11    DftiFreeDescriptor(&desc);
12    return in;
13 }
```

Listing B.2: Function performing backward fast Fourier transform using Intel® MKL library

```
1 std::vector<std::complex<double>> fft::mkl_fft_backward(std::vector<std::complex<double>> in) {
2     DFTI_DESCRIPTOR_HANDLE desc;
3     MKL_LONG status;
4     DftiCreateDescriptor(&desc, DFTI_DOUBLE, DFTI_COMPLEX, 1, static_cast<MKL_LONG>(in.size()));
5     DftiCommitDescriptor(desc);
```

```

6 status = DftiComputeBackward(desc, in.data());
7 if(status != 0) {
8 std::cerr << DftiErrorMessage(status) << std::endl;
9 abort();
10 }
11 DftiFreeDescriptor(&desc);
12 return in;
13 }

```

Listing B.3: Function performing forward fast Fourier transform using FFTW library

```

1 std::vector<std::complex<double>> fft::fftw_fft_forward(std::vector<std::complex<double>> in) {
2 fftw_plan p = fftw_plan_dft_1d(in.size(), reinterpret_cast<fftw_complex*>(in.data()),
3     reinterpret_cast<fftw_complex*>(in.data()), FFTW_FORWARD, FFTW_ESTIMATE);
4 fftw_execute(p);
5 fftw_destroy_plan(p);
6 return in;
}

```

Listing B.4: Function performing backward fast Fourier transform using FFTW library

```

1 std::vector<std::complex<double>> fft::fftw_fft_backward(std::vector<std::complex<double>> in) {
2 fftw_plan p = fftw_plan_dft_1d(in.size(), reinterpret_cast<fftw_complex*>(in.data()),
3     reinterpret_cast<fftw_complex*>(in.data()), FFTW_BACKWARD, FFTW_ESTIMATE);
4 fftw_execute(p);
5 fftw_destroy_plan(p);
6 return in;
}

```

Listing B.5: Function performing forward discrete Fourier transform without using any library

```

1 std::vector<std::complex<double>> fft::fft_forward(std::vector<std::complex<double>> in) {
2 std::vector<std::complex<double>> out(in.size());
3 for(auto j = 0; j < out.size(); j++) {
4 for(auto l = 0; l < out.size(); l++) {
5 out.at(j) += in.at(l) * exp(-2.0 * constants::pi * I * l * j / in.size());
6 }
7 }
8 return out;
9 }

```

Listing B.6: Function performing backward discrete Fourier transform without using any library

```

1 std::vector<std::complex<double>> fft::fft_backward(std::vector<std::complex<double>> in) {
2 std::vector<std::complex<double>> out(in.size());
3 for(auto j = 0; j < out.size(); j++) {
4 for(auto l = 0; l < out.size(); l++) {
5 out.at(j) += in.at(l) * exp(+2.0 * constants::pi * I * l * j / in.size());
6 }
7 }
8 return out;
9 }

```

Listing B.7: Method for performing discrete Fourier transform in time

```

1 void laser_bcs::dft_time(field_2d<std::complex<double>>& field) const {
2 #ifdef OPENMP
3 #pragma omp parallel for schedule(static)

```

```

4 #endif
5 for(auto j = 0; j < this->domain->Nx; j++) {
6 #ifdef USE_MKL
7 field.add_col(fft::mkl_fft_backward(field.get_col(j)), j);
8 #elif USE_FFTW
9 field.add_col(fft::fftw_fft_backward(field.get_col(j)), j);
10 #else
11 field.add_col(fft::fft_backward(field.get_col(j)), j);
12 #endif
13 }
14 field.multiply(this->domain->dt / (2.0 * constants::pi));
15 return;
16 }

```

Listing B.8: Method for performing inverse discrete Fourier transform in time

```

1 void laser_bcs::idft_time(field_2d<std::complex<double>>& field) const {
2 #ifdef OPENMP
3 #pragma omp parallel for schedule(static)
4 #endif
5 for(auto j = 0; j < this->domain->Nx; j++) {
6 #ifdef USE_MKL
7 field.add_col(fft::mkl_fft_forward(field.get_col(j)), j);
8 #elif USE_FFTW
9 field.add_col(fft::fftw_fft_forward(field.get_col(j)), j);
10 #else
11 field.add_col(fft::fft_forward(field.get_col(j)), j);
12 #endif
13 }
14 field.multiply(2.0 * (2.0 * constants::pi) / (this->domain->Nt * this->domain->dt));
15 return;
16 }

```

Listing B.9: Method for performing discrete Fourier transform in space

```

1 void laser_bcs::dft_space(field_2d<std::complex<double>>& field) const {
2 std::vector<std::complex<double>> row_global(this->domain->Nx_global);
3 std::vector<std::complex<double>> row_local;
4 for(auto j = 0; j < this->domain->Nt; j++) {
5 row_local = field.get_row(j);
6 MPI_Gatherv(row_local.data(), this->domain->Nx, MPI_CXX_DOUBLE_COMPLEX, row_global.data(), this->
    domain->counts.data(), this->domain->displs.data(), MPI_CXX_DOUBLE_COMPLEX, 0, MPI_COMM_WORLD
    );
7 if(this->domain->rank == 0) {
8 #ifdef USE_MKL
9 row_global = fft::mkl_fft_forward(row_global);
10 #elif USE_FFTW
11 row_global = fft::fftw_fft_forward(row_global);
12 #else
13 row_global = fft::fft_forward(row_global);
14 #endif
15 }
16 MPI_Scatterv(row_global.data(), this->domain->counts.data(), this->domain->displs.data(),
    MPI_CXX_DOUBLE_COMPLEX, row_local.data(), this->domain->Nx, MPI_CXX_DOUBLE_COMPLEX, 0,
    MPI_COMM_WORLD);
17 field.add_row(row_local, j);
18 }
19 field.multiply(this->domain->dx / (2.0 * constants::pi));
20 return;
21 }

```

Listing B.10: Method for performing inverse discrete Fourier transform in space

```

1 void laser_bcs::idft_space(field_2d<std::complex<double>>& field) const {
2 std::vector<std::complex<double>> row_global(this->domain->Nx_global);
3 std::vector<std::complex<double>> row_local;
4 for(auto j = 0; j < this->domain->Nt; j++) {
5 row_local = field.get_row(j);
6 MPI_Gatherv(row_local.data(), this->domain->Nx, MPI_CXX_DOUBLE_COMPLEX, row_global.data(), this->
    domain->counts.data(), this->domain->displs.data(), MPI_CXX_DOUBLE_COMPLEX, 0, MPI_COMM_WORLD
    );
7 if(this->domain->rank == 0) {
8 #ifdef USE_MKL
9 row_global = fft::mkl_fft_backward(row_global);
10#elif USE_FFTW
11 row_global = fft::fftw_fft_backward(row_global);
12#else
13 row_global = fft::fft_backward(row_global);
14#endif
15}
16MPI_Scatterv(row_global.data(), this->domain->counts.data(), this->domain->displs.data(),
    MPI_CXX_DOUBLE_COMPLEX, row_local.data(), this->domain->Nx, MPI_CXX_DOUBLE_COMPLEX, 0,
    MPI_COMM_WORLD);
17field.add_row(row_local, j);
18}
19field.multiply((2.0 * constants::pi) / (this->domain->Nx_global * this->domain->dx));
20return;
21}

```

Listing B.11: Method for dumping data into shared file

```

1 template <typename T>
2 void field_2d<T>::dump_to_shared_file(std::string name, int row_first, int row_last, int
    row_size_local, int row_size_global, int col_start) const {
3 MPI_File file;
4 MPI_Offset offset = 0;
5 MPI_Status status;
6 MPI_Datatype local_array;
7 int col_size = row_last - row_first;
8 const int ndims = 2;
9 std::array<int, ndims> size_global = {col_size, row_size_global};
10 std::array<int, ndims> size_local = {col_size, row_size_local};
11 std::array<int, ndims> start_coords = {0, col_start};
12 MPI_Type_create_subarray(2, size_global.data(), size_local.data(), start_coords.data(),
    MPI_ORDER_C, MPI_DOUBLE, &local_array);
13 MPI_Type_commit(&local_array);
14 std::vector<double> real_part(col_size * row_size_local);
15 for(auto i = std::make_pair(row_first, 0); i.first < row_last; i.first++, i.second++) {
16 for(auto j = 0; j < row_size_local; j++) {
17 real_part[i.second * row_size_local + j] = std::real(this->data[i.first * row_size_local + j]);
18 }
19 }
20 MPI_File_open(MPI_COMM_WORLD, name.data(), MPI_MODE_CREATE|MPI_MODE_WRONLY, MPI_INFO_NULL, &file)
    ;
21 MPI_File_set_view(file, offset, MPI_DOUBLE, local_array, "native", MPI_INFO_NULL);
22 MPI_File_write_all(file, real_part.data(), col_size * row_size_local, MPI_DOUBLE, &status);
23 MPI_File_close(&file);
24 MPI_Type_free(&local_array);
25 return;
26}

```

Listing B.12: Extern C++ function to fill Fortran arrays with laser fields dumped in binary file

```
1 void populate_laser_at_boundary(double* field, int* id, const char* data_dir, int* timestep, int*
2     size_global, int* first, int* last) {
3     double num = 0.0;
4     std::string laser_id = std::to_string(*id);
5     std::string path(data_dir);
6     std::ifstream in;
7     in.open(path + "/laser_" + laser_id + ".dat", std::ios::binary);
8     if(in.is_open()) {
9         in.seekg(((*timestep) * (*size_global) + (*first) - 1) * sizeof(num));
10        for(auto i = 0; i < *last - *first + 1; i++) {
11            in.read(reinterpret_cast<char*>(&num), sizeof(num));
12            field[i] = num;
13        }
14    } else {
15        std::cout << "error: cannot read file " << path + "/" + filename + laser_id + ".dat" << std::endl
16        ;
17    }
18    return;
19 }
```

Listing B.13: Fortran interfaces for C++ library functions

```
1 INTERFACE
2
3 SUBROUTINE compute_laser_at_boundary(rank, nproc, laser_start, laser_end, &
4 fwhm_time, t_0, omega, pos, amp, w_0, id, L_min, L_max, L_focus, T_min, T_max, &
5 T_ncells, cpml_thickness, t_end, T_cell_size, L_cell_size, dt, output_path) bind(c)
6 USE, INTRINSIC :: iso_c_binding
7 IMPLICIT NONE
8 INTEGER(c_int), INTENT(IN) :: rank, nproc, id, T_ncells, cpml_thickness
9 CHARACTER(kind=c_char), DIMENSION(*), INTENT(IN) :: output_path
10 REAL(c_double), INTENT(IN) :: laser_start, laser_end, fwhm_time, t_0, omega, pos, &
11 amp, w_0, L_min, L_max, L_focus, T_min, T_max, t_end, T_cell_size, L_cell_size, dt
12 END SUBROUTINE compute_laser_at_boundary
13
14 SUBROUTINE populate_laser_at_boundary(field, laser_id, output_path, timestep, size_global, first,
15     last) bind(c)
16 USE, INTRINSIC :: iso_c_binding
17 IMPLICIT NONE
18 INTEGER(c_int), INTENT(IN) :: laser_id, timestep, size_global, first, last
19 CHARACTER(kind=c_char), DIMENSION(*), INTENT(IN) :: output_path
20 REAL(c_double), DIMENSION(*), INTENT(OUT) :: field
21 END SUBROUTINE populate_laser_at_boundary
22 END INTERFACE
```

Listing B.14: Fortran subroutines for Maxwell consistent computation of laser fields at boundaries

```
1 SUBROUTINE Maxwell_consistent_computation_of_EM_fields
2
3 TYPE(laser_block), POINTER :: current
4
5 current => laser_x_min
6 DO WHILE(ASSOCIATED(current))
7 CALL compute_laser_at_boundary(rank, nproc, current%t_start, current%t_end, &
8 current%fwhm_time, current%t_0, current%omega, current%pos, current%amp, current%w_0, &
9 current%id, x_min, x_max, current%focus, y_min, y_max, ny_global, cpml_thickness, t_end, &
10 dy, dx, dt, TRIM(data_dir)//C_NULL_CHAR)
```

```

11 current => current%next
12 ENDDO
13
14 current => laser_x_max
15 DO WHILE(ASSOCIATED(current))
16 CALL compute_laser_at_boundary(rank, nproc, current%t_start, current%t_end, &
17 current%fwhm_time, current%t_0, current%omega, current%pos, current%amp, current%w_0, &
18 current%id, x_min, x_max, current%focus, y_min, y_max, ny_global, cpml_thickness, t_end, &
19 dy, dx, dt, TRIM(data_dir)//C_NULL_CHAR)
20 current => current%next
21 ENDDO
22
23 current => laser_y_min
24 DO WHILE(ASSOCIATED(current))
25 CALL compute_laser_at_boundary(rank, nproc, current%t_start, current%t_end, &
26 current%fwhm_time, current%t_0, current%omega, current%pos, current%amp, current%w_0, &
27 current%id, y_min, y_max, current%focus, x_min, x_max, nx_global, cpml_thickness, t_end, &
28 dx, dy, dt, TRIM(data_dir)//C_NULL_CHAR)
29 current => current%next
30 ENDDO
31
32 current => laser_y_max
33 DO WHILE(ASSOCIATED(current))
34 CALL compute_laser_at_boundary(rank, nproc, current%t_start, current%t_end, &
35 current%fwhm_time, current%t_0, current%omega, current%pos, current%amp, current%w_0, &
36 current%id, y_min, y_max, current%focus, x_min, x_max, nx_global, cpml_thickness, t_end, &
37 dx, dy, dt, TRIM(data_dir)//C_NULL_CHAR)
38 current => current%next
39 ENDDO
40
41 END SUBROUTINE Maxwell_consistent_computation_of_EM_fields

```

Listing B.15: Fortran subroutines for populating laser sources at boundaries

```

1 SUBROUTINE get_source_x_boundary(buffer, laser_id)
2 REAL(num), DIMENSION(:), INTENT(INOUT) :: buffer
3 INTEGER, INTENT(IN) :: laser_id
4 CALL populate_laser_at_boundary(buffer, laser_id, TRIM(data_dir)//C_NULL_CHAR, &
5 step, ny_global, ny_global_min, ny_global_max)
6 END SUBROUTINE get_source_x_boundary
7
8 SUBROUTINE get_source_y_boundary(buffer, laser_id)
9 REAL(num), DIMENSION(:), INTENT(INOUT) :: buffer
10 INTEGER, INTENT(IN) :: laser_id
11 CALL populate_laser_at_boundary(buffer, laser_id, TRIM(data_dir)//C_NULL_CHAR, &
12 step, nx_global, nx_global_min, nx_global_max)
13 END SUBROUTINE get_source_y_boundary

```

Listing B.16: Fortran adaptor for ParaView Catalyst

```

1 MODULE coprocessor
2
3 USE, INTRINSIC :: iso_c_binding
4 USE fields
5
6 IMPLICIT NONE
7
8 CONTAINS
9
10 SUBROUTINE init_coproc(step, time)

```

```

11 INTEGER, INTENT(in) :: step
12 REAL(num), INTENT(in) :: time
13 INTEGER :: ilen, i
14 CHARACTER(len=200) :: arg
15 CALL coprocessorinitialize()
16 DO i = 1, iargc()
17 CALL getarg(i, arg)
18 ilen = len_trim(arg)
19 arg(ilen+1:) = C_NULL_CHAR
20 CALL coprocessoraddpythonscript(arg, ilen)
21 ENDDO
22 CALL createinputdatadescription(step, time, "essential")
23 END SUBROUTINE init_coproc
24
25 SUBROUTINE run_coproc(step, time)
26 INTEGER, INTENT(in) :: step
27 REAL(num), INTENT(in) :: time
28 INTEGER :: flag, mytid, ntids, n, i, j
29 INTEGER, DIMENSION(6) :: local_extent, global_extent
30 INTEGER, DIMENSION(4) :: lim
31 REAL(num), DIMENSION(3*nx*ny) :: e_field, b_field
32 #ifdef OPENMP
33     INTEGER :: omp_get_thread_num, omp_get_num_threads, omp_get_max_threads
34     EXTERNAL :: omp_get_thread_num, omp_get_num_threads, omp_get_max_threads
35 #endiff
36
37 local_extent = (/ nx_global_min, nx_global_max, ny_global_min, ny_global_max, 0, 0 /)
38 global_extent = (/ 1, nx_global, 1, ny_global, 0, 0 /)
39 lim = (/ 1 + ng, nx + ng, 1 + ng, ny + ng /)
40
41 CALL requestdatadescription(step, time, flag)
42 IF (flag /= 0) THEN
43 CALL buildgrid(rank, nproc, step, time, local_extent, global_extent, &
44 x(lim(1):lim(2)), y(lim(3):lim(4)), "essential"//C_NULL_CHAR)
45
46 !$omp parallel default(private(mytid,i,j,n) &
47 shared(ntids,lim,e_field,b_field,ex,ey,ez,bx,by,bz)
48 #ifdef OPENMP
49     mytid = OMP_GET_THREAD_NUM()
50     ntids = OMP_GET_NUM_THREADS()
51 #endiff
52 DO j = 0, lim(4) - lim(3), ntids
53 n = (j+mytid)*(l + lim(2) - lim(1))*3 + 1
54 IF(j + mytid <= lim(4)) THEN
55 DO i = 0, lim(2) - lim(1)
56 e_field(n + 0) = ex(lim(1) + i, lim(3) + j + mytid)
57 e_field(n + 1) = ey(lim(1) + i, lim(3) + j + mytid)
58 e_field(n + 2) = ez(lim(1) + i, lim(3) + j + mytid)
59 b_field(n + 0) = bx(lim(1) + i, lim(3) + j + mytid)
60 b_field(n + 1) = by(lim(1) + i, lim(3) + j + mytid)
61 b_field(n + 2) = bz(lim(1) + i, lim(3) + j + mytid)
62 n = n + 3
63 ENDDO
64 ENDIF
65 ENDDO
66 !$omp end parallel
67
68 CALL addfield(rank, e_field, "E (V/m)"//C_NULL_CHAR, 3, "essential"//C_NULL_CHAR)
69 CALL addfield(rank, b_field, "B (T)"//C_NULL_CHAR, 3, "essential"//C_NULL_CHAR)
70 CALL coprocess()
71 ENDIF
72 END SUBROUTINE run_coproc

```

```

73 SUBROUTINE finalise_coproc()
74 CALL coprocessorfinalize()
75 END SUBROUTINE finalise_coproc
76
77
78 END MODULE coprocessor

```

Listing B.17: C++ adaptor for ParaView Catalyst

```

1 #include "vtkCPDataDescription.h"
2 #include "vtkCPInputDataDescription.h"
3 #include "vtkCPPProcessor.h"
4 #include "vtkCPPythonScriptPipeline.h"
5 #include "vtkCPPythonAdaptorAPI.h"
6
7 #ifdef INSITU_DOUBLE_PREC
8 #include "vtkDoubleArray.h"
9 #else
10 #include "vtkFloatArray.h"
11#endif
12
13#include "vtkSmartPointer.h"
14#include "vtkRectilinearGrid.h"
15#include "vtkPointData.h"
16#include "vtkImageData.h"
17#include "vtkMultiBlockDataSet.h"
18#include "vtkMultiPieceDataSet.h"
19
20#include <iostream>
21#include <fstream>
22#include <vector>
23#include <array>
24
25#ifndef __cplusplus
26extern "C" {
27#endif
28void createinputdatadescription_(int* step, double* time, const char* grid_name);
29void buildgrid_(int* rank, int* size, int* step, double* time, int* local_extent, int*
    global_extent, double* x_coords, double* y_coords, const char* grid_name);
30void addfield_(int* rank, double* input_field, char* name, int* components, const char* grid_name
    );
31#ifndef __cplusplus
32}
33#endif
34
35void createinputdatadescription_(int* step, double* time, const char* grid_name) {
36if (!vtkCPPythonAdaptorAPI::GetCoProcessorData()) {
37vtkGenericWarningMacro("unable to access coprocessor data");
38return;
39}
40vtkCPPythonAdaptorAPI::GetCoProcessorData() ->AddInput(grid_name);
41vtkCPPythonAdaptorAPI::GetCoProcessorData() ->SetTimeData(*time, static_cast<vtkIdType>(*step));
42return;
43}
44
45void buildgrid_(int* rank, int* size, int* step, double* time, int* local_extent, int*
    global_extent, double* x_coords, double* y_coords, const char* grid_name) {
46if (!vtkCPPythonAdaptorAPI::GetCoProcessorData()) {
47vtkGenericWarningMacro("unable to access coprocessor data");
48return;
49}

```

```

50| vtkCPPythonAdaptorAPI::GetCoProcessorData() -> SetTimeData(*time, static_cast<vtkIdType>(*step));
51| if (!vtkCPPythonAdaptorAPI::GetCoProcessorData() -> GetInputDescriptionByName(grid_name) -> GetGrid())
52| {
53|     vtkCPInputDataDescription* idd = vtkCPPythonAdaptorAPI::GetCoProcessorData() ->
54|         GetInputDescriptionByName(grid_name);
55|     if (!idd) {
56|         vtkGenericWarningMacro("cannot access data description to attach grid to");
57|         return;
58|     }
59|     vtkSmartPointer<vtkRectilinearGrid> rectilinear_grid =
60|     vtkSmartPointer<vtkRectilinearGrid>::New();
61|     rectilinear_grid->SetExtent(local_extent);
62|     int* ext = rectilinear_grid->GetExtent();
63|     int dim[3] = {ext[1] - ext[0] + 1, ext[3] - ext[2] + 1, ext[5] - ext[4] + 1};
64|
65| #ifdef INSITU_DOUBLE_PREC
66| vtkSmartPointer<vtkDoubleArray> x_array = vtkSmartPointer<vtkDoubleArray>::New();
67| vtkSmartPointer<vtkDoubleArray> y_array = vtkSmartPointer<vtkDoubleArray>::New();
68| double* x_c = x_coords;
69| double* y_c = y_coords;
70| #else
71| vtkSmartPointer<vtkFloatArray> x_array = vtkSmartPointer<vtkFloatArray>::New();
72| vtkSmartPointer<vtkFloatArray> y_array = vtkSmartPointer<vtkFloatArray>::New();
73| float* x_c = new float[dim[0]];
74| float* y_c = new float[dim[1]];
75| for(std::size_t i = 0; i < dim[0]; i++) {
76|     x_c[i] = static_cast<float>(x_coords[i]);
77| }
78| for(std::size_t i = 0; i < dim[1]; i++) {
79|     y_c[i] = static_cast<float>(y_coords[i]);
80| }
81| #endif
82| x_array->SetNumberOfComponents(1);
83| y_array->SetNumberOfComponents(1);
84| x_array->SetArray(x_c, static_cast<vtkIdType>(dim[0]), 1);
85| y_array->SetArray(y_c, static_cast<vtkIdType>(dim[1]), 1);
86| rectilinear_grid->SetXCoordinates(x_array);
87| rectilinear_grid->SetYCoordinates(y_array);
88|
89| vtkSmartPointer<vtkMultiPieceDataSet> multi_piece = vtkSmartPointer<vtkMultiPieceDataSet>::New();
90| multi_piece->SetNumberOfPieces(*size);
91| multi_piece->SetPiece(*rank, rectilinear_grid);
92|
93| vtkSmartPointer<vtkMultiBlockDataSet> grid = vtkSmartPointer<vtkMultiBlockDataSet>::New();
94| grid->SetNumberOfBlocks(1);
95| grid->SetBlock(0, multi_piece);
96|
97| idd->SetWholeExtent(global_extent);
98| idd->SetGrid(grid);
99|
100| return;
101}
102}
103void addfield_(int* rank, double* input_field, char* name, int* components, const char* grid_name
104)
105if (!vtkCPPythonAdaptorAPI::GetCoProcessorData()) {
106    vtkGenericWarningMacro("unable to access coprocessor data");
107}
108vtkCPInputDataDescription* idd = vtkCPPythonAdaptorAPI::GetCoProcessorData() ->
```

```

    GetInputDescriptionByName(grid_name);
109 vtkMultiBlockDataSet* multi_block = vtkMultiBlockDataSet::SafeDownCast(idd->GetGrid());
110 vtkMultiPieceDataSet* multi_piece = vtkMultiPieceDataSet::SafeDownCast(multi_block->GetBlock(0));
111 vtkRectilinearGrid* type = vtkRectilinearGrid::SafeDownCast(multi_piece->GetPiece(*rank));
112 if (!type) {
113     vtkGenericWarningMacro("no adaptor grid to attach field data to");
114     return;
115 }
116 if (idd->IsFieldNeeded(name)) {
117     int size = (*components)*type->GetNumberOfPoints();
118 #ifdef INSITU_DOUBLE_PREC
119     double* array = input_field;
120     vtkSmartPointer<vtkDoubleArray> field = vtkSmartPointer<vtkDoubleArray>::New();
121 #else
122     float* array = new float[size];
123     for(std::size_t i = 0; i < size; i++) {
124         array[i] = static_cast<float>(input_field[i]);
125     }
126     vtkSmartPointer<vtkFloatArray> field = vtkSmartPointer<vtkFloatArray>::New();
127 #endif
128     field->SetName(name);
129     field->SetNumberOfComponents(*components);
130     field->SetArray(array, static_cast<vtkIdType>(size), 1);
131     type->GetPointData()->AddArray(field);
132 }
133 return;
134 }
```

Listing B.18: Sample visualization pipeline using Python script

```

1 try: paraview.simple
2 except: from paraview.simple import *
3
4 from paraview import coprocessing
5
6 inputs = ['essential']
7 update_freq = 1
8 output_freq = 10000
9
10 def CreateCoProcessor():
11     def _CreatePipeline(coprocessor, datadescription):
12         class Pipeline:
13
14             essential = coprocessor.CreateProducer(datadescription, "essential")
15
16             multi_block_binary_writer = servermanager.writers.XMLMultiBlockDataWriter(Input=essential,
17                 DataMode='Appended', EncodeAppendedData=0, HeaderType='UInt32', CompressorType='ZLib')
18             coprocessor.RegisterWriter(multi_block_binary_writer, filename='full_grid_%t.vtm', freq=
19                 output_freq)
20
21         class CoProcessor(coprocessing.CoProcessor):
22             def CreatePipeline(self, datadescription):
23                 self.Pipeline = _CreatePipeline(self, datadescription)
24
25             coprocessor = CoProcessor()
26             freqs = {}
27             for name in inputs:
28                 freqs[name] = [update_freq]
29             coprocessor.SetUpdateFrequencies(freqs)
30             return coprocessor
```

```

30 coprocessor = CreateCoProcessor()
31 coprocessor.EnableLiveVisualization(True)
32
33 def RequestDataDescription(datadescription):
34     "Callback to populate the request for current timestep"
35     global coprocessor
36
37     if datadescription.GetForceOutput() == True:
38         for i in range(datadescription.GetNumberOfInputDescriptions()):
39             datadescription.GetInputDescription(i).AllFieldsOn()
40             datadescription.GetInputDescription(i).GenerateMeshOn()
41
42     return
43
44 coprocessor.LoadRequestedData(datadescription)
45
46 def DoCoProcessing(datadescription):
47     "Callback to do co-processing for current timestep"
48     global coprocessor
49
50     coprocessor.UpdateProducers(datadescription)
51     coprocessor.WriteData(datadescription);
52     coprocessor.WriteImages(datadescription, rescale_lookuptable=False)
53     coprocessor.DoLiveVisualization(datadescription, "visualization_node", 11111)

```

Listing B.19: EPOCH CMakeLists file to generate platform-specific build scripts

```

1 cmake_minimum_required(VERSION 3.1)
2 project(EPOCH_2D)
3 enable_language(CXX Fortran)
4
5 set(CMAKE_MODULE_PATH ${CMAKE_SOURCE_DIR}/cmake)
6 set(CMAKE_Fortran_MODULE_DIRECTORY ${CMAKE_SOURCE_DIR}/obj)
7 set(CMAKE_ARCHIVE_OUTPUT_DIRECTORY ${CMAKE_SOURCE_DIR}/lib)
8 set(EXECUTABLE_OUTPUT_PATH ${CMAKE_SOURCE_DIR}/bin)
9
10 find_package(MPI REQUIRED)
11 find_package(SDF REQUIRED)
12
13 include_directories(${MPI_Fortran_INCLUDE_PATH})
14 include_directories(${SDF_Fortran_INCLUDE_PATH})
15 include_directories(src/include)
16
17 execute_process(COMMAND ./src/gen_commit_string.sh)
18 execute_process(COMMAND grep -oP "(?=<COMMIT=) [^ ]+" ./src/COMMIT OUTPUT_VARIABLE COMMIT)
19 execute_process(COMMAND date +%s OUTPUT_VARIABLE DATE)
20 execute_process(COMMAND uname -n OUTPUT_VARIABLE MACHINE)
21
22 add_definitions('-D_COMMIT="${COMMIT}"')
23 add_definitions('-D_DATE=${DATE}')
24 add_definitions('-D_MACHINE="${MACHINE}"')
25
26 if(NOT CMAKE_BUILD_TYPE AND NOT CMAKE_CONFIGURATION_TYPES)
27 message(STATUS "Setting build type to 'Release', Debug mode was not specified.")
28 set(CMAKE_BUILD_TYPE Release CACHE STRING "Choose the type of build." FORCE)
29 # Set the possible values of build type for cmake-gui
30 set_property(CACHE CMAKE_BUILD_TYPE PROPERTY STRINGS "Debug" "Release")
31 endif()
32
33 if(${CMAKE_Fortran_COMPILER_ID} MATCHES "Intel")
34 set(CMAKE_Fortran_FLAGS_RELEASE "-O3 -xHost -no-prec-div -fno-math-errno -unroll=3 -qopt-

```

```

    subscript-in-range -align all")
35 set(CMAKE_Fortran_FLAGS_DEBUG "-O0 -nothreads -traceback -flichtconsistency -C -g -heap-arrays 64 -
     warn -fp-stack-check -check bounds -fpe0")
36 elseif(${CMAKE_Fortran_COMPILER_ID} MATCHES "GNU")
37 set(CMAKE_Fortran_FLAGS_RELEASE "-O2 -fimplicit-none -ffixed-line-length-132")
38 set(CMAKE_Fortran_FLAGS_DEBUG "-O0 -g -Wall -Wextra -pedantic -fbounds-check -ffpe-trap=invalid,
     zero,overflow -Wno-unused-parameter")
39 elseif(${CMAKE_Fortran_COMPILER_ID} MATCHES "PGI")
40   set(CMAKE_Fortran_FLAGS_RELEASE "-r8 -fast -fastsse -O3 -Mipa=fast,inline -Minfo")
41   set(CMAKE_Fortran_FLAGS_DEBUG "-Mbounds -g")
42 elseif(${CMAKE_Fortran_COMPILER_ID} MATCHES "G95")
43   set(CMAKE_Fortran_FLAGS_RELEASE "-O3")
44   set(CMAKE_Fortran_FLAGS_DEBUG "-O0 -g")
45 elseif(${CMAKE_Fortran_COMPILER_ID} MATCHES "XL")
46   set(CMAKE_Fortran_FLAGS_RELEASE "-O5 -qhot -qipa")
47   set(CMAKE_Fortran_FLAGS_DEBUG "-O0 -C -g -qfullpath -qinfo -qnosmp -qxflag=dvz -Q! -qnounwind -
     qnunroll")
48 else()
49 message(STATUS "No optimized Fortran compiler flags are known")
50 message(STATUS "Fortran compiler full path: " ${CMAKE_Fortran_COMPILER})
51 set(CMAKE_Fortran_FLAGS_RELEASE "-O2")
52 set(CMAKE_Fortran_FLAGS_DEBUG "-O0 -g")
53 endif()
54
55 if(${CMAKE_CXX_COMPILER_ID} MATCHES "Intel")
56 set(CMAKE_CXX_FLAGS_RELEASE "-O3 -std=c++11 -no-prec-div -ansi-alias -qopt-prefetch=4 -unroll-
     aggressive -m64")
57 set(CMAKE_CXX_FLAGS_DEBUG "-O0 -std=c++11 -g -traceback -mp1 -fp-trap=common -fp-model strict")
58 elseif(${CMAKE_CXX_COMPILER_ID} MATCHES "GNU")
59 set(CMAKE_CXX_FLAGS_RELEASE "-O2 -std=c++11 -msse4 -mtune=native -march=native -funroll-loops -
     fno-math-errno -ffast-math")
60 set(CMAKE_CXX_FLAGS_DEBUG "-O0 -std=c++11 -g -pedantic -Wall -Wextra -Wno-unused")
61 elseif(${CMAKE_CXX_COMPILER_ID} MATCHES "PGI")
62   set(CMAKE_CXX_FLAGS_RELEASE "-std=c++0x")
63   set(CMAKE_CXX_FLAGS_DEBUG "-std=c++0x")
64 elseif(${CMAKE_CXX_COMPILER_ID} MATCHES "G95")
65   set(CMAKE_CXX_FLAGS_RELEASE "-std=c++0x")
66   set(CMAKE_CXX_FLAGS_DEBUG "-std=c++0x")
67 elseif(${CMAKE_CXX_COMPILER_ID} MATCHES "XL")
68   set(CMAKE_CXX_FLAGS_RELEASE "-qlanglvl=extended0x")
69   set(CMAKE_CXX_FLAGS_DEBUG "-qlanglvl=extended0x")
70 else()
71 message(STATUS "No optimized C++ compiler flags are known")
72 message(STATUS "C++ compiler full path: " ${CMAKE_CXX_COMPILER})
73 set(CMAKE_CXX_FLAGS_RELEASE "-O2 -std=c++11")
74 set(CMAKE_CXX_FLAGS_DEBUG "-O0 -std=c++11 -g")
75 endif()
76
77 set(SOURCES
78 ${CMAKE_SOURCE_DIR}/src/epoch2d.F90
79 ${CMAKE_SOURCE_DIR}/src/boundary.f90
80 ${CMAKE_SOURCE_DIR}/src/fields.f90
81 ${CMAKE_SOURCE_DIR}/src/laser.F90
82 ${CMAKE_SOURCE_DIR}/src/particles.F90
83 ${CMAKE_SOURCE_DIR}/src/shared_data.F90
84 )
85
86 set(FOLDERS deck housekeeping io parser physics_packages user_interaction)
87 foreach(FOLDER ${FOLDERS})
88   file(GLOB TMP ${CMAKE_SOURCE_DIR}/src/${FOLDER}/*)
89   list(APPEND SOURCES ${TMP})
90 endforeach()

```

```

91 option(OPENMP "Enable multithreading using OpenMP directives." OFF)
92 option(PER_SPECIES_WEIGHT "Set every pseudoparticle in a species to represent the same number of
93     real particles." OFF)
94 option(NO_TRACER_PARTICLES "Don't enable support for tracer particles." OFF)
95 option(NO_PARTICLE_PROBES "Don't enable support for particle probes." OFF)
96 option(PARTICLE_SHAPE_TOPHAT "Use second order particle weighting." OFF)
97 option(PARTICLE_SHAPE_BSPLINE3 "Use fifth order particle weighting." OFF)
98 option(PARTICLE_ID "Include a unique global particle ID using an 8-byte integer." OFF)
99 option(PARTICLE_ID4 "Include a unique global particle ID using an 4-byte integer." OFF)
100 option(PARTICLE_COUNT_UPDATE "Keep global particle counts up to date." OFF)
101 option(PHOTONS "Include QED routines" OFF)
102 option(TRIDENT_PHOTONS "Use the Trident process for pair production." OFF)
103 option(PREFETCH "Use Intel-specific 'mm_prefetch' calls to load next particle in the list into
104     cache ahead of time." OFF)
105 option(PARSER_DEBUG "Turn on debugging." OFF)
106 option(PARTICLE_DEBUG "Turn on debugging." OFF)
107 option(MPI_DEBUG "Turn on debugging." OFF)
108 option(SIMPLIFY_DEBUG "Turn on debugging." OFF)
109 option(NO_IO "Don't generate any output at all. Useful for benchmarking." OFF)
110 option(COLLISIONS_TEST "Bypass the main simulation and only perform collision tests." OFF)
111 option(PER_PARTICLE_CHARGE_MASS "specify charge and mass per particle rather than per species."
112     OFF)
113 option(PARSER_CHECKING "Perform checks on evaluated deck expressions." OFF)
114 option(USE_INSITU "Link epoch with ParaView Catalyst." OFF)
115 option(INSITU_DOUBLE_PREC "Double precision for data exported insitu." OFF)
116 option(TIGHT_FOCUSING "Maxwell consistent computation of EM fields at boundary for tight-focusing
117     ." OFF)
118
119 if(OPENMP)
120 message(STATUS "Option 'OPENMP' enabled")
121 add_definitions("-DOPENMP")
122 if(${CMAKE_Fortran_COMPILER_ID} MATCHES "Intel")
123 set(CMAKE_Fortran_FLAGS_RELEASE "${CMAKE_Fortran_FLAGS_RELEASE} -fopenmp")
124 set(CMAKE_Fortran_FLAGS_DEBUG "${CMAKE_Fortran_FLAGS_DEBUG} -fopenmp")
125 elseif(${CMAKE_Fortran_COMPILER_ID} MATCHES "GNU")
126 set(CMAKE_Fortran_FLAGS_RELEASE "${CMAKE_Fortran_FLAGS_RELEASE} -fopenmp")
127 set(CMAKE_Fortran_FLAGS_DEBUG "${CMAKE_Fortran_FLAGS_DEBUG} -fopenmp")
128 else()
129 message(STATUS "Fortran OpenMP compiler flag not known.")
130 endif()
131 if(${CMAKE_CXX_COMPILER_ID} MATCHES "Intel")
132 set(CMAKE_CXX_FLAGS_RELEASE "${CMAKE_CXX_FLAGS_RELEASE} -fopenmp")
133 set(CMAKE_CXX_FLAGS_DEBUG "${CMAKE_CXX_FLAGS_DEBUG} -fopenmp")
134 elseif(${CMAKE_CXX_COMPILER_ID} MATCHES "GNU")
135 set(CMAKE_CXX_FLAGS_RELEASE "${CMAKE_CXX_FLAGS_RELEASE} -fopenmp")
136 set(CMAKE_CXX_FLAGS_DEBUG "${CMAKE_CXX_FLAGS_DEBUG} -fopenmp")
137 else()
138 message(STATUS "C++ OpenMP compiler flag not known.")
139 endif()
140 endif()
141
142 if(TIGHT_FOCUSING AND NOT FFT_LIBRARY)
143 message(STATUS "No FFT library specified. Setting FFT library to 'none'.")
144 set(FFT_LIBRARY none CACHE STRING "Choose the FFT library." FORCE)
145 set_property(CACHE FFT_LIBRARY PROPERTY STRINGS "FFTW" "MKL" "None")
146 endif()
147
148 if(PER_SPECIES_WEIGHT)
149 message(STATUS "Option 'PER_SPECIES_WEIGHT' enabled")
150 add_definitions("-DPER_SPECIES_WEIGHT")
151 endif()

```

```

149
150 if(NO_TRACER_PARTICLES)
151 message(STATUS "Option 'NO_TRACER_PARTICLES' enabled")
152 add_definitions("-DNO_TRACER_PARTICLES")
153 endif()
154
155 if(NO_PARTICLE_PROBES)
156 message(STATUS "Option 'NO_PARTICLE_PROBES' enabled")
157 add_definitions("-DNO_PARTICLE_PROBES")
158 endif()
159
160 if(PARTICLE_SHAPE_TOPHAT)
161 message(STATUS "Option 'PARTICLE_SHAPE_TOPHAT' enabled")
162 add_definitions("-DPARTICLE_SHAPE_TOPHAT")
163 endif()
164
165 if(PARTICLE_SHAPE_BSPLINE3)
166 message(STATUS "Option 'PARTICLE_SHAPE_BSPLINE3' enabled")
167 add_definitions("-DPARTICLE_SHAPE_BSPLINE3")
168 endif()
169
170 if(PARTICLE_ID)
171 message(STATUS "Option 'PARTICLE_ID' enabled")
172 add_definitions("-DPARTICLE_ID")
173 endif()
174
175 if(PARTICLE_ID4)
176 message(STATUS "Option 'PARTICLE_ID4' enabled")
177 add_definitions("-DPARTICLE_ID4")
178 endif()
179
180 if(PARTICLE_COUNT_UPDATE)
181 message(STATUS "Option 'PARTICLE_COUNT_UPDATE' enabled")
182 add_definitions("-DPARTICLE_COUNT_UPDATE")
183 endif()
184
185 if(PHOTONS)
186 message(STATUS "Option 'PHOTONS' enabled")
187 add_definitions("-DPHOTONS")
188 endif()
189
190 if(TRIDENT_PHOTONS)
191 message(STATUS "Option 'TRIDENT_PHOTONS' enabled")
192 add_definitions("-DTRIDENT_PHOTONS")
193 endif()
194
195 if(PREFETCH)
196 message(STATUS "Option 'PREFETCH' enabled")
197 add_definitions("-DPREFETCH")
198 endif()
199
200 if(PARSER_DEBUG)
201 message(STATUS "Option 'PARSER_DEBUG' enabled")
202 add_definitions("-DPARSER_DEBUG")
203 endif()
204
205 if(PARTICLE_DEBUG)
206 message(STATUS "Option 'PARTICLE_DEBUG' enabled")
207 add_definitions("-DPARTICLE_DEBUG")
208 endif()
209
210 if(MPI_DEBUG)

```

```

211 message(STATUS "Option 'MPI_DEBUG' enabled")
212 add_definitions("-DMPI_DEBUG")
213 endif()
214
215 if(SIMPLIFY_DEBUG)
216 message(STATUS "Option 'SIMPLIFY_DEBUG' enabled")
217 add_definitions("-DSIMPLIFY_DEBUG")
218 endif()
219
220 if(NO_IO)
221 message(STATUS "Option 'NO_IO' enabled")
222 add_definitions("-DNO_IO")
223 endif()
224
225 if(COLLISIONS_TEST)
226 message(STATUS "Option 'COLLISIONS_TEST' enabled")
227 add_definitions("-DCOLLISIONS_TEST")
228 endif()
229
230 if(PER_PARTICLE_CHARGE_MASS)
231 message(STATUS "Option 'PER_PARTICLE_CHARGE_MASS' enabled")
232 add_definitions("-DPER_PARTICLE_CHARGE_MASS")
233 endif()
234
235 if(PARSER_CHECKING)
236 message(STATUS "Option 'PARSER_CHECKING' enabled")
237 add_definitions("-DPARSER_CHECKING")
238 endif()
239
240 if(USE_INSITU)
241 message(STATUS "Option 'USE_INSITU' enabled")
242 find_package(ParaView 5.2 REQUIRED COMPONENTS vtkPVPythonCatalyst)
243 include(${PARAVIEW_USE_FILE})
244 file(GLOB ADAPTOR ${CMAKE_SOURCE_DIR}/src/adaptor/*)
245 list(APPEND SOURCES ${ADAPTOR})
246 add_definitions("-DINSITU")
247 if(NOT PARAVIEW_USE_MPI)
248 message(SEND_ERROR "ParaView must be built with MPI enabled")
249 endif()
250 if(INSITU_DOUBLE_PREC)
251 message(STATUS "Option 'INSITU_DOUBLE_PREC' enabled")
252 add_definitions("-DINSITU_DOUBLE_PREC")
253 endif()
254 endif()
255
256 if(TIGHT_FOCUSING)
257 message(STATUS "Option 'TIGHT_FOCUSING' enabled")
258 file(GLOB FOCUSING ${CMAKE_SOURCE_DIR}/src/focusing/interface.f90)
259 list(APPEND SOURCES ${FOCUSING})
260 include_directories(${MPI_CXX_INCLUDE_PATH})
261 add_definitions("-DTIGHT_FOCUSING")
262 set(FOCUS_SRC
263 ${CMAKE_SOURCE_DIR}/src/focusing/main.cpp
264 ${CMAKE_SOURCE_DIR}/src/focusing/domain_param.cpp
265 ${CMAKE_SOURCE_DIR}/src/focusing/laser_param.cpp
266 ${CMAKE_SOURCE_DIR}/src/focusing/global.cpp
267 ${CMAKE_SOURCE_DIR}/src/focusing/laser_bcs.cpp
268 )
269 include_directories(${CMAKE_SOURCE_DIR}/src/focusing/inc)
270 if(${FFT_LIBRARY} MATCHES "FFTW")
271 if(OPENMP)
272 message(SEND_ERROR "Multi-threaded FFTW routines are not supported. Disable OpenMP.")

```

```

273 endif()
274 message(STATUS "FFT library: FFTW")
275 message(STATUS "Option 'USE_FFTW' enabled")
276 add_definitions("-DUSE_FFTW")
277 find_package(FFTW REQUIRED)
278 include_directories(${FFTW_INCLUDES})
279 endif()
280 if(${FFT_LIBRARY} MATCHES "MKL")
281 if(NOT ${CMAKE_CXX_COMPILER_ID} MATCHES "Intel")
282 message(SEND_ERROR "MKL library can be used only with Intel compilers")
283 endif()
284 message(STATUS "FFT library: MKL")
285 message(STATUS "Option 'USE_MKL' enabled")
286 add_definitions("-DUSE_MKL")
287 set(CMAKE_CXX_FLAGS_RELEASE "${CMAKE_CXX_FLAGS_RELEASE} -mkl")
288 set(CMAKE_CXX_FLAGS_DEBUG "${CMAKE_CXX_FLAGS_DEBUG} -mkl")
289 set(CMAKE_Fortran_FLAGS_RELEASE "${CMAKE_Fortran_FLAGS_RELEASE} -mkl")
290 set(CMAKE_Fortran_FLAGS_DEBUG "${CMAKE_Fortran_FLAGS_DEBUG} -mkl")
291 endif()
292 if(${FFT_LIBRARY} MATCHES "None")
293 message(STATUS "FFT library: None")
294 endif()
295 add_library(focus ${FOCUS_SRC})
296 if(${FFT_LIBRARY} MATCHES "FFTW")
297 #if(OPENMP)
298 # target_link_libraries(focus LINK_PUBLIC ${FFTW_LIBRARIES} ${FFTW_LIBRARIES_OMP})
299 #else()
300 target_link_libraries(focus LINK_PUBLIC ${FFTW_LIBRARIES})
301 #endif()
302 endif()
303 set_target_properties(focus PROPERTIES LINKER_LANGUAGE CXX)
304 endif()
305
306 add_executable(epoch2d ${SOURCES})
307 target_link_libraries(epoch2d LINK_PRIVATE ${MPI_Fortran_LIBRARIES} ${SDF_Fortran_LIBRARIES})
308 if(USE_INSITU)
309 target_link_libraries(epoch2d LINK_PRIVATE vtkPVPythonCatalyst vtkParallelMPI)
310 endif()
311 if(TIGHT_FOCUSING)
312 target_link_libraries(epoch2d LINK_PRIVATE ${MPI_CXX_LIBRARIES} focus)
313 endif()
314 set_target_properties(epoch2d PROPERTIES LINKER_LANGUAGE Fortran)

```

Appendix C

CD content

directory/file	specification
master_thesis.pdf	this document in standard electronic format
master_thesis/	directory containing all source files related to this document
epoch/	directory containing EPOCH source code with all modifications performed within this work (cloned on 05-05-2017)
input_files/	directory containing the input files for evaluation of the algorithm for tight-focusing (chapter 4) as well as for all the simulations performed within this work (chapter 5)
scripts/	directory containing scripts intended for post-processing of simulation data (MATLAB®, Python)
catalyst/	directory containing ParaView Catalyst pipelines devoted for the in-situ visualization
jobs/	directory containing scripts that has been used to run jobs on computer clusters (PBS, SLURM)